Modelling fracture and healing in particulate composite systems

Ponnusami, S.A.

DOI
10.4233/uuid:ac4dccc7-d9fe-4a90-9606-aa16abf8efed

Publication date
2018

Document Version
Final published version

Citation (APA)
Ponnusami, S. A. (2018). *Modelling fracture and healing in particulate composite systems*. [Dissertation (TU Delft), Delft University of Technology]. https://doi.org/10.4233/uuid:ac4dccc7-d9fe-4a90-9606-aa16abf8efed

Modelling Fracture and Healing in Particulate Composite Systems

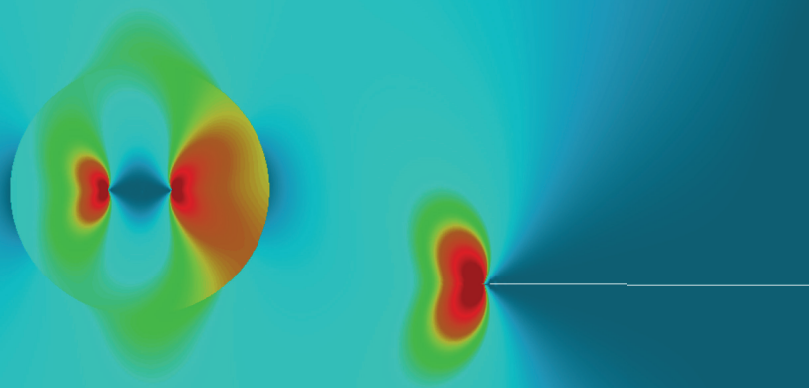

Sathiskumar Anusuya Ponnusami

MODELLING FRACTURE AND HEALING IN PARTICULATE COMPOSITE SYSTEMS

Sathiskumar ANUSUYA PONNUSAMI

MODELLING FRACTURE AND HEALING IN PARTICULATE COMPOSITE SYSTEMS

Proefschrift

ter verkrijging van de graad van doctor
aan de Technische Universiteit Delft,
op gezag van de Rector Magnificus Prof. dr. ir. T.H.J.J. van der Hagen,
voorzitter van het College voor Promoties,
in het openbaar te verdedigen op maandag 09 April 2018 om 10.00 uur

door

Sathiskumar ANUSUYA PONNUSAMI

Master of Engineering, Indian Institute of Science, Bangalore, India
geboren te Tamil Nadu, India

This dissertation has been approved by the promotors:
Prof. dr. ir. S. van der Zwaag, Prof. dr. C. Bisagni and Dr. S. R. Turteltaub

Composition of the doctoral committee:

Rector Magnificus	voorzitter
Prof. dr. ir. S. van der Zwaag	Technische Universiteit Delft, promotor
Prof. dr. C. Bisagni	Technische Universiteit Delft, promotor
Dr. S. R. Turteltaub	Technische Universiteit Delft, promotor

Independent members:

Dr. ir. W. G. Sloof	Technische Universiteit Delft
Prof. dr. ir. A. S. J. Suiker	Technische Universiteit Eindhoven
Prof. dr. ir. L. J. Sluijs	Technische Universiteit Delft
Prof. dr. ir. K. van Breugel	Technische Universiteit Delft

This research was funded by IOP Self Healing Materials (Agentschap NL, now Rijksdienst voor Ondernemend Nederland RVO) through project SHM01021: Self healing thermal barrier coatings.

Keywords: Self-healing materials, Cohesive zone modelling, Crack healing model, Composite materials, Fracture mechanics, Thermal barrier coatings

Printed by: Ridderprint BV, The Netherlands.

ISBN 978-94-6299-944-2

Email: apsathiskumar@gmail.com

An electronic version of this dissertation is available at
http://repository.tudelft.nl/.

To my family and teachers

CONTENTS

1

INTRODUCTION

In this introductory chapter, a brief overview of self-healing materials is presented followed by an introduction to Thermal Barrier Coating (TBC) systems in gas turbine applications. The concept of a self-healing TBC and the underlying mechanisms are explained in the subsequent section. The challenges associated with the realisation of the self-healing TBC are highlighted. These challenges, in turn, emphasise the need for modelling and analysis tools for the successful design of the self-healing system, which forms the core theme of this thesis. Towards the end of this chapter, a short overview of the thesis structure is presented.

1.1. SELF-HEALING MATERIALS

Self-healing materials are a class of materials which possess the capability of autonomously or under minimal external stimulus healing the 'damage' incurred in the material. The term 'damage' here could refer to deterioration of any kind of functionality of the material, though traditionally it refers to mechanical load bearing. Research efforts have been extensive in the field of self-healing materials in the past decade with material classes ranging from polymers, metals, building materials to high-temperature ceramics and fiber reinforced composites. Incorporation of self-healing mechanisms is found to be a promising path to enhance the damage tolerance and extend the lifetime of structural and functional materials. Though the study of biological self-healing materials has been existing since decades, research on man-made self-healing materials started in the 2000s and accelerated following the work of White et al. [WSG+01]. A comprehensive list of different classes of self-healing materials and their healing mechanisms can be found in [vdZ07, vdZB15].

1.1.1. HEALING MECHANISMS AND ROUTES

Self-healing materials can be classified into two classes, extrinsic and intrinsic, depending upon the healing mechanism and the healing agent involved. In an intrinsic

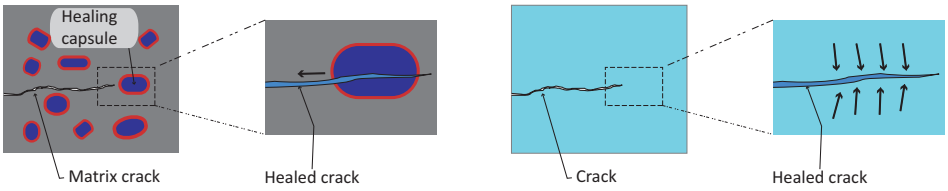

(a) Extrinsic self-healing (b) Intrinsic self-healing

Figure 1.1: Schematic of (a) a capsule-based extrinsic self-healing material: A matrix crack is attracted towards the healing capsule, which upon fracture releases the healing agent into the crack, resulting in crack healing and (b) an intrinsic self-healing material: the healing agent is available directly from the material chemical composition. The material that fills the crack is typically different than the matrix material for both the extrinsic and intrinsic cases.

self-healing material, the healing agent is contained within the host material as its integral constituent. In other words, the healing action is due to the physiochemical nature of the material itself, as illustrated in Fig. 1.1b [BW08]. When damage or cracking occurs, one or more constituents of the material act as the healing agent, which upon completion of the healing process aid in the recovery of the mechanical properties. Some of the examples of the intrinsic self-healing material can be found in the works in [SPM+16, SPS+08]. For instance, in one of the MAX-phase ceramics, Ti_2AlC, aluminium, which is an integral constituent acts as the healing agent under high temperature operating conditions. Upon cracking during its operation, the aluminium atoms in the material diffuse towards the crack faces and react with the ambient oxygen in the operating atmosphere. As a result, alumina, Al_2O_3 forms as a healing product in the crack vicinity, thereby leading to crack healing and recovery of mechanical properties. The advantage of intrinsic self-healing materials is that no modification of the original material's composition is required. Further, such materials have the natural capability of repairing the damage more than once [SPM+16].

In the second class of self-healing materials, the extrinsic ones, the healing agent is not contained within the original material, rather a discrete foreign material constituent is added to the host material during the fabrication process [STD+15, PB05a, TSL+07, CvS15]. This class has been a popular approach as it favours incorporating healing mechanism into any class of material system that does not inherently possess a self-healing characteristic. One of the widely used techniques under this category is encapsulation of the healing agent and dispersing the healing capsules within the host material. When a crack appears in such a material, it interacts with the healing capsule, followed by its rupture or fracturing [WSG+01, KSW03, CvS15]. Upon opening of the capsule, the healing agent flows or diffuses into the crack eventually leading to crack filling, as shown in Fig. 1.1a. Such a healing process involves a sequence of steps starting from crack-capsule interaction, rupture of the capsule, followed by the release of the healing agent into the crack and finally formation of healing product through a chemical or a physical reaction. The resulting healing product, in turn, binds the crack faces together and restores the integrity of the material.

Other extrinsic self-healing materials involve hollow fibers filled with healing agents [PB05a, Dry94] and microvascular networks with distributed healing agents [TSL+07]. Among the extrinsic self-healing mechanisms, the encapsulated particle-based system has been widely investigated [BKO+10, WJ11, VD13]. The encapsulation-based healing concept may lead to a desirable autonomous self-healing behaviour for the system (base material plus healing agent), but it is typically limited by the finite amount of the healing agent which often precludes multiple healing, at least in the location where the healing agent has been consumed. Microvascular network-based self-healing systems offer the possibility of multiple healing after repeated damage events by enhancing the supply of the healing agent.

1.2. THERMAL BARRIER COATINGS

Thermal barrier coating systems are applied on gas turbine engines in order to protect the underlying structural components from the high-temperature environment in the hot zone of a turbine. A modern high-temperature coating system, schematically shown in Fig. 1.2, comprises of a thermal barrier coating (TBC) layer on top of a bond coating (BC) layer. A thin thermally-grown oxide (TGO) layer is formed during operation between the TBC and BC layers as a result of oxidation of one of the metallic constituents of the bond coat. The coating system undergoes a thermal cycle during each start and stop as the turbine's temperature increases from ambient to operating temperature (around 1500^{o}C) and subsequently decreases back to ambient temperature. During each thermal cycle, the layers of the TBC system expand and shrink unequally due to a mismatch in coefficients of thermal expansion (CTE) of the TBC layers as illustrated in Fig.1.2. The resulting thermal stresses cause nucleation and growth of micro-cracks in the TBC system [HST09, EMH+01, PTZX15]. In addition, cracking also occurs due to the thickening of the TGO layer as the oxidation of the metallic bond coating generates more alumina. After several hundred thermal cycles, the micro-cracks eventually coalesce, forming a relatively large crack originally more or less parallel to the TBC-substrate interface. As a large crack deflects towards the free surface via local imperfections, the TBC separates from the substrate, which is known as spallation, as illustrated in Fig. 1.2. As a consequence, large portions of the top coating separate, which may lead to overheating of the unprotected metallic substrate and irreparable damage in structural components and even catastrophic failure of the entire turbine.

The lifetime of TBC systems currently lies between 2000 and 4000 thermal cycles (or flights). Correspondingly, TBC systems on an average need to be replaced about four times during the lifetime of an aircraft engine and these are cost-intensive maintenance operations. Hence, life extension of such systems is always desirable in order to reduce maintenance costs. Several efforts were made in gas turbine industry to enhance the lifetime of the TBC system, for example, by varying the deposition method, coating composition, etc [VJS+10, Cla03, PBD91]. All these routes aim at reducing the occurrence of microcracks, but once formed all such cracks will always grow and unavoidably lead to coating delamination and spallation. From this

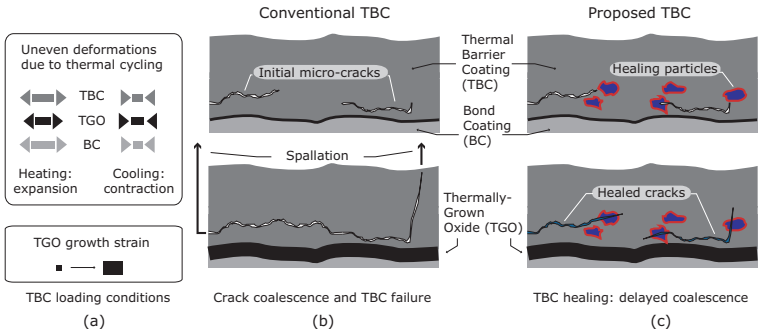

Figure 1.2: Failure mechanisms in Thermal Barrier Coatings and proposed self-healing mechanism.

1

context, one of the promising ideas to improve the lifetime is to incorporate a healing mechanism into the system, thereby healing the microcracks, ultimately resulting in a self-healing TBC system.

1.3. SELF-HEALING TBC SYSTEM

The principle of the self-healing mechanism in the proposed self-healing TBC system is demonstrated in Fig. 1.2. A self-healing agent is encapsulated and embedded within the TBC topcoat layer during the coating process. When the crack reaches the microcapsule, the capsule breaks and the self-healing agent diffuses into the crack, where it can oxidise and heal the crack. As discussed before, multiple microcracks initiate in the TBC layer during thermal cycling process, see Fig. 1.2. The objective is to prevent the coalescence of such microcracks into a major catastrophic crack through self-healing mechanism, thereby extending the lifetime of the TBC system.

In order to successfully realise the concept of autonomous self-healing ceramics for TBCs, the following set of material selection criteria is necessary:

(i) The healing agent to be embedded in the TBC layer should be a solid at the operating temperature, as liquids generally have an unacceptably large thermal expansion coefficient as well as a large thermal conductivity. Further, a non-solid healing agent may be detrimental to the mechanical integrity of the base TBC material system.

(ii) Once the healing process is activated, the healing agent should turn into a (flowing) liquid-like phase which can fill the crack and wet the TBC crack surfaces.

(iii) Subsequently, the viscous liquid-like medium flown into the crack should turn into a solid by a subsequent solid-state chemical reaction with the TBC material, resulting in a load bearing material.

The final outcome of all these reactions should be a crack filled with a well-bonded crystalline material of low thermal conductivity. For real-life applications, additional design parameters such as particle size, volume fraction, mechanical properties and effective 'shelf life' need to be considered during the design process in order to maximise the probability of healing activation and the healing efficiency [MFvdZ09].

In an explorative research by my experimental collaborators [STD+15, SPS+08], it was demonstrated that the addition of Mo-Si based particles leads to the filling of cracks in the TBC layer. Some of the results, in particular, the SEM images and elemental maps of characteristic regions of the healed crack taken from cross sections of the healed sample are shown in Fig. 1.3. The crack is about 2 µm wide and is filled with SiO_2, which has migrated along the crack more than 40 µm away from the healing particle (HP), see (b) in Fig. 1.3. Within the original crack, two phases can be distinguished: the (black) core material in the centre of the crack and an (grey) interface layer separating the SiO_2 filled core material and the YSZ matrix. Elemental maps of such a region show that the core material is free of Zr and only contains Si (and O), while the interface layer contains both Zr and Si. Supporting XRD measurements indicated that the interfacial layer formed consists of $ZrSiO_4$(Zircon). While the crack was not fully filled at all locations along the length of the crack, the SEM observations clearly indicated that the $ZrSiO_4$ was bonded perfectly to the matrix. In the case of thinner cracks, no SiO_2 was observed anymore and only $ZrSiO_4$ was observed in the healed crack zone. However, also some healing particles located well away from the cracks had transformed to $ZrSiO_4$. Thus, it is important to encapsulate the healing particles to protect them from the premature oxidation of the healing agent. For this purpose, a shell of alumina (Al_2O_3) will be created around the healing particles by selective oxidation of a limited amount of Al that is added to the particles. With this approach, the healing mechanism will become active only when required, i.e., when a crack breaks up the alumina shell.

Thus, it was successfully demonstrated that pure $MoSi_2$ or variants alloyed with healing activity enhancing elements such as Al based healing particles can be deposited together with the yttria-partially-stabilised zirconia (YPSZ) using plasma spraying to produce the TBC. Further, it has been shown that the artificially induced cracks in the TBC layer can be healed by oxidation of the Mo-Si based particles. The mechanism of the crack healing is based on the formation of SiO_2 by oxidation when Mo-Si containing particle is exposed to the ambient gas at high temperatures through a crack in the TBC. The Mo forms a volatile oxide (MoO_3) and will leave the coating via the crack path, thereby compensating for the volume increase upon oxidation. The SiO_2 fills the crack and closes it, thus postponing failure of the TBC system. Upon further exposure to high temperature, the silica reacts with the surrounding YSZ material to form load-bearing $ZrSiO_4$, refer, Fig. 1.4 resulting in restoration of mechanical integrity of the TBC.

Nonetheless, this self-healing mechanism is not fully understood and therefore needs to be thoroughly analysed in order to significantly improve its efficiency. More importantly, as the healing particles need to be encapsulated for protection against

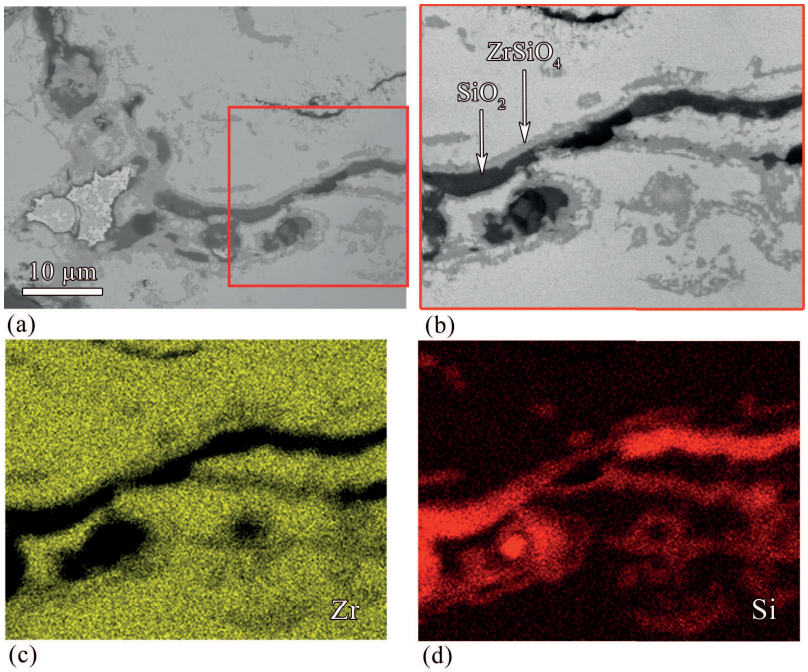

Figure 1.3: Healing of crack in yttria stabilized zirconia TBC with embedded Mo-Si (molybdenum alloyed with silicon) healing particles (HP) after exposure at 1100^{o}C for 20 hours in air. (a) Backscattered electron image of the sample cross section. (b) Enlarged view of the region of interest showing the crack filling and healing material phases, SiO_2 and $ZrSiO_4$ respectively. (c) Corresponding Zr distribution and (d) corresponding Si distribution (X-ray maps).

premature oxidation, it becomes important to understand how the microcracks will interact with the healing particles. To be precise, for healing activation, the rupture of the capsule or particle becomes a prerequisite. Another important research question is that how does the introduction of healing particles affect the mechanical properties of the original material under consideration. Further, it is also critical to understand the relation between the particle size and crack area to be healed, which directly influences the recovery of mechanical properties of the post-healed material. Hence, the present research is aimed at delivering design and analysis tools for optimizing the self-healing capacity of thermal barrier coatings dispersed with Mo-Si based particles or similar self-healing material systems. This is achieved through a combined experimental-modelling approach involving advanced finite element methods.

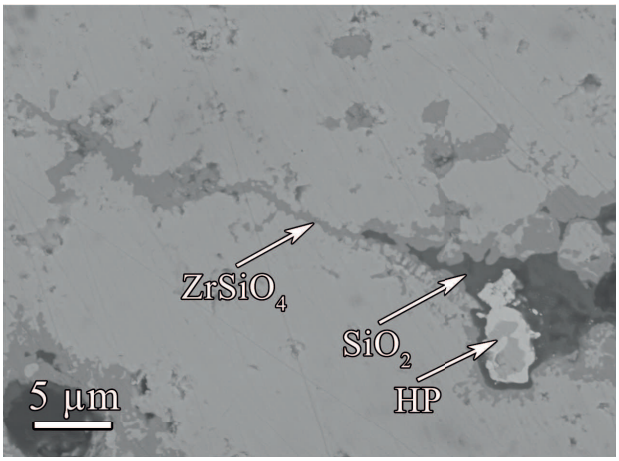

Figure 1.4: Solid Zircone fills in the small crack gaps as well as the closed porosities in the coating structure.

1.4. MODELLING APPROACH AND CHALLENGES

In order to establish an optimal design for the self-healing TBC system, numerous experimental iterations are necessary. Some of the critical parameters or factors that influence the healing mechanism and the performance include mechanical properties of the healing particle, adhesion between the particle and the matrix, location, size and distribution of the healing particles. Such a number of parameters or factors naturally make the design problem complex, necessitating a computational modelling approach to address the challenges in combination with trial experiments. In the present research on self-healing materials, two key aspects are critical to understand and thereby design a successful self-healing material system. Firstly, understanding the fracture mechanism of the material in the presence of healing particles is important, which helps in successful activation of the healing mechanism. And the second is to analyse the post-healing behaviour of the material, in other words, the recovery of mechanical properties upon healing needs to be understood. This thesis treats these two key issues as the research questions and addresses them through a numerical modelling technique, namely the finite element method. A cohesive zone-based fracture mechanics approach is adopted to analyse fracture and healing in the self-healing material system.

1.5. THESIS ORGANIZATION

The thesis is organised as follows. Chapter 2 is dedicated to an investigation of the interaction of a matrix crack with a healing particle, whereby design guidelines are generated for selection and further engineering of the healing particles. In chapter 3, a real TBC microstructure-based finite element analysis is conducted, whereby crack interaction with an actual distribution of multiple healing particles is

considered and the fracture mechanisms are studied. Further, in the same chapter, the effect of healing particle dispersion on the resulting mechanical properties of the composite is quantified. A cohesive zone-based fracture-healing model is developed and implemented in chapter 4. The model possesses the ability to simulate both cracking and healing with additional features such as modelling multiple healing events and varying healing material properties. In chapter 5, the healing model is applied to an intrinsic healing material system, namely the MAX-phase ceramic and the general capabilities of the model are elucidated with the aid of experimental results obtained with the same material system. In a different context, chapter 6 addresses the effect of the presence of the healing particle(s) on the crack driving force using the concept of configurational forces. In particular, it attempts to analyse the crack-particle interaction using driving force parameters and elucidates the effect of using the cohesive zone approach in such interaction studies.

2

CRACK-PARTICLE INTERACTIONS: SINGLE PARTICLE-MATRIX SYSTEM

A cohesive-zone approach is used to study the interaction between an approaching crack and a healing particle embedded in a matrix material as a function of the mismatch in elastic and fracture properties. Crack-particle interaction is a crucial issue governing fracture behavior of particle-dispersed self-healing materials. Special attention is given in the present work to the effect of the mismatch in fracture properties, namely fracture strength and energy, which has not been fully-explored in the literature. Based on extensive finite element simulations using cohesive elements, the basic fracture mechanisms governing the crack-particle interaction are identified, namely particle fracture, crack deflection and interface debonding. The details of the cracking sequences are elucidated and the role of secondary cracks is highlighted. The effect of pre-existing flaws on the fracture behavior is analyzed both for flaws inside the healing particle as well as flaws on the particle/matrix interface. Several flaw configurations in terms of size, orientation and location are considered. In addition, the effect of the mismatch between the matrix and the interface fracture properties is also considered for a wide range of adhesive characteristics. The results of the simulations are summarized in the form of several fracture maps for different configurations, whereby the main fracture mechanisms are identified in regions inside a two-dimensional space of strength and toughness mismatch between the particle and the matrix. These results can be used as a guideline for designing a self-healing particulate composite system with a preferred fracture mechanism, namely matrix cracking, interface debonding or particle fracture.

2.1. INTRODUCTION

Particulate composites is an important class of heterogeneous materials in which the secondary phase are particles, embedded in a suitable matrix material. Particles

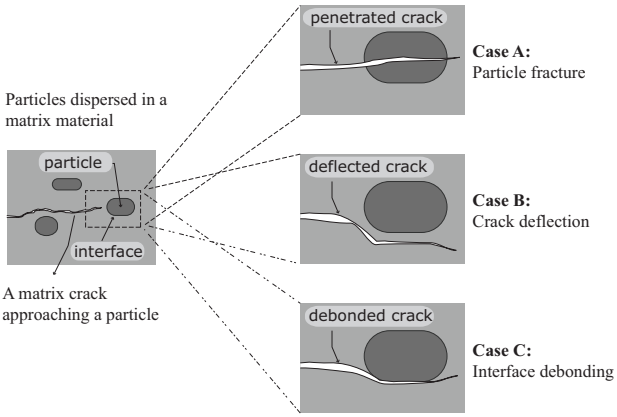

Figure 2.1: Crack-particle interaction in a particulate system showing three possible fracture mechanisms, namely particle fracture, crack deflection and interface debonding.

are typically combined with the host matrix material to increase its functionality, particularly its effective fracture behavior. For example, hard second phase particles are dispersed in an otherwise homogeneous material to strengthen it. An illustrative example of material strengthening is a metal matrix reinforced with ceramic particles (see, e.g.,[LZWZ10, Sri96, CNS89]). Conversely, soft ductile particles are dispersed in a brittle matrix to enhance its fracture toughness such as metallic particles dispersed in a ceramic matrix (see, e.g., [SMD+88, KNH81]). In the context of self-healing materials, a distinct mechanism using embedded particles has been proposed to enhance the long-term resistance against failure. In particular, particles containing a suitable healing agent are dispersed in the matrix [WSG+01, vdZ07]. Upon loading the material, existing microcracks interact with the healing particles, thereby activating the self-healing mechanism. In order to successfully trigger the healing mechanism, it needs to be ensured that a propagating crack gets attracted towards the healing particles instead of deflecting away from them.

The fracture behavior in heterogeneous materials strongly depends on how cracks interact with the individual constituent phases at the microstructural level. In the aforementioned examples, a critical issue is the effect that a particle has on a nearby crack running through the matrix, henceforth referred to as *crack-particle interaction*. A key aspect that governs this interaction is the change in crack tip driving force due to the presence of a particle, which in turn depends upon the mismatch in the properties of the particle and the matrix. Shielding effect is observed when the particle is stiffer than the surrounding matrix material and amplification effect is observed if the particle is softer. As a consequence, a change in the crack trajectory occurs in the presence of the particle. In the context of a particulate composite system, three basic fracture mechanisms could be identified, namely particle fracture, crack deflection and interface debonding as depicted in Fig.2.1.

Several analytical studies have been performed to address the issue of a crack interacting with particles [Atk72, Tam68, EGR74, EG75, PS90, XC01, LC02]. The basic goal of all those studies is to quantify the effect of the particle on the crack tip driving force through parameters like stress intensity factor (SIF) or energy release rate (ERR). The studies establish a key conclusion, namely that a reduction in SIF or crack driving force occurs if the particle ahead of the crack tip is stiffer than the surrounding material and an amplification of crack driving force occurs in the presence of a softer particle leading to shielding and antishielding effects respectively. With the advent of finite element (FE), boundary element (BE) and other numerical methods, studies have been carried out to further analyze crack-particle interaction [LK95, LC93, Bus97, KWHD02, KPTK06, AC06, WPT+07, LS94, NSK+99, AC07, NKMB14]. The advantage of the numerical methods is that it is possible to consider more complex scenarios where analytical solutions are not feasible, such as irregular particle shapes and distribution of particles [RBS09, AC06], the presence of an additional interphase layer between the particle and the matrix [KWHD02] or the presence of pre-existing interface flaw [Bus97].

In general, the primary focus of the aforementioned studies has been the mismatch in elastic properties between the particle and the matrix, generally supporting the notion that a crack in the matrix deflects away from a stiffer particle (shielding effect). In most studies, particle fracture was not considered or was restricted along a specified plane [AC07]. However, experimental observations have shown that particle fracture may occur instead of crack deflection despite the higher stiffness of the particle, which indicates that the mismatch in elastic properties is not sufficient to predict crack-particle interaction [LHB96, Llo91, ML90, HWS94]. Hence, in the present work, one of the primary goals is to take into account additional factors that play a significant role in predicting crack-particle interaction, in particular,

- the effect of the mismatch in *fracture* properties (i.e., mismatch in fracture strength and fracture energy),
- the effect of interfacial properties (i.e., interfacial strength and toughness) and
- the influence of flaws inside the particle and on the interface.

The factors taken into account in the present study are not only important at the level of crack-particle interaction (microscale), but in fact they play a crucial role in determining the *overall* (macroscopic) fracture behavior of a particulate system. For example, in the case of a ductile matrix reinforced with brittle particles, the effective composite strength depends on the efficiency of stress transfer across the particle/matrix interface, which in turn depends on the interface strength. Hence, the material can be significantly weakened if the bonding between the particle and matrix is relatively weak [FFLM08]. In the case of ductile particles dispersed in a brittle matrix, fracture toughness enhancement is generally achieved through plastic deformation of the ductile particles. In that case, the interface properties play a vital role in facilitating the toughness improvement. For example, experimental observations show that the

improvement in fracture toughness may not be realized in such systems [RSR92, Krs83, SY05], which is attributed to a weak particle/matrix interface, whereby the approaching crack induces debonding instead of plastic deformation in the particle. In some other cases, where both phases are brittle, relatively weak interfaces may be preferred since the interface failure can be used as an energy-dissipating mechanism, thereby enhancing the effective toughness of the material [YJ91].

The presence of pre-existing flaws in the interface or the particle can also largely affect the fracture behavior of the particle/matrix system. For instance, in [Bus97], it is reported that a pre-existing interface flaw can attract the approaching crack, which otherwise gets deflected. In case of brittle particle reinforced ductile matrix composites, one would expect an increase in the effective strength due to the strong brittle particles. However, brittle particles may contain flaws or defects which may be inherent to the particle itself or produced during processing. In such cases, the particles attract the approaching crack leading to substantial increase in the crack driving force, thereby resulting in degradation in strength [ML90]. Fracture of stiffer particles dispersed in a softer matrix is observed in several cases, which in general should have the tendency of deflecting the approaching crack [WST86]. Such fracture of stiffer/brittle particles is attributed to presence of flaws within the particle.

Numerical simulations have been carried out to study the behavior of a crack impinging on a planar interface [PT06] as well as the effect of strength of particle/matrix interface [WSB08] or the presence of flaws on the crack path in a particulate system [CSVdB10]. However, there is a need for a systematic analysis where all the relevant mechanisms (i.e., matrix cracking, particle fracture and interface debonding) are simultaneously considered, while taking into account of the mismatch in the elastic and the fracture properties between the constituent phases. Such analysis should also consider the possible nucleation, propagation and coalescence of secondary cracks as the main crack approaches a particle, since this mechanism is often critical in predicting the actual crack-particle interaction.

In the present work, a cohesive zone modelling approach is adopted [Bar62, Dug60], whereby secondary cracks may nucleate in the matrix and/or the particle. Possible crack coalescence and crack bifurcations are also taken into account, which extends the range of possible interactions analyzed. Effects of the mismatch in the elastic and the fracture properties of particle, matrix and interface are examined in detail, combined with the presence of flaws both in the particle and the particle/matrix interface. For each combination of parameters and for each configuration, the crack advancement mechanism is studied and the type of crack-particle interaction is classified. The intention is to provide guidelines that can be used for analysis and design, e.g., to find the required combination of particle/matrix/interface properties to achieve a desired behavior (e.g., to enhance the effective toughness, to increase the effective strength or to trigger a self-healing mechanism).

The chapter is organized as follows. The Cohesive Zone Model (CZM) adopted in the present study is summarized in Sec. 2.2. In addition, that section includes information about the finite element implementation and the simulation set-up. The

effect of the mismatch in fracture properties between the matrix and the particle is treated in Sec.2.3. The effect of pre-existing flaws in the particle is analyzed in Sec.2.4. Sec. 2.5 addresses the influence of *interfacial* fracture properties and the presence of flaws in the interface between the particle and the matrix. Concluding remarks are provided in Sec.2.6.

2.2. MODELLING OF CRACK-PARTICLE INTERACTION

Classical methods in fracture mechanics may be classified as strength-based or fracture energy-based. In the strength-based approach, a crack is initiated if a stress measure (e.g., maximum principal stress) exceeds a critical value corresponding to the strength of the material. In the energy-based approach, a pre-existing crack is propagated if an energy-based measure exceeds a critical value (e.g., fracture energy). Linear elastic fracture mechanics (LEFM) methods based on strain ERR and J-integral are commonly-used energy-based approaches that quantify the amount of energy available at the crack tip for crack propagation [T.L05]. Among these methods, the J-integral approach for fracture became very popular because it circumvents the need to resolve the crack tip stress field accurately. In general, a strength-based approach is effective for crack initiation studies whereas an energy-based approach is useful for the analysis of crack propagation [CPCT06]. Most of the crack-particle interaction studies in the literature discussed in Sec. 2.1 adopt energy-based approaches as the key interest lies in the interaction of a propagating crack with the particle, rather than just crack initiation.

LEFM-based approaches are typically developed for studying the growth of a single pre-existing crack, hence it is in general not possible to model crack nucleation (nucleation of new cracks throughout the analysis) or coalescence of two or more cracks. In this context, Cohesive Zone Models can serve as an alternative to the strength and the energy-based approaches and they are naturally capable of overcoming these limitations. CZM combines the strength and energy-based approaches through the use of a traction-separation law [Bar62]. Moreover, the CZM framework is naturally suitable for analyzing complex crack patterns that arise from multiple crack initiation and coalescence. In the intrinsic cohesive element-based approach adopted in the present study, nucleation, propagation and coalescence do not require additional criteria and in principle do not increase the complexity of the analysis.

2.2.1. COHESIVE ZONE MODEL AND FINITE ELEMENT IMPLEMENTATION

In the CZM approach, the crack tip singularity predicted by the LEFM theory is replaced by a fracture process zone (the cohesive zone) where the material surface degrades from fully-coherent to complete separation. The constitutive behavior in the cohesive zone is described using a traction-separation relation as illustrated in Fig.2.2, which shows the connection between a cracked body and the constitutive relation. The concept of CZM for fracture mechanics was originally developed by Barenblatt [Bar62] for studying cracks in brittle materials and later extended to elastoplastic materials, based on related work by Dugdale [Dug60] (see, e.g., [TH92]). Various

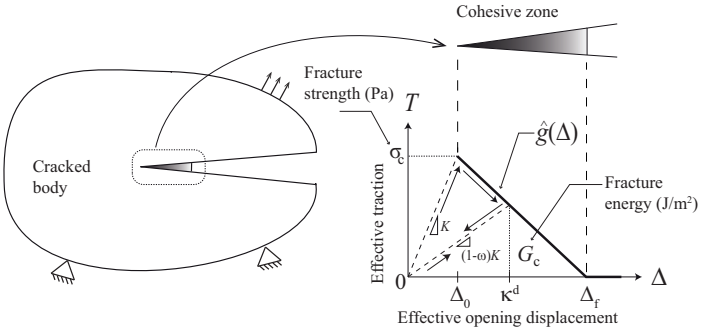

Figure 2.2: Cohesive zone and traction-separation law. The arrows in the traction-separation law represent loading, damage, unloading and reloading steps.

2

cohesive laws have been proposed in the literature for different material systems such as polymers, metals and composites [TH92, Nee90, GB98, CSS03, EGGP01]. Those include exponential, polynomial, trapezoidal and bilinear traction-separation laws.

The cohesive law illustrated in Fig. 2.2 corresponds to a bilinear relation between T, which is a scalar measure of the traction $\boldsymbol{t}$ transmitted across the cohesive surface, and Δ, which is a scalar measure of the cohesive surface opening displacement vector $\boldsymbol{\delta}$. A bilinear relation captures the essential ingredients of most cohesive laws, namely that the traction T increases with increasing cohesive surface opening displacement Δ up to a maximum value given by the material fracture strength, σ_c, and eventually decreases to zero, at which point the cohesive zone is fully-separated in the sense that no (positive) traction can be transmitted across the surface.

The initially increasing part of the curve, which serves the purpose of modelling crack nucleation without a separate nucleation criterion, should in general have a sufficiently large slope to mimic an undamaged surface inside a material (typically referred to as a "rigid" surface in the context of cohesive relations). The initial slope K shown in Fig. 2.2 (i.e., the cohesive stiffness) is not a parameter that may be experimentally measured but, rather, a convenient modelling tool that is normally chosen sufficiently large compared to a representative elastic stiffness of the bulk material (e.g., Young's modulus E).

The area under the traction-separation curve, which represents the total work per unit area expended in creating a fully-separated crack, corresponds to the fracture energy (also called here as toughness for convenience) G_c of the material. Thus, both the strength and the fracture energy are simultaneously taken into account in a cohesive law used for fracture analysis. Furthermore, the cohesive zone approach introduces an inherent characteristic length to the model, designated as the cohesive zone length or fracture process zone length (FPZ), a parameter that combines elastic and fracture characteristics of a material. The fracture process zone length l_{fpz} is

conventionally defined as

$$l_{\mathrm{fpz}} := \frac{EG_{\mathrm{c}}}{\sigma_{\mathrm{c}}^2}\,, \tag{2.1}$$

where E is a representative elastic modulus of the material (typically Young's modulus for an isotropic, homogeneous material). The fracture process zone length (cohesive zone length) can be used as a measure of the brittleness of a material, with decreasing values corresponding to higher brittleness (i.e., lower ductility to strength ratio). Cohesive zone models can reproduce LEFM conditions if the fracture process zone length is negligible compared to the crack length, but may also be used in situations where LEFM is not applicable [PT06]. The influence of fracture process zone length within the context of crack-particle interaction will be explored in later sections.

For completeness and in order to introduce the required notation, the cohesive zone model adopted in the present analysis is briefly summarized below [OP99, HST09]. The traction-separation law relates the traction $\boldsymbol{t}$ acting on the crack faces, with components $(t_{\mathrm{n}}, t_{\mathrm{s}})$, to the crack opening vector $\boldsymbol{\delta}$, with components $(\delta_{\mathrm{n}}, \delta_{\mathrm{s}})$, where the subscripts "n" and "s" refer to the directions normal and tangential to the crack face, respectively. An effective crack opening Δ can be defined as

$$\Delta := \sqrt{\langle \delta_{\mathrm{n}} \rangle^2 + \gamma^2 \delta_{\mathrm{s}}^2}\,, \tag{2.2}$$

where $\langle \cdot \rangle = (\cdot + |\cdot|)/2$ refers to the Macaulay bracket and γ is a non-dimensional weighting factor for the mode I and mode II contributions. In order to determine whether the crack opening is increasing or decreasing due to the external loading process, the following loading function f^{d} is used:

$$f^{\mathrm{d}} = \hat{f}^{\mathrm{d}}(\Delta, \kappa^{\mathrm{d}}) := \Delta - \kappa^{\mathrm{d}}\,, \tag{2.3}$$

where κ^{d} is a damage history variable that, at a given time t, corresponds to the maximum value attained by the equivalent crack opening during a process up to that time, i.e.,

$$\kappa^{\mathrm{d}}(t) := \max_{\tilde{t} \in [0,t]} \Delta\left(\tilde{t}\right)\,.$$

The loading and unloading conditions correspond to the Karush–Kuhn–Tucker relations and are expressed as follows:

$$f^{\mathrm{d}} \dot{\kappa}^{\mathrm{d}} = 0\,, \qquad f^{\mathrm{d}} \leq 0\,, \qquad \dot{\kappa}^{\mathrm{d}} \geq 0\,, \tag{2.4}$$

where $\dot{\kappa}^{\mathrm{d}}$ indicates the (time) rate of change of the damage history variable with $\dot{\kappa}^{\mathrm{d}} > 0$ corresponding to an active damage step and $\dot{\kappa}^{\mathrm{d}} = 0$ to an "elastic" step.

The equivalent crack opening Δ is used to compute the equivalent traction T as

$$T = \hat{T}(\Delta, \kappa^{\mathrm{d}}) = \begin{cases} \hat{g}(\Delta) & \text{if} \quad f^{\mathrm{d}} = 0 \text{ and } \dot{\kappa}^{\mathrm{d}} > 0, \\ \hat{g}(\kappa^{\mathrm{d}}) \dfrac{\Delta}{\kappa^{\mathrm{d}}} & \text{otherwise,} \end{cases} \tag{2.5}$$

where $\hat{g}$ is the effective traction-separation law and $\dot{\kappa}^{\mathrm{d}}$ indicates the (time) rate of change of the damage history variable. The upper and lower expressions in (2.5) provide the equivalent traction during, respectively, crack growth and unloading/reloading. Alternatively, one could work with a damage variable ω and consider a "damaged" stiffness such that $(1-\omega)K = \hat{g}(\kappa^{\mathrm{d}})/\kappa^{\mathrm{d}}$ as indicated in Fig. 2.2.

The specific form of the effective traction-separation law used in the present work is a linear softening relation (see Fig. 2.2), which corresponds to

$$g = \hat{g}(\Delta) = \sigma_{\mathrm{c}} \frac{\langle \Delta_{\mathrm{f}} - \Delta \rangle}{\Delta_{\mathrm{f}} - \Delta_0} \,. \tag{2.6}$$

In the above expression, the parameters Δ_0 and Δ_{f} are, respectively, the equivalent crack opening at the onset of softening and the maximum equivalent crack opening. These parameters may be chosen such that, for a given fracture strength σ_{c}, fracture toughness G_{c} and an initial cohesive stiffness K,

$$\Delta_0 = \frac{\sigma_{\mathrm{c}}}{K} \,, \qquad \Delta_{\mathrm{f}} = \frac{2G_{\mathrm{c}}}{\sigma_{\mathrm{c}}} \,.$$

The initially linearly "elastic" loading up to the fracture strength in a bi-linear law can be reproduced in (2.5) by assigning an initial damage $\kappa^{\mathrm{d}}(0) = \kappa_0^{\mathrm{d}} = \Delta_0$. The parameters Δ_0 and Δ_{f} are chosen such that the maximum of the function $\hat{T}$ in (2.5) equals the fracture strength σ_{c} and the integral of $\hat{T}$ from $\Delta = 0$ to $\Delta = \Delta_{\mathrm{f}}$ equals the material fracture toughness G_{c}.

After evaluating (2.5), the normal and shear tractions can be computed as

$$t_{\mathrm{n}} = \begin{cases} \dfrac{\delta_{\mathrm{n}}}{\Delta} T & \text{if} \quad \delta_{\mathrm{n}} > 0, \\ K\delta_{\mathrm{n}} & \text{if} \quad \delta_{\mathrm{n}} < 0, \end{cases} \tag{2.7}$$

$$t_{\mathrm{s}} = \gamma^2 \frac{\delta_{\mathrm{s}}}{\Delta} T \,,$$

i.e., for $\delta_{\mathrm{n}} \geq 0$, one has that $\boldsymbol{t} \cdot \boldsymbol{\delta} = T\Delta$.

In the context of the finite element method, cohesive laws can be implemented using cohesive elements [OP99, XN94]. Cohesive elements are interface finite elements with zero thickness and their constitutive response during cracking is given by a cohesive law. The term "interface" here refers to the fact that they are embedded between the conventional solid elements (in two or three dimensions), whereby their nodes are shared (see Fig. 2.5). In the present work, cohesive elements are employed for fracture studies in a particle/matrix system, in conjunction with a bilinear traction-separation law, as shown in Fig. 2.2.

The cohesive model presented above can be reproduced with the one available in the Finite Element package Abaqus using an appropriate choice of model options and parameters [ABA11]. In particular, let $\delta_{\mathrm{n},0}$ and $\delta_{\mathrm{s},0}$ denote, respectively, the crack

opening at the onset of failure for pure mode I and pure mode II and let $t_{n,c}$ and $t_{s,c}$ be the corresponding values of the cohesive strength, with $t_{n,c} = K\delta_{n,0}$ and $t_{s,c} = \gamma^2 K\delta_{s,0}$. The non-dimensional weighting factor γ is

$$\gamma = \frac{\delta_{n,0}}{\delta_{s,0}} ,$$

hence $\Delta_0 = \delta_{n,0} = \gamma\delta_{s,0}$ and, using the stiffnesses K and $\gamma^2 K$ in modes I and II, respectively, then $\sigma_c = t_{n,c} = t_{s,c}/\gamma$. Complete loss of cohesion occurs for pure mode I and II, respectively, at $\delta_{n,f}$ and $\delta_{s,f}$, with $\Delta_f = \delta_{n,f} = \gamma\delta_{s,f}$. The features indicated above for the linear softening model can be reproduced in Abaqus using (i) a quadratic nominal strain damage initiation criterion with $\delta_{n,0} = \gamma\delta_{s,0}$ and (ii) an energy-based linear softening model for damage evolution with an exponent equal to 1 in the power law and with equal toughness in pure mode I and II, i.e., $G_{Ic} = G_{IIc}$. Although this formulation does not contemplate distinct values of the fracture toughness in modes I and II, it has the advantage of being thermodynamically admissible since it satisfies the entropy inequality upon application of the Coleman-Noll procedure [OP99].

The cohesive element-based approach can be straightforward if the actual (or possible) crack path(s) is (are) known a priori. However, in general the crack path is an outcome of the simulation, hence it has to be ensured that a crack can initiate at *any* material point and can grow along an *arbitrary* direction. To this end, in the present analysis, cohesive elements are embedded along *all* continuum elements, as shown schematically in Fig.2.5. For the sake of clarity, the cohesive elements are shown to possess certain thickness, but in the actual finite element mesh, they have zero thickness. To achieve the cohesive element insertion, a Matlab script is developed which reads the Abaqus input file (nodal coordinates and element connectivity) and processes them to embed cohesive elements throughout the existing mesh by introducing the required additional nodes and altering the element connectivity accordingly. One of the natural questions that arise with this methodology is the issue of mesh dependency since the crack path is still constrained to move along the element boundaries. This issue is analyzed in Appendix 7.1 for the present simulations where it is shown that, with a sufficiently refined and randomly-oriented mesh, a pre-defined mesh of cohesive elements is a viable alternative to other methods (in particular, the extended finite element method, XFEM), albeit at an increased computational cost. One key advantage of using embedded cohesive elements pertains to crack coalescence, an issue that is important in the present work, which cannot be robustly handled by the current XFEM implementation. Abaqus Standard implicit solver is used for the simulations with the standard Newton-Raphson method. To alleviate convergence difficulties (encountered during the cracking process, especially during multiple cracking and coalescence), a small value of viscosity equal to 1.0×10^{-5} s is used for the simulations which involve too many cutbacks during the solution process.

2.2.2. SIMULATION SET-UP

In order to analyze the crack-particle interaction, numerical simulations are carried out in a two-dimensional rectangular domain of length L and height W, which contains a single particle of diameter $d = 2r$ embedded in a matrix. The domain contains an initially straight edge crack of length a with its crack tip located at a horizontal distance b and vertical distance c measured from the center of the particle, as shown in Fig. 2.3. The initial crack length is taken as $a = 0.4L$. The horizontal distance is chosen as $b = 7r$, which is sufficiently large such that the influence of the particle on the crack driving force is initially negligible, regardless of the vertical offset c (see [Bus97, KWHD02]). Distinct values of the offset c are considered since this initial configuration is relevant for the subsequent crack-particle interaction. It is worth pointing out that a pre-existing crack is in principle not required for an analysis based on cohesive elements. However, for the purpose of comparing distinct crack-particle interactions, it is convenient that all simulations start with the same main approaching crack. Nevertheless, possible nucleation of secondary cracks is permitted throughout the simulation.

The specimen is loaded nominally in opening mode. A concurrent multiscale type of approach is adopted in order to eliminate the interaction between the applied load on the boundary and the stress fields in the region of interest, i.e., in the proximity of particle. An infinite matrix is simulated using a two-scale finite element domain consisting of a fine mesh in the smaller inner domain containing the particle and a coarse mesh in the outer domain as shown in Fig.2.4. The characteristic length of the elements, l_e in the fine mesh is chosen sufficiently small (Appendix 7.1) compared to the fracture process zone length given in (2.1) in order to guarantee a proper resolution of the process zone. The dimensions of the computational domain are chosen sufficiently large compared to the radius r of the particle (in particular, $L/r = 800$ with $L = 1.2W$). Linear plane strain triangular elements are used for the continuum description and four-noded, zero thickness cohesive elements, available in the finite element package Abaqus, are used for fracture. Isotropic, linearly elastic models are used for the matrix and the particle prior to fracture.

An extensive parametric analysis is performed by considering distinct mismatches of the fracture properties, namely the strength ratio σ_c^p/σ_c^m and the toughness ratio G_c^p/G_c^m, where the superscripts "p" and "m" refer to the properties of the particle and the matrix, respectively. In addition, the interface between the particle and the matrix is modelled with a separate traction-separation relation, which depends on an (interface) strength σ_c^i and a (delamination) toughness G_c^i. Unless otherwise indicated, the properties of the matrix for the simulations are set as follows:

$$E^m = 150 \text{ GPa}\,, \quad \sigma_c^m = 300 \text{ MPa}\,, \quad G_c^m = 100 \text{ J/m}^2\,.$$

For simplicity, the Poisson's ratios of the particle and the matrix, ν^p and ν^m, are kept constant and equal in all the simulations, with $\nu^p = \nu^m = 0.25$. Unless explicitly mentioned, the simulations are carried out with a ratio $E^p/E^m = 3$, which corresponds to a stiffer particle, with E^p representing the Young's modulus of the particle.

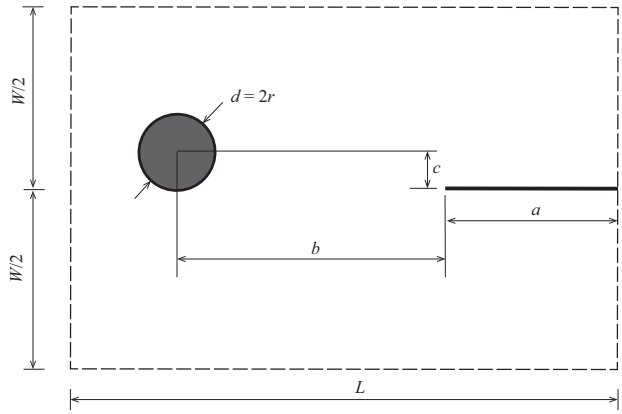

Figure 2.3: Particle of diameter $d = 2r$ embedded in a rectangular domain $L \times W$ with an edge crack of length $a = 0.4L$; Sketch not to scale, actual dimensions are chosen as $L = 800r$ and $L = 1.2W$. A main approaching crack tip is initially located at a horizontal distance $b = 7r$ and vertical distance c (offset).

Table 2.1: Summary of geometric and material parameters used in this study.

Geometric parameters	Ratio of material parameters
Particle offset, $(r/2, r, 3r/2, 2r)$	Elastic modulus, $(E^{\mathrm{p}}/E^{\mathrm{m}} = 3, 1, 1/3)$
Particle flaw size, $(r/4, r/2, r, 4r/3)$	Fracture strength, $(0.1 < \sigma_{\mathrm{c}}^{\mathrm{p}}/\sigma_{\mathrm{c}}^{\mathrm{m}} < 10)$
Particle flaw orientation, $(0°, 30°, 60°, 90°)$	Fracture toughness, $(0.01 < G_{\mathrm{c}}^{\mathrm{p}}/G_{\mathrm{c}}^{\mathrm{m}} < 100)$
Interface flaw size (angle subtended by the flaw), (15° - 120°)	Fracture process zone length, $(\bar{l}_{\mathrm{fpz}}^{\mathrm{m}} \sim 10^m, m = -1, 0, 1, 2, 3)$
Interface flaw location, (top, middle, bottom)	

It is convenient to introduce in the simulations a non-dimensional fracture length scale parameter $\bar{l}_{\mathrm{fpz}}^{\mathrm{m}}$ that relates the fracture process zone length of the matrix $l_{\mathrm{fpz}}^{\mathrm{m}}$ to the particle's radius r, i.e., from (2.1),

$$\bar{l}_{\mathrm{fpz}}^{\mathrm{m}} := \frac{l_{\mathrm{fpz}}^{\mathrm{m}}}{r} = \frac{E^{\mathrm{m}} G_{\mathrm{c}}^{\mathrm{m}}}{\left(\sigma_{\mathrm{c}}^{\mathrm{m}}\right)^2 r} \,. \tag{2.8}$$

The fracture process zone length of the particle varies accordingly with the change in properties of the particle relative to the matrix. In this study, the radius of the particle is chosen as $r = 15\,\mu\mathrm{m}$. Along with the properties of the matrix mentioned above, the matrix fracture length scale parameter becomes $\bar{l}_{\mathrm{fpz}}^{\mathrm{m}} = 1.1 \times 10^1$. The dependence of the fracture mechanism on the length scale is explored in Sec. 2.4, whereby different orders of magnitude for the length scale parameter are considered by altering the toughness of the matrix. To provide an overview of the parametric simulations, different parameters and their range considered are summarized in Table 2.1.

The non-dimensional weighting factor γ for the mode I and mode II contributions is set to 1 (equal contribution), which implies that the simulations allow for a substantial mode II contribution if required by the local stress/deformation fields during crack growth. This is particularly relevant when analyzing interface delamination.

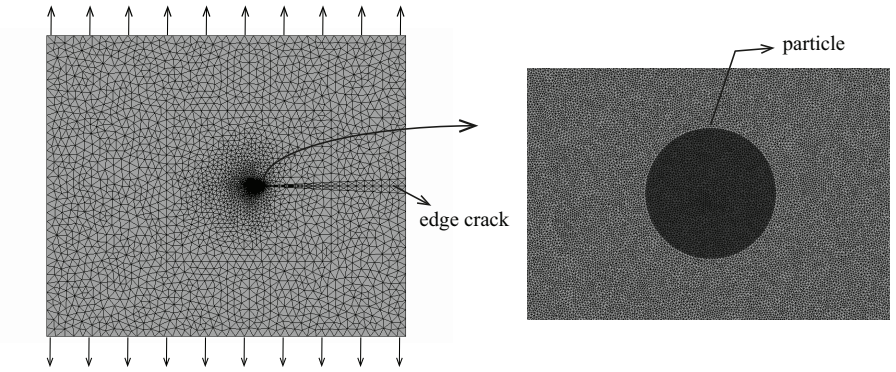

Figure 2.4: Two-scale finite element mesh of the complete 2D domain (left). Finer mesh near the proximity of the particle (right). The element size in the finer mesh region is chosen as $l_e = 0.5\,\mu m$ such that $l_e / l^m_{fpz} = 0.003$. The radius of the particle is chosen as $r = 15\,\mu m$.

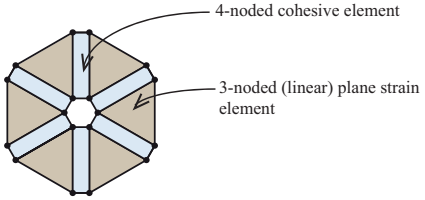

Figure 2.5: Schematic of embedded cohesive elements.

2.3. EFFECT OF MISMATCH IN FRACTURE PROPERTIES FOR A PERFECTLY-BONDED, UNDAMAGED PARTICLE

One primary goal of the present analysis is to study the effect that the mismatch in fracture properties has on the crack trajectory. To achieve this, extensive parametric analyses are conducted and the results are reported in this section. Sec.2.3.1 provides the overview of different parameters used for the parametric study and describes the associated fracture mechanisms. Secs. 2.3.2 and 2.3.3 focus on the local fracture mechanisms in detail using the observed crack sequence and path, whereas Secs. 2.3.4 and 2.3.5 summarize the results of the parametric analyses in the form of fracture maps distinguishing the fracture mechanisms.

2.3.1. SIMULATION PARAMETERS AND FRACTURE MECHANISMS

To this end, the fracture properties of the particle are varied relative to the properties of the matrix, i.e., different ratios of the fracture strengths, σ^p_c / σ^m_c, and fracture energies, G^p_c / G^m_c, are considered. In this section, the particle is assumed to be perfectly bonded to the matrix, i.e., the interfacial strength σ^i_c and the delamination toughness G^i_c are artificially set to a sufficiently large value such that separation at the particle/matrix

interface is prevented. All the simulations conducted in Sec. 2.3 are obtained with the fracture length scale of the matrix, $\bar{l}^{\mathrm{m}}_{\mathrm{fpz}} = 1.1 \times 10^{1}$. The fracture length scale of the particle varies accordingly with its elastic and fracture properties relative to the matrix.

In addition to distinct fracture properties, it is also relevant to consider different crack-path offsets c as indicated in Fig. 2.3. Four representative values are considered for c, namely $c = r/2, r, 3r/2$ and $2r$, which are within the range of practical interest in which the interaction between the crack and the particle is noticeable as the main crack approaches the particle. For each set of fracture properties and offset, a numerical simulation is carried according to the set-up indicated in Sec. 2.2.2 and the corresponding crack pattern is classified in terms of one of the following possible outcomes:

- **Case 1**: Particle fracture, which occurs either when the main approaching crack enters into the particle or when a secondary crack nucleates inside the particle and grows into the matrix.
- **Case 2**: Crack deflection, which corresponds to the situation where the main approaching crack remains confined to the matrix.

Observe that the notion of particle fracture is reserved in the present work for a situation where a crack runs continuously across the particle/matrix interface. In other words, if a new secondary crack initiates inside the particle or a secondary crack initiates from a pre-existing flaw within the particle, but does not propagate into the matrix, then the fracture mechanism is not qualified as particle fracture. Further, the expression crack "deflection" refers to the fact that the crack does not enter the particle, regardless of whether the initial offset c is increased or reduced. The relevance of the classification indicated above is connected to the purpose of embedding particles in the matrix. In particular, case 1 is typically required when designing a particle-based self-healing material whereas case 2 is often favorable for particle toughening purposes.

Numerical simulations, using the model parameters indicated in Sec. 2.2.2, are carried out by increasing the remotely-applied external load (see Fig. 2.4) until the crack tip has moved substantially away from the particle, at which point the crack pattern close to the particle is not expected to evolve further. In order to get insight into the crack-particle interaction, crack paths are shown and discussed in detail for two selected particle offsets, $c = r/2$ and $3r/2$, for representative mismatches in fracture properties and for two mismatches in elastic properties, namely $E^{\mathrm{p}}/E^{\mathrm{m}} = 3$ (stiff particle) and $E^{\mathrm{p}}/E^{\mathrm{m}} = 1/3$ (soft particle). A summary of calculations for all offsets is provided at the end of this section.

2.3.2. BEHAVIOR OF INCOMING CRACKS ALIGNED WITH PARTICLE (OFFSET $c = r/2$)

An initial crack offset $c = r/2$ (see Fig. 2.3) is representative of the situation where the particle is located directly in front of the path of an incoming crack. The actual path

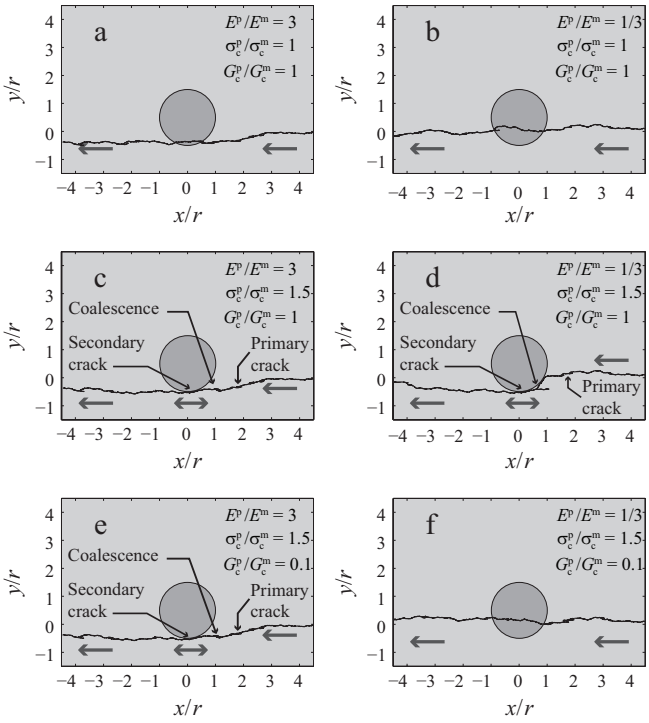

Figure 2.6: Crack paths of an incoming crack with an initial offset $c = r/2$ relative to a perfectly-bonded, undamaged particle for selected mismatches in elastic and fracture properties (advancing crack path is from right to left).

that the crack adopts as it approaches the particle depends on the relative elastic and fracture properties of the matrix and the particle, as shown in Fig. 2.6. Figures on the left column (a,c, and e) correspond to a stiffer particle case, $E^p/E^m = 3$ and figures on the right column (b, d and f) correspond to softer particle case, $E^p/E^m = 1/3$. The other relative properties (i.e., the relative fracture strength and toughness) are varied correspondingly and shown in the figure. In all cases, the particle is initially undamaged and has a perfect bonding with the matrix.

All crack paths shown in Fig. 2.6, which advance from right to left, are essentially the same until the crack front reaches a distance equal to the diameter of the particle (measured from the particle's center). In three cases (a, b and f) particle fracture is observed whereas in the other cases (c, d, and e), crack deflection occurs. Small crack fluctuations in the crack paths may in fact be attributed to mesh resolution (see also 7.1). It can be observed from Fig. 2.6a and b that, when there is no mismatch in fracture properties (same fracture properties for the particle and the matrix), particle fracture

occurs in both cases, however, the stiffer particle (case a) deflects the incoming crack away from it. Nonetheless, the mismatch in elastic modulus does not prevent particle fracture despite higher stiffness of the particle.

When the strength of the particle is larger than the strength of the matrix while the toughnesses are the same (cases c and d), the approaching crack deflects along the particle. It is worth indicating that the crack actually does not propagate monotonically. Instead, as the primary crack approaches the particle, a secondary crack nucleates near the bottom of the particle (on the matrix side). This secondary crack grows and eventually coalesces with the primary incoming crack. Subsequently, after effectively by-passing the particle via this mechanism, the unified crack resumes its mode I path in the matrix. The crack paths shown in the figures only indicate the parts that are open (portions of the secondary crack that are closed due to unloading are not shown). Consequently, it can be concluded that for cases c and d, the mismatch in fracture properties have a significant influence on the crack path.

Cases e and f show the interplay between elastic and fracture properties, which show a more significant effect of the mismatch in elastic modulus. In these cases, the strength of the particle is higher than the matrix (as in cases c and d), but the toughness of the particle is smaller (reduced by a factor of 10 relative to the toughness of the matrix). Case e is essentially similar to the case c indicated above (i.e., a secondary crack nucleates and coalesces with the main crack). In case f the main crack is attracted to the particle due to the elastic mismatch (soft particle). This behavior is initially similar to case d, however in case f the toughness of the particle is relatively low and the main crack continues through the particle. Hence, the mismatch in elastic properties do play a significant role in cases e and f, but only in combination with the fracture properties.

2.3.3. BEHAVIOR OF INCOMING CRACKS NOT ALIGNED WITH PARTICLE (OFFSET $c = 3r/2$)

Representative crack paths for an incoming crack with an offset $c = 3r/2$ with respect to the particle are indicated in Fig. 2.7. The crack paths on left side of the figure correspond to the stiffer particle case ($E^{\mathrm{p}}/E^{\mathrm{m}} = 3$) and the right side corresponds to the softer particle case ($E^{\mathrm{p}}/E^{\mathrm{m}} = 1/3$). As in Sec. 2.3.2, all crack paths are essentially the same until the crack front reaches a distance equal to the diameter of the particle. In two cases (a and b) crack deflection occurs whereas in the other cases (c, d, e and f), particle fracture occurs.

In cases a and b in Fig. 2.7 the fracture strength and toughness are the same for the particle and the matrix, hence any deviation from a straight path can be purely attributed to the elastic modulus mismatch. For the stiffer particle, case a, a slight crack deflection away from the particle is observed. In case b, the main crack is attracted towards the softer particle. The elastic mismatch (lower stiffness of the particle), however, is not sufficiently low to completely deviate the crack path, which eventually moves away from the particle due to the influence of the externally applied stress field.

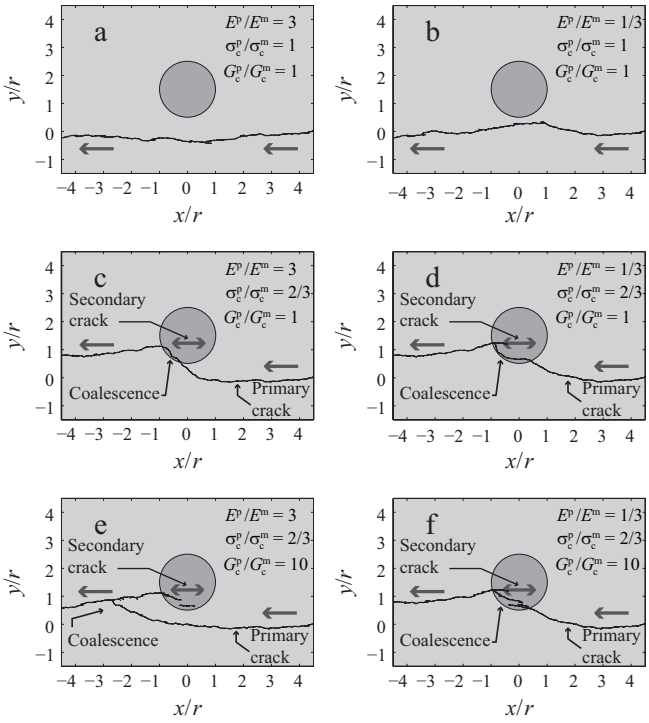

Figure 2.7: Crack paths for particle offset $c = 3r/2$; crack path is from right to left.

Cases c and d shown in Fig.2.7 correspond to a *weaker* particle, where the strength of the particle is 2/3 of the strength of the matrix. It is interesting to note from these figures that for both the stiffer and the softer particle cases, a secondary microcrack nucleates inside the particle due to the stress field of the main approaching crack and eventually both cracks coalesce. Some small differences can be observed between cases c and d in Fig.2.7 (stiffer and softer particle cases), where it can be seen that the main crack gets attracted towards the softer particle earlier than the stiffer particle. This is due to the fact that, in case of a stiffer particle, only the (lower) strength makes the crack change its direction towards the particle, whereas in case of a softer particle, both the stiffness (tendency of softer particle attracting a crack) and the lower strength play a role in the crack path. Despite these differences, the effect of the elastic mismatch is relatively unimportant in these cases, when it comes to the fracture mechanism.

In cases e and f in Fig.2.7, crack paths are reported in which the toughness of the particle is one order of magnitude higher than the toughness of the matrix, while the particle strength is kept lower, as in cases c and d. Comparing cases e and f with the

corresponding cases c and d, it can be observed that increasing the fracture energy (toughness) does not prevent the deflection of the main crack towards the particle. One notable difference between cases e and f is that for the stiffer particle (case e), the main crack coalesces with the secondary crack in the matrix, after it has passed the particle, whereas coalescence occurs inside the particle in case f. This difference can be attributed to the mismatch in elastic properties (in case f, the softer particle further attracts the main crack).

Based on the results shown in Sec. 2.3.2 and Sec. 2.3.3, it can be concluded that a purely energy-based fracture mechanics approach, which cannot consider the mismatch in strength, would fail in capturing relevant fracture scenarios since it could not account for a secondary crack initiation. Thus, a purely energy-based criteria may over-emphasize the role of the mismatch in elastic properties in predicting crack paths. The effect of the mismatch in elastic properties is not discussed in detail as it has been explored extensively in the literature. However, for completeness, the effect of the mismatch in elastic properties is analyzed in the following section within the context of the current framework that accounts for both strength and toughness.

2.3.4. EFFECT OF MISMATCH IN ELASTIC PROPERTIES: FRACTURE MAP

The influence of the elastic mismatch is analyzed by considering three different modulus ratios, namely $E^{\mathrm{p}}/E^{\mathrm{m}} = 3,1$ and $1/3$. In all cases, the main approaching crack has an initial offset of $c = r/2$ (i.e., the particle lies directly in front of the path of the primary crack). The results of a large number of simulations is conveniently summarized in the form of a fracture map (i.e., failure-mechanism map), as shown in Fig. 2.8. For each mismatch in elastic properties, the corresponding curve shown in Fig. 2.8, called a *transition* curve, separates the regions of the fracture strength $\sigma_{\mathrm{c}}^{\mathrm{p}}/\sigma_{\mathrm{c}}^{\mathrm{m}}$ and fracture toughness $G_{\mathrm{c}}^{\mathrm{p}}/G_{\mathrm{c}}^{\mathrm{m}}$ for which an approaching crack would either break the embedded particle or not. In particular, the regions to the left and bottom of a curve correspond to particle fracture and the regions to the right and top of the curve correspond to crack deflection. In order to determine the curves shown in Fig. 2.8, a large number of simulations need to be carried out to identify the corresponding strength and fracture energy ratios where the transition from case 1 to case 2 occurs (the curve itself is an interpolation between the properties of the nearest points where the transition is observed). It should be noted that, for each mismatch in elastic properties, a single transition curve was identified in the fracture map.

The general trend is that particle fracture is favored with a decrease in stiffness of the particle. This is qualitatively in accordance with a general conclusion established in the literature that indicates that a softer particle attracts the approaching crack and a stiffer particle deflects the approaching crack away from it. However, the fracture behavior is significantly dependent upon the mismatch in fracture properties as seen in Fig. 2.8. It is also observed that the interplay between the mismatch in fracture strength and toughness is more pronounced for softer particles (e.g., $E^{\mathrm{p}}/E^{\mathrm{m}} = 1/3$) than for stiffer particles (e.g., $E^{\mathrm{p}}/E^{\mathrm{m}} = 3$). It is interesting to note that particle fracture occurs in case of softer particle, even if the fracture strength of the particle is higher

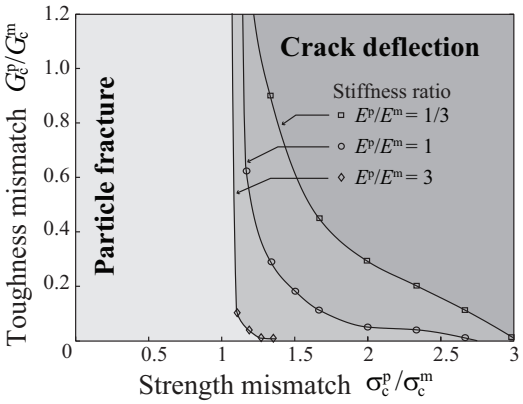

Figure 2.8: Fracture map: Effect of mismatch in elastic properties. Three stiffness ratios are considered corresponding to stiffer particle, particle with same stiffness of the matrix and softer particle. The curves shown are obtained for an offset $c = r/2$. The transition curves correspond to the boundary separating the regions in which particle fracture or crack deflection occurs, as a function of the strength mismatch σ_c^p/σ_c^m and the toughness mismatch G_c^p/G_c^m.

2

that that of the matrix by a factor of 2 or even more, provided the fracture toughness of the particle is sufficiently low. In case of stiffer particle, particle fracture is precluded if the strength of the particle is higher by a factor of 1.3 relative to the matrix strength, irrespective of lower fracture toughness of the particle.

2.3.5. FRACTURE MAPS FOR A PERFECTLY-BONDED, UNDAMAGED PARTICLE

Similar to the results presented in the previous section, it is convenient to summarize the results of a large number of simulations for distinct offsets c. In this case, the mismatch in elastic properties is set to $E^p/E^m = 3$ (stiffer particle) for all simulations.

Distinct types of transitions from one case to the other have been observed in the simulations, corresponding to distinct changes in crack patterns. Crack paths for the different offsets are not reported here, rather the fracture maps corresponding to different offsets are shown in Fig. 2.9. For all offsets analyzed, if the mismatch in toughness G_c^p/G_c^m is sufficiently high, the transition curves depend mostly on the mismatch in fracture strength σ_c^p/σ_c^m (i.e., all transition curves are nearly vertical for $G_c^p/G_c^m > 0.6$). Correspondingly, the mismatch in fracture strength is the deciding factor in order to predict whether particle fracture or crack deflection would occur. However, if the mismatch in toughness is sufficiently low (e.g., $G_c^p/G_c^m < 0.4$), then the transition curve is slightly influenced by this parameter. Nonetheless, for any considered offset, it is observed that particle fracture does not occur even for very low toughness of the particle, if the strength of the particle is higher than that of the matrix by a factor of 1.3.

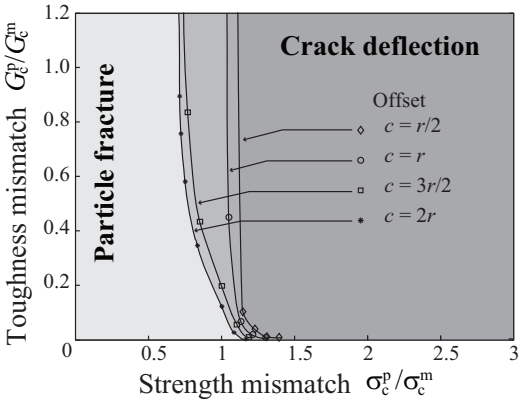

Figure 2.9: Fracture map for a perfectly-bonded, undamaged particle: Effect of particle offset. The curves shown are obtained for the stiffness ratio, $E^p/E^m = 3$. For four distinct initial offsets c, the curves shown correspond to the boundary separating the regions in which particle fracture or crack deflection occurs, as a function of the strength mismatch σ_c^p/σ_c^m and the toughness mismatch G_c^p/G_c^m.

It is worth recalling that the fracture map shown in Fig. 2.9 corresponds to a significantly stiff particle, relative to the matrix, with $E^p/E^m = 3$. It is well-known that stiffer particles tend to deflect incoming cracks. Nonetheless, it is interesting to observe that for the offset $c = r/2$, i.e., when the particle is in front of the incoming crack path, the primary matrix crack can directly break an equally stronger particle even if it is tougher and stiffer than the matrix (i.e., $\sigma_c^p/\sigma_c^m \approx 1$ for $G_c^p/G_c^m > 1$ and $E^p/E^m = 3$). Furthermore, particles can break even if they are not in the path of the incoming crack (i.e., for $c \geq r$) provided that the particle strength is sufficiently low. This situation arises when the particle is subjected to the influence of the approaching crack stress field and a secondary crack is generated inside the particle. The secondary crack may grow into the matrix and coalesce with the incoming primary crack, effectively generating particle fracture even if the primary crack does not (directly) break the particle. Hence, despite the tendency of stiffer particles to deflect incoming cracks, the influence of the elastic stiffness on the interaction between an incoming crack and the particle is in general secondary and the behavior depends mostly on the fracture properties. Elastic properties do play a role in the fracture process as discussed in the previous section. Nonetheless, the point emphasized here is that for a fixed elastic property mismatch, the influence of the fracture property mismatch is much more pronounced than the considered mismatch in elastic stiffness.

2.4. EFFECT OF PRE-EXISTING FLAWS INSIDE THE PARTICLE

In Sec.2.3 it was assumed that the particle was initially undamaged. Typically, however, flaws can occur during processing of the composite material or they can be inherent to the material itself (e.g., brittle particles). As a consequence, the expected strength gain

may not be achieved as these flaws can weaken the system instead of strengthening it. Thus, for practical applications, it is important to study the effect of such flaws as they may significantly affect the anticipated performance of a composite. To study the effect of pre-existing flaws on the fracture behavior, a single representative flaw, located in the center of the particle, is considered in the simulations reported in this section. The flaw is initially confined to the interior of the particle and the particle/matrix interface is assumed to be perfectly bonded (simulated with a sufficiently large interface strength).

Two main geometrical parameters of the flaw are varied in a parametric analysis, namely its initial size and its orientation with respect to the main approaching crack. All parametric analyses carried out for distinct geometrical characteristics of the flaw are obtained with the same fracture length scale of the matrix used in Sec. 2.3, namely $\bar{l}^{\mathrm{m}}_{\mathrm{fpz}} = 1.1 \times 10^{1}$. However, an additional parametric analysis is conducted in this section, namely for distinct values for the matrix fracture length scale $\bar{l}^{\mathrm{m}}_{\mathrm{fpz}}$, in order to investigate the effect of this quantity on the fracture behavior.

As pre-existing flaws are most often observed in stiff and brittle particles (compared to softer particles) only the stiffer particle case is considered in this section ($E^{\mathrm{p}}/E^{\mathrm{m}} = 3$). All the analyses are carried out for the particle offset $c = 3r/2$, which is representative of a particle that does not lie ahead of an approaching crack.

2.4.1. MECHANISM OF CRACK-PARTICLE-FLAW INTERACTION

To demonstrate the effect of the particle flaw and establish a link between a fracture map and a fracture mechanism, it is useful to first illustrate one representative sequence of a crack-particle-flaw interaction. A particle with a flaw of size r is shown in Fig. 2.10, where r is the radius of the particle. To focus on the effect of the flaw, the fracture properties for the particle and the matrix are kept the same. Upon loading, it can be observed that there are two different stress fields, one for the main crack and the other associated with the flaw inside the particle as seen in Fig. 2.10a. Despite the stress concentration inside the particle, the flaw does not initially grow (recall that the stress predicted using a cohesive zone approach is finite). However, once the main crack approaches the particle as shown in Fig. 2.10b, the two stress fields interact with each other leading to further amplification of the stresses inside the particle. Eventually a secondary crack is activated starting from the tip of the flaw. Upon further loading, the secondary crack originated from the flaw grows further and attracts the approaching main crack towards the particle, finally resulting in coalescence with the main crack as observed sequentially in Fig. 2.10c and Fig. 2.10d. This crack advancement mechanism is somewhat similar to cases studied in Sec. 2.3, except that the possibility of appearance of a secondary crack is increased due to the presence of the flaw. The initial location of this secondary crack is mostly dependent upon the location of the flaw. The quantitative effect of the flaws is studied in the next subsections based on flaw size and flaw orientation.

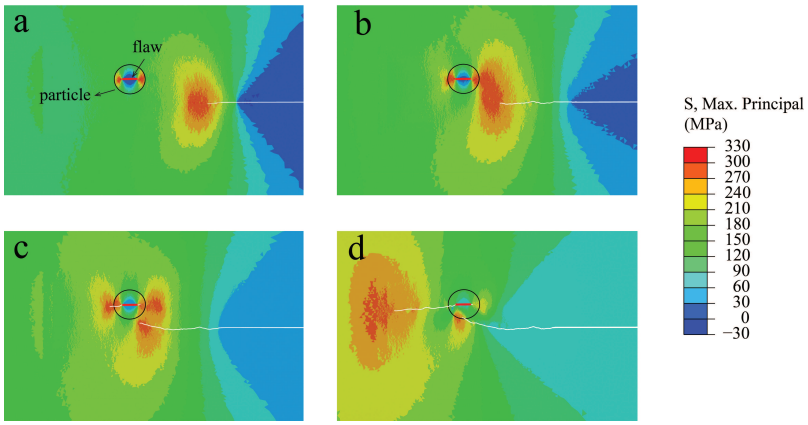

Figure 2.10: Crack-flaw interaction: a) two different stress fields corresponding to the flaw and the main crack, b) the initial interaction between the two stress fields, c) a secondary crack initiating from the flaw and simultaneously the main crack getting attracted towards the flaw, d) further coalescence of the flaw-induced secondary crack and the attracted main crack.

2.4.2. EFFECT OF FLAW SIZE

Four different flaw sizes in the particle, namely $r/4$, $r/2$, r and $4r/3$, are considered in order to simulate the range from small to large flaws. Their effect can also be compared to the undamaged particle case studied in Sec. 2.3 (i.e., no flaw). The corresponding results with a crack that has an initial offset $c = 3r/2$ are shown in Fig. 2.11. In all cases the fracture strength and the toughness are the same for both the particle and the matrix in order to focus on the influence of the flaw. It can be observed that flaws with sizes equal to $r/4$ and $r/2$ (cases a and b) do not significantly alter the crack path compared to the case of an undamaged particle. In contrast, larger flaws, namely r and $4r/3$, have an important effect as can be observed in cases c and d in Fig. 2.11. Hence, these results indicate that there is a critical flaw size (in this case somewhere between $r/2$ and r), for which the crack response changes from crack deflection (case 1) to particle fracture (case 2). The critical flaw size corresponds to the minimum length for which a secondary crack can nucleate and grow from the flaw tip (i.e., there is sufficient stress concentration to both nucleate and subsequently propagate a secondary crack).

In order to globally assess the effect of flaw size on the crack path, a wide range of fracture properties of the particle relative to the matrix are considered. The results corresponding to different flaw sizes are summarized in the form of fracture maps in Fig. 2.12, for a representative offset, namely $c = 3r/2$. Essentially, each transition curve indicates the locus of material properties for which the flaw size is critical. As it can be clearly observed from the results, the presence of a particle flaw shifts the transition curve upwards and towards the right simultaneously (higher particle strength and toughness), favoring particle fracture with increased flaw size compared to the case with no flaw.

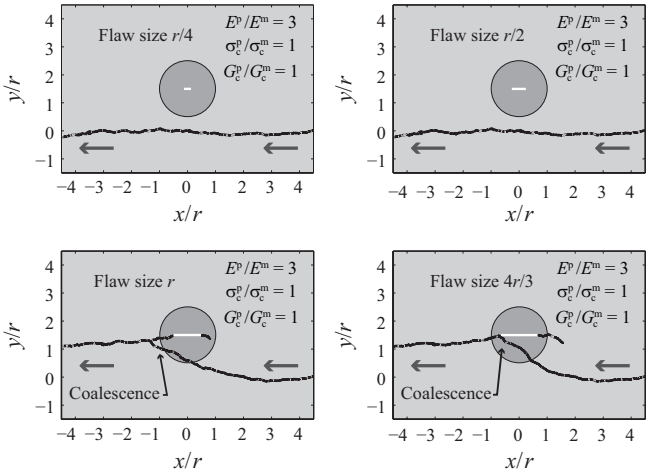

Figure 2.11: Crack patterns for different flaw sizes, In all cases, the particle is stiff and the particle and matrix have equal fracture properties. The crack path is from right to left.

It is interesting to note that the fracture map curve for the no flaw case is almost vertical, implying that the failure mechanism is dominantly controlled by fracture strength only. However, if a flaw is introduced, failure is also controlled by fracture toughness, a dependency that can be traced back to the secondary crack mechanism as indicated in Sec. 2.4.1. In general, for sufficiently large particle toughness, the transition between particle fracture to crack deflection is dominated by the mismatch in strength (near vertical lines), while for sufficiently large particle strength, the transition is dominated by the mismatch in toughness (near horizontal curves). Nonetheless, it is worth indicating that for particles with very low relative toughness, the transition between fracture mechanisms (case 1 and 2) eventually does occur at a finite value of the strength mismatch σ_c^p/σ_c^m, albeit a large one (i.e., although not shown for the flaw sizes r and $4r/3$, the transition curves eventually intersect the horizontal axis). For intermediate cases, both strength and toughness play equally important roles. For the flaw sizes $r/4$ and $r/2$, the transition lines are very close to the one with no flaw for sufficiently large values of G_c^p/G_c^m, implying that particles may have flaws but that their *effective* strength is not significantly affected if the particle toughness is sufficiently high.

2.4.3. EFFECT OF FLAW ORIENTATION

The results displayed in the previous section were obtained assuming that the flaw was aligned with the main incoming crack. However, typically flaws and cracks are not aligned and it is anticipated that the critical flaw size will strongly depend on the relative orientation. To quantify this assertion, for a flaw of size equal to r, different

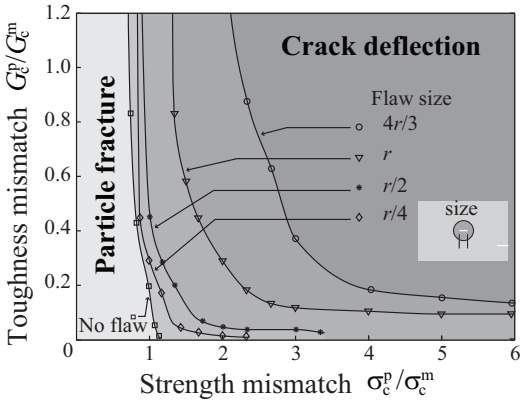

Figure 2.12: Fracture map: Effect of pre-existing flaws inside a perfectly-bonded particle for an offset $c = 3r/2$. The transition curves indicate the points for which the flaw size is critical and a secondary crack emanates from the flaw.

representative flaw orientations were analyzed, namely 0°, 30° , 60° and 90°, where each angle indicates the relative orientation of a flaw with respect to the incoming crack. The corresponding fracture maps are shown in Fig.2.13.

Among the four different orientations analyzed, the flaw aligned with the incoming crack (i.e., 0°) is the most critical. This due to the fact that the 0°-oriented flaw is mostly loaded in mode I conditions, which favors the nucleation and growth of a secondary crack emanating from the flaw. Hence, the particle with 0° flaw will have the least resistance to particle fracture compared with the other three flaw orientations. The flaw orientation 90° corresponds to the least favorable conditions for crack nucleation and propagation. Nonetheless, even the presence of the 90°-oriented flaw can alter the crack path, provided the toughness is sufficiently low. This is because the mismatch in elastic properties and the non-symmetric stress field related to the approaching primary crack may lead to a local mixed-mode condition in which a crack can be activated in the flaw. In general, it can be concluded that the presence of a flaw clearly decreases the resistance to particle fracture; the *smallest* critical flaw size corresponds to the case where the flaw and the incoming crack are aligned.

2.4.4. EFFECT OF FRACTURE LENGTH SCALE PARAMETER

Cohesive zone models contain an intrinsic fracture process zone length as defined in (2.1) for the matrix material. Consequently, in a particle-matrix system, it is possible to compare the size of the particle to the intrinsic matrix fracture length by introducing a fracture length scale parameter, as given in (2.8). The influence of this length scale parameter on the fracture behavior in the particle-matrix system is examined by considering a wide range of matrix toughnesses, namely $G_c^m = 10^n$ J/m^2, with $n = 0,1,2,3,4$, resulting, respectively, in five different length scale parameters, i.e.,

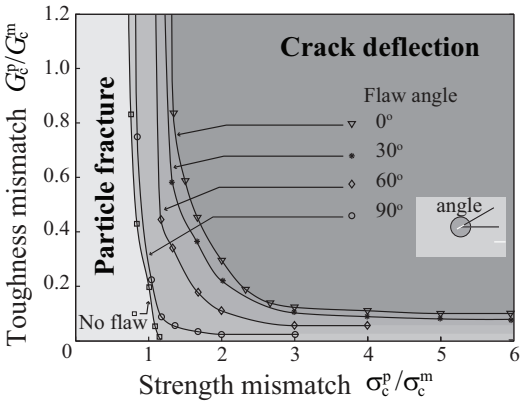

Figure 2.13: Fracture maps: Effect of flaw orientation for a flaw size equal to r and an initial crack offset $c = 3r/2$.

2

$\bar{l}^m_{fpz} = 1.1 \times 10^m$, with $m = -1, 0, 1, 2, 3$. Recall that the reference value used in the previous sections was $G^m_c = 10^2$ J/m^2 , which corresponds to $\bar{l}^m_{fpz} = 1.1 \times 10^1$. The simulations in this section are conducted with a flaw in the particle of size $r/2$, which is aligned with an incoming crack that has an offset $c = 3r/2$. The transition curves from particle fracture to crack deflection are plotted in Fig.2.14 for each fracture length scale parameter.

From the Fig.2.14, it may be observed that, when the fracture process zone length is very large relative to the particle size (i.e., $\bar{l}^m_{fpz} \gg 1$), the mismatch in fracture strength becomes the dominating factor. For example, for the length scale parameters $\bar{l}^m_{fpz} = 1.1 \times 10^2$ and $\bar{l}^m_{fpz} = 1.1 \times 10^3$, the corresponding fracture map is almost vertical, signifying that it is predominantly the mismatch in strength that plays a role in determining the point in which the fracture mechanism changes. It is worth pointing out that, for the length scale parameter, namely $l^m_{fpz}/r = 1.1 \times 10^3$, (plotted as dotted curve in the figure for the purpose of clarity) the fracture map is essentially vertical, with a transition curve defined by a single value of the strength mismatch, namely $\sigma^p_c/\sigma^m_c = 1.3$. This behavior can be explained as follows: If the length scale is very large for the matrix (hence for the particle as well, as particle fracture properties are varied relative to the matrix), then the characteristic stress field associated with such large fracture process zone involves dissipation (amount of energy spent in formation and extension of process zone) of the specified fracture energy over a very larger length of the process zone. Under such conditions, the *extension* of the *cohesive* crack tip of either the main crack in the matrix or the flaw within the particle over a considered length relative to the particle size would only require a very small fraction of the specified fracture energy of the particle and the matrix. Hence, any mismatch in fracture energy between the particle and matrix, in general, would have a

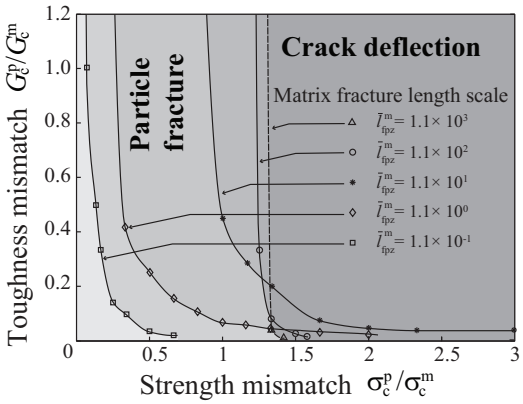

Figure 2.14: Fracture maps: Effect of fracture length scale parameter for a particle with a flaw of size $r/2$ and an incoming crack with an offset $c = 3r/2$.

negligible effect on the crack path. Consequently, the extension of the cohesive crack tip is controlled predominantly by the mismatch in the strength, resulting in vertical transition curves for very large length scales, namely $\bar{l}^{m}_{fpz} = 1.1 \times 10^2$ and $\bar{l}^{m}_{fpz} = 1.1 \times 10^3$. Furthermore, for increasing fracture length scales, it has been observed that there exists a limit for the value of strength mismatch above which particle fracture does not occur. This can be observed by comparing the nearly vertical transition curves in the Fig.2.14 corresponding to the length scales, $\bar{l}^{m}_{fpz} = 1.1 \times 10^2$ and $\bar{l}^{m}_{fpz} = 1.1 \times 10^3$.

Conversely, for lower values of the length scale, toughness mismatch also plays a prominent role in deciding the fracture mechanism. This is because, if the material fracture process zone length is small relative to the particle size, the energy dissipated over the considered extension of the cohesive crack tip (of the propagating matrix crack or the crack inside the particle) becomes significant and contributes to a larger fraction of the specified fracture energy. In this case, the mismatch in fracture energy between the particle and the matrix becomes important to trigger the propagation of the pre-existing flaw within the particle. In the limit case of infinitesimally small length scale, the particle is mostly subjected to the same stress field used in linear elastic fracture mechanics, which is theoretically recovered in the limit $\bar{l}^{m}_{fpz} \to 0$. In that case, it is to be expected that the energy dissipated is crucial. Thus, for intermediate and small fracture length scales, both strength and fracture energy mismatch have an effect on the fracture behavior. The results on the effect of fracture process zone length agree well qualitatively with the work in [PT06], in the sense that the mismatch in strength is the controlling factor for larger length scales, though the problems analyzed are different.

2.5. EFFECT OF INTERFACE FRACTURE PROPERTIES AND INTERFACE FLAWS

In the previous sections, the bonding between the particle and the matrix was assumed to be perfect. This was modelled by assigning sufficiently high values to the interface strength σ_c^i and the interfacial fracture energy G_c^i (delamination toughness). Consequently, cracks in the vicinity of the interface could only run across or remain close to the interface. However, in many particle/matrix systems, the interface between the particles and the matrix may have a lower strength and toughness than that of the bulk materials. In some cases, it is possible that no adhesion is achieved between the particle and the matrix in portions of the interface (i.e., there is an *interface flaw*). These two issues are analyzed in this section, namely the influence that the interfacial fracture properties and the presence of interfacial flaws have on the trajectory of an incoming crack.

2.5.1. INFLUENCE OF FRACTURE PROPERTIES OF THE INTERFACE

The simulations in this section are carried out for a primary crack with a representative offset ($c = 3r/2$), for the reference non-dimensional value of the fracture length scale of the matrix $\bar{l}^m_{\text{fpz}} = 1.1 \times 10^1$ and for a particle without an internal flaw (but possibly an interfacial flaw). To focus on the effect of the interfacial properties and flaws, the fracture properties of the particle and matrix are kept the same for all the simulations in this section. Both the stiffer ($E^p/E^m = 3$) and softer ($E^p/E^m = 1/3$) particle cases are considered. When the interface is allowed to break, a new fracture mechanism is available, namely *interface delamination*. However, for simplicity, only selected examples are shown instead of a fracture map. In particular, crack patterns when the interface strength is equal to 2/3 of the matrix strength (which is equal to particle strength), are shown in Fig. 2.15. The results corresponding to the stiffer and softer particle cases are shown in the left and right sides of the figure, respectively. Cases a and b are obtained with an interfacial toughness equal to that of the surrounding phases (particle and matrix), whereas in cases c and d the interfacial toughness is one order of magnitude higher.

In all cases shown in Fig. 2.15, a secondary crack appears at the interface and eventually coalesces with the main crack. This is in contrast to the case of perfect particle bonding (cases a and b in Fig. 2.7), where the crack runs in the matrix and does not reach the interface. It is relevant to observe that in the cases shown in Fig. 2.15, strictly speaking, the particle itself does not crack but, rather, the interface separates. Furthermore, as may be observed in cases c and d, an increase in the interfacial fracture energy does not prevent the interface from separating, which indicates that this is a phenomenon that is mostly controlled by the interfacial strength (i.e, if the interface strength is reduced below a certain limit, debonding always occurs irrespective of the interface fracture energy).

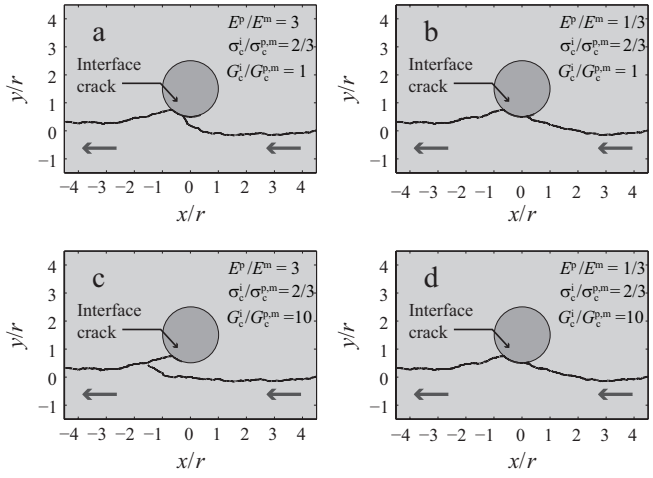

Figure 2.15: Crack paths for particle offset case, $c = 3r/2$: effect of interface fracture properties; crack path is from right to left.

2.5.2. FLAW IN INTERFACE

Flaws in the particle/matrix interface may be generated during processing leading to poor or no bonding in some parts of the interface. To provide insight on the consequences that this lack of bonding has on the interaction between an incoming crack and a particle, selected interfacial flaw configurations, in terms of size and their location, are considered. The simulation conditions are similar to the ones indicated in Sec. 2.5.1, except that the interfacial strength and toughness are chosen equal to that of the surrounding phases in order to focus on the effect of the interfacial flaw. For simplicity, only the stiffer particle case ($E^p/E^m = 3$) is considered in this section. Three representative locations of a flaw on the interface are considered, designated as bottom, middle and top, where bottom refers to the portion of the particle/matrix interface closest to an incoming crack with an offset $c = 3r/2$. Several sizes were considered for the flaws in the three aforementioned positions. In all three locations, a critical flaw size was identified such that the flaw attracts the main crack irrespective of the high strength and fracture energy for the rest of the interface (i.e., for any value of $\sigma_c^i \geq \sigma_c^{p,m}$ and $G_c^i \geq G_c^{p,m}$). The crack paths associated with the critical sizes for flaws located at the bottom, middle and top locations are shown in Fig. 2.16 (cases a, b and c, respectively). For flaws smaller than the critical value, the crack pattern is *qualitatively* similar to the one shown in case a in Fig. 2.7 (i.e., the crack runs in the matrix, similar to the perfect bonding case). The critical length is quantified in each case in terms of the angle subtended by the flaw, i.e., 15°, 120° and 90° for cases a, b and c, respectively (in which case the critical length is computed as θr, where θ is the angle measured in radians and r the radius of the particle). The smallest critical

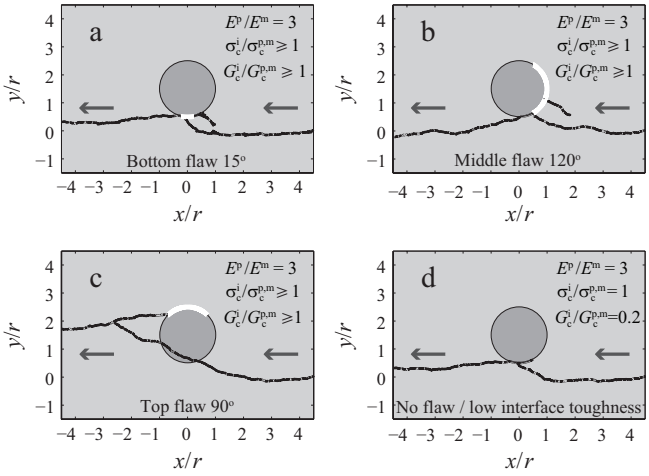

Figure 2.16: Effect of interface flaw on crack path; crack path is from right to left.

length corresponds to the bottom flaw due to its proximity to the incoming crack and the fact that it is essentially oriented in the same direction as the crack. In contrast, the largest critical length corresponds to the middle flaw, since it is not favorably oriented in order to trigger further interface debonding. The critical length for the top flaw is bounded between the smallest and the largest critical sizes analyzed; it is interesting to observe that in this case (case c in Fig. 2.16), the failure mechanism involves both particle fracture and debonding as the main crack traverses the particle. In contrast, only particle debonding is observed in cases a and b.

For comparison purposes, a fourth case is included in Fig. 2.16, namely case d in which no flaw is present but the interfacial toughness is reduced up to a point where debonding and subsequent coalescence occurs at the bottom of the particle. This situation is similar to the crack patterns previously observed in case a in Fig. 2.15 and case a in Fig. 2.16. From these cases, it may be concluded that debonding and coalescence may be triggered due to (i) low interfacial strength, (ii) low interfacial toughness or (iii) the presence of a flaw (despite a high interfacial strength and toughness).

2.6. CONCLUDING REMARKS

Numerical simulations using a cohesive zone model were carried out to analyze the influence that a particle embedded in a matrix has on the trajectory of a crack. Complex interactions can be observed between the crack and the particle in some cases, with an overall crack advancement composed of a sequence of nucleation, propagation and coalescence of secondary cracks in the particle or the matrix. A summary of distinct

failure mechanisms (particle fracture, crack deflection and interface debonding) were reported for a wide range of combinations of fracture properties of the matrix, particle, interface and under the presence of flaws in the particle or the interface. From the simulations, the following general conclusions were drawn:

- The trajectory of a crack is primarily dependent upon the fracture properties, while elastic properties often (though not always) play a secondary role.
- The mismatch in strength between the particle and the matrix was found to be the dominant factor affecting the fracture behavior in undamaged, perfectly bonded particles. Above a critical value of the strength mismatch, crack deflection occurs regardless of the toughness mismatch.
- Toughness mismatch (i.e., mismatch in fracture energies of particle and matrix) also plays an important role in determining the crack path if flaws are present in the particle.
- The mismatch in strength is the dominant factor, even in the presence of a flaw, if the matrix cohesive zone length is sufficiently large (i.e., when the matrix material has a more ductile-like fracture behavior).
- The effect of fracture properties of the interface is critical in deciding the crack path. Further, presence of interface flaws highly favors debonding of the particle/matrix interface.

For design purposes, it is important to fine-tune the mismatch in mechanical properties when a given outcome is required. In particular, for particles embedded in a matrix for self-healing purposes, the present study indicates that a very good bonding between the particles and the matrix is required while, simultaneously, particles should have a sufficiently small fracture strength. With this combination, a self-healing mechanism can be successfully triggered by the incoming crack, which itself needs to be healed.

3

MICROSTRUCTURE-BASED CRACK PROPAGATION ANALYSIS

In the previous chapter, a comprehensive study has been conducted to establish the guidelines for selection and design of healing particles. However, the analyses focused on an idealised single-particle matrix system, which may not be representative of a realistic particle dispersed self-healing materials. Hence, in this chapter, the computational fracture analysis is extended to a system containing multiple particles, which is more representative of an actual microstructure in a self-healing TBC. The composite microstructure, under consideration, contains particles made out of molybdenum disilicide ($MoSi_2$) embedded in an Yttria Stabilised Zirconia (YSZ) matrix, which is commonly used in TBC systems. It is to be noted that the $MoSi_2$ particles are the actual healing agents dispersed in the YSZ matrix to achieve an extrinsic self-healing TBC system [STD+15]. The analyses, in addition to reporting the crack paths in the microstructure, aim to quantify the effect of the particle and the interface properties on the overall mechanical properties of the self-healing particulate composite. The results of the parametric simulations are summarised in terms of the macroscopic stress-strain response of the composite. The fracture behaviour in terms of strength of the composite is reported as a function of the mismatch in fracture properties between the healing particles and the matrix. The number of instances of fracture of healing particles is quantified as a function of the property mismatch, a relevant result in the context of healing activation. The effect of the interface properties is analysed and the composite strength is reported as a function of interface strength and fracture energy. Further, the effect of mode mixity on the interface fracture is elucidated by considering different strength values for normal and shear modes of fracture. The study could be used as a guiding tool while designing an extrinsic self-healing material and understanding the effect of the healing particles on the overall mechanical properties of the material.

3.1. INTRODUCTION

Microstructure-based finite element simulations have been conducted in the literature to analyse fracture and damage in particulate composite systems [AC07, AC06, CMM+06, SPP10, QL15, Qin14, LZ13a, LZ13b, MDB04]. In [AC07, AC06], microstructures representing a random distribution of irregularly shaped SiC particles in an aluminum matrix were simulated using two-dimensional linear elastic approach involving stress intensity factor as the crack driving force. The effect of particle clustering was quantified and the resulting crack paths were compared with experiments. In a different work [CMM+06], the actual microstructure of the particulate composite was modelled by mapping the Scanning Electron Microscope (SEM) images onto the finite element mesh. They investigated the effects of pore defects and residual stresses on the crack path by employing Griffith's energy-based fracture mechanics approach. In [SPP10], an elastoplastic finite element analysis was conducted on an SEM-based finite element model and the stress-strain response was reported as a function of microstructural features such as particle clustering. A comprehensive investigation of the effect of distribution, size and shape of the particulate reinforcements and interphase properties on the fracture behavior of a Al_2O_3/TiB_2 composite has been conducted in [LZ13a, LZ13b]. Employing a J-integral concept and using cohesive zone approach to simulate fracture in the matrix, the particle or the interface, the effective fracture toughness of the composite is quantified. It is worth mentioning that all of the analyses summarised above are performed in a two-dimensional framework. Some efforts were taken to conduct three-dimensional crack propagation analysis in particulate composites [WSLC12, ZOG+16, GGP17], but the computational cost associated with such simulations limits the scope of such studies. For instance, the size of the microstructure, in terms of number of particles, that can be analysed in the three-dimensional framework is limited. Further, the computational intensity prevents the possibility of conducting a series of parametric analysis to explore the influence of constituent properties.

In the context of self-healing particulate composite systems, very few modelling studies have been conducted in the literature in terms of effective mechanical properties and crack path predictions [GGP17, GVT+17, QZR15, LJYY16]. For instance, in [QZR15, LJYY16], efforts are taken to estimate the effective elastic properties of the self-healing particulate composites, whereby the effect of dispersed healing particles on elastic moduli of the host matrix material is quantified. In [GGP17], crack propagation studies were conducted in an idealized healing capsule(s)-matrix system and the effects of geometric and material parameters were analysed using cohesive and XFEM techniques. In particular, a self-healing concrete in a three-point bending test set-up is utilised to evaluate the influence of parameters such as number of capsules, size and position on the mechanical behaviour of the concrete. This is then followed by modelling an idealised single healing capsule-matrix volume element, whereby the influence of interface properties and capsule volume fraction on the effective strength was reported. Nonetheless, studies dealing with the analysis of fracture in particulate self-healing materials in a realistic microstructure could provide practical insights

enabling optimal design of the material. It is thus the objective of this chapter to study the crack propagation in a real microstructure of a self-healing particulate composite, followed by quantification of the effect of healing particles and their properties on the composite mechanical properties.

Two key aspects are addressed in this chapter. Firstly, the effect of fracture properties of the particle and the interface fracture properties on the crack path are analyzed numerically using a finite element model generated directly from the actual microstructure of the $MoSi_2$-YSZ composite obtained from the SEM image. The results are compared with experimental observations from fracture tests conducted on the composite. The second aspect dealt with in this chapter is the investigation of the effect of mismatch in properties of the constituents and the interface on the overall mechanical behaviour of the composite. For an ideal self-healing system, one of the requirements is that introduction of healing particles into the base material should not deteriorate its mechanical characteristics. In other words, the healing particles should not degrade the stiffness, the strength and the fracture toughness of the base material. The factors that influence the above-mentioned mechanical properties of the resulting particle-dispersed composite include the properties of the particle and the particle-matrix interface. It is, therefore, the goal of the present chapter to investigate the effect of the particle and the interface properties on the global mechanical properties of the composite, utilising the microstructure-based crack propagation analysis. The motivation is to reveal the roles of these parameters to experimental researchers which could be helpful in the design and development of self-healing systems with least compromised mechanical property values of the original base material. This is achieved through numerical analysis using a finite element model generated directly from an actual microstructure of the $MoSi_2$-YSZ composite obtained from an SEM image [KMZC+16]. The motivation is to reveal the roles of these parameters to experimental researchers which could be helpful in the design and development of self-healing systems with least compromised mechanical property values of the original intact base material.

3.2. MICROSTRUCTURE AND FINITE ELEMENT MODEL

The composite microstructure is shown in Fig. 3.1 in which $MoSi_2$ particles, the discontinuous phase, are randomly dispersed in the YSZ matrix. The nominal volume fraction of the $MoSi_2$ particles was 20%. Additional information of the composite material such as manufacturing process, details of the material constituents of the composite can be found in [KMZC+16]. The figure shown in Fig. 3.1 was generated through post-processing of an SEM image of the composite cross-section, following which the microstructure is translated into a finite element mesh.

The microstructure is meshed using two-dimensional three-node plane-strain elements (CPE3) for the particle and the matrix phases, to model their bulk constitutive behaviour. In order to simulate fracture, the initial finite element mesh was modified using a Matlab pre-processing script to include four node cohesive elements (COH2D4) throughout the solid elements. This process of embedding cohesive

elements throughout the mesh introduces potential crack faces necessary to simulate all the relevant fracture mechanisms such as interface debonding, particle fracture and matrix cracking. As discussed in chapters 2 and 7, such an approach naturally triggers the issue of mesh dependency in terms of the artificial compliance and the converged crack path. This aspect has been taken into consideration and subsequently resolved using the guidelines derived from the mesh dependency study in Sec.7.1. The resulting finite element mesh consists of 1063157 elements of which 637716 elements are the cohesive elements and remaining 425441 elements are plane-strain bulk elements. For the bulk plane-strain elements in the particle and the matrix phases, a linear elastic and isotropic constitutive behaviour is assumed. For the cohesive elements, a bilinear cohesive constitutive relation is utilised, see chapter 2, through which appropriate fracture properties (strength and fracture energy) are considered for failure modelling in the particle, the matrix and the interface.

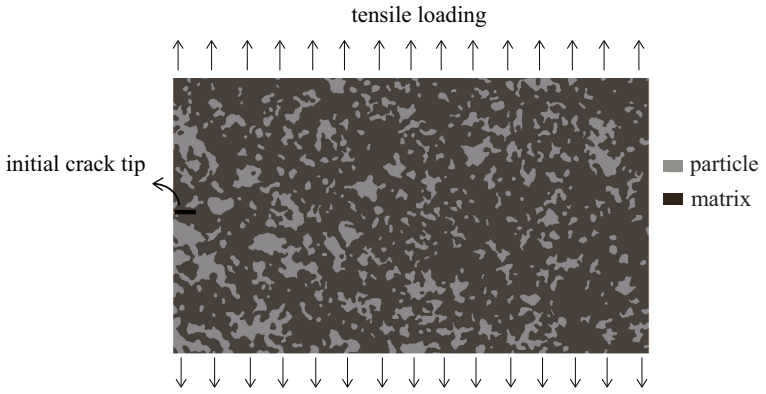

Figure 3.1: Loading conditions for a particle-matrix composite system. Cohesive elements were embedded within all elements of the finite element mesh (not shown here for clarity). The finite element mesh was generated after processing an SEM picture of ($MoSi_2$) particles (lighter phase) embedded in Yttria Stabilised Zirconia (YSZ, darker phase). An initial precrack was included on the left side. The length and the width of the specimen are equal to 0.7 mm and 0.4 mm respectively.

Note that the microstructure considered in the analysis is a cross-section of the particulate composite. Hence, the two-dimensional finite element model of the microstructure does not entirely reproduce the microstructural features as the three-dimensionality is naturally lost in the model. As a matter of fact, the finite element model assumes that the cross-section of the particles is extruded in the third direction representing cylindrical inclusions rather than the actual particles. Despite these limitations, the microstructure-based fracture analysis in a two-dimensional framework is undertaken to reveal qualitative and some quantitative information in terms of the fracture mechanisms and the mechanical properties of the composites. For instance, in [KMZC+16], effective thermal properties of the composite are obtained through a two-dimensional finite element analysis on the microstructures of the same composite material considered in this work. In the context of fracture

study, three-dimensional crack propagation analyses would not be feasible due to the intensive computational costs associated with three-dimensional cohesive elements throughout the domain. Also, reconstruction of three-dimensional microstructure is needed for such an analysis, which in itself is a separate challenge. In the end, two-dimensional fracture analyses can be effectively used as a pragmatic approach to understand the effect of properties of the constituents (particle, matrix and interface) on the crack path, a crucial information for self-healing material design.

The finite element model is subjected to a global mode-I loading by prescribing traction on the upper and lower edges of the specimen, which contains a small edge pre-crack on the left as shown in the Fig. 3.1. With reference to [SS03, SA04], the elastic properties used for the particle and the matrix are as follows: Young's modulus of the YSZ matrix is taken as E^{m} = 150 GPa and that of the $MoSi_2$ particle is given as E^{p} = 450 GPa. Poisson's ratio of the particle and the matrix are kept equal to 0.25. In the related literature, a significant scatter was observed in the strength and the fracture energy of the matrix and the particle and they depend on various factors such as temperature, manufacturing technique and chemical composition [ARM97, KSKN04, SKÜW01, Pet95]. So, in the current study, a parametric approach is taken, whereby a range of relative fracture properties are considered and their effect on the crack path and the composite properties are quantified. The strength and fracture energy of the matrix are taken as $\sigma_{\mathrm{c}}^{\mathrm{m}}$ = 300 MPa and $G_{\mathrm{c}}^{\mathrm{m}}$ = 0.1 N/mm, whereas the strength and fracture energy of the particle and the interface ($\sigma_{\mathrm{c}}^{\mathrm{p}}$, $G_{\mathrm{c}}^{\mathrm{p}}$, $\sigma_{\mathrm{c}}^{\mathrm{i}}$, $G_{\mathrm{c}}^{\mathrm{i}}$) are varied with respect to the corresponding matrix properties for the analyses. The details on the fracture properties of the particle and the interface and their variations are specified in the relevant sections. All the analyses were conducted in Abaqus using implicit Newton-Raphson's iterative nonlinear solver.

As discussed in 3.1, the focus of the analyses is two-fold, i.e., evaluating the effect of the properties of the particle and the interface w.r.t the matrix on (a) the crack path and (b) the mechanical properties of the composite. Accordingly, Sec. 3.3 deals with a discussion of the simulation results in terms of the crack trajectories, followed by Sec. 3.4 which addresses the overall mechanical response of the specimen in terms of the composite properties.

3.3. EFFECT OF CONSTITUENT PROPERTIES ON CRACK TRAJECTORY

In this section, crack propagation through the particulate system is analyzed for three different representative cases in which the strength of the particle and the interface relative to that of the matrix were varied. The primary purpose of this section is to show the importance of the fracture properties in determining the crack trajectory through the microstructure, followed by a qualitative comparison of the simulation results with experimental observation of the crack path in the $MoSi_2$-YSZ composite microstructure.

CRACK PATH FOR RELATIVELY WEAK PARTICLES

A simulation is carried out with the properties mentioned in Sec. 3.2 for the particle and the matrix, except that the strength of the particle is reduced by 25 percent w.r.t the matrix, resulting in a strength mismatch ratio, $\sigma_c^p/\sigma_c^m = 0.75$ between the particle and the matrix. The fracture energy of the particle and the matrix are kept the same and equal to 0.1 N/mm. The particle is assumed to be perfectly bonded to the matrix, which is achieved by assigning very high fracture properties for the interface w.r.t the properties of the particle and the matrix. The simulated crack path through the microstructure is shown in Fig. 3.2 (indicated in white). It can be observed that the propagating crack finds the weaker path by fracturing all the particles that are in the neighborhood of the advancing crack tip. In this case, particles fracture despite the fact that the healing particles are stiffer than the matrix by a factor of 3. Thus, the mismatch in the fracture strength (making the particle weaker) has a stronger influential effect in deciding the crack path when compared with the effect of the mismatch in elastic properties. This result is relevant for a capsule-based self-healing mechanism since it indicates that healing activation can be achieved even if the particles are relatively stiffer than the matrix and crack-particle interaction is in principle deflective.

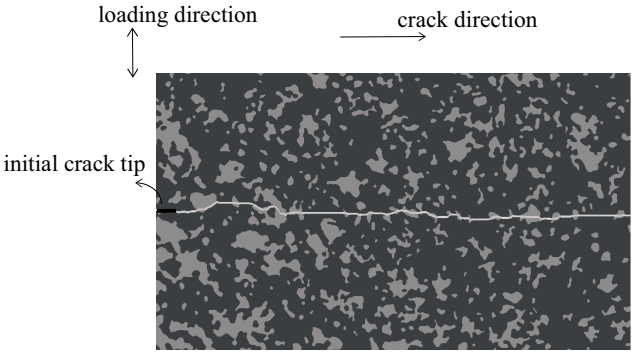

Figure 3.2: Simulated crack growth on a particle/matrix system with relatively weak particles given by the strength mismatch, $\sigma_c^p/\sigma_c^m = 0.75$ between the particle and the matrix (propagating crack path is from left to right). Perfect particle/matrix bonding is assumed in this simulation. A stiffer particle case is considered given by the elastic mismatch ratio, $E^p/E^m = 3$ between the particle and the matrix. The fracture energy of the particle, the matrix and the interface are kept equal to 0.1 N/mm.

CRACK PATH FOR RELATIVELY STRONG PARTICLES

The second case of interest is the situation when the strength of the particle is higher than that of the matrix. In this section, the simulation is performed with the material properties indicated in Sec. 3.2, except that the strength of the particle is increased by 25 percent as compared to the matrix strength, which corresponds to a particle strength mismatch ratio, $\sigma_c^p/\sigma_c^m = 1.25$. The fracture energy of the particle and the

matrix are kept the same and equal to 0.1 N/mm. Again, the bonding between the particle and the matrix is assumed to be perfect. The resulting crack path under the mode-I loading is reported in Fig. 3.3 (indicated in white). From the simulated crack path, it can be observed that the crack propagates preferentially through the matrix, thus, in general, avoiding the particles. However, on a few occasions, particle fracture did occur, when the particle is directly in front of the approaching crack. A similar observation has been made in [LZ13a]. Such instances of particle fracture despite its higher strength can also be attributed to the irregular shape and clustering of the particles (i.e., local stress conditions occur such that particle fracture is favored). Furthermore, in these particular cases, prevention of particle fracture would require an unrealistic deflection of the crack tip. As a general conclusion, a composite with particles of higher strength precludes fracturing of the particles. Such a scenario is unfavorable from a self-healing materials design viewpoint as this fracture mechanism would prevent triggering of the healing mechanism.

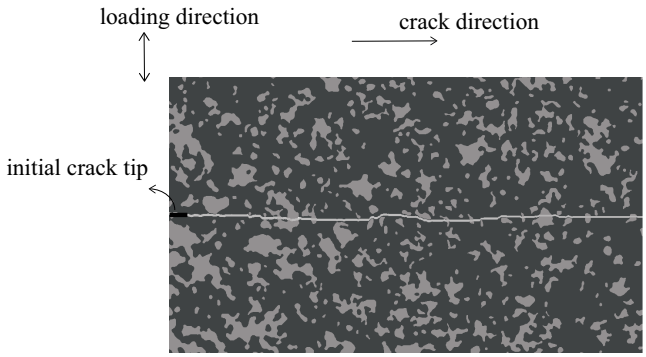

Figure 3.3: Simulated crack growth on a particle/matrix system with relatively strong particles given by the strength mismatch, $\sigma_c^p/\sigma_c^m = 1.25$ (propagating crack path is from left to right). Perfect particle/matrix bonding is assumed in this simulation. Fracture energies of all the phases are kept the same and equal to 0.1 N/mm.

CRACK PATH FOR A RELATIVELY WEAK INTERFACE

In the two cases presented above, the interface fracture strength was assigned a sufficiently large value to simulate perfect bonding between the particle and the matrix. However, in some systems, the strength of the interface may be relatively low. In order to study the effect of the interface properties, the fracture strength of the interface is reduced by 25 percent relative to the strength of the matrix and the particle, resulting in an interface strength mismatch ratio, $\sigma_c^i/\sigma_c^m = 0.75$. The strength and fracture energy of the particle and the matrix are assigned equal values and are given by $\sigma_c^p = \sigma_c^m = 300$ MPa and $G_c^p = G_c^m = 0.1$ N/mm respectively. The crack path obtained for this scenario is shown in Fig. 3.4. It can be observed that the

crack predominantly deflects its path towards the particle/matrix interfaces. Crack advancement occurs primarily through debonding along the interfaces between the particles and the matrix. Nevertheless, at few instances it is observed that particle fracture occurs when the particle is directly in front of the approaching crack or when it is relatively larger in size, making it difficult for the crack to circumvent the interface. From the perspective of successful triggering of healing mechanism, a weaker interface is in general not preferable as it does not necessarily lead to particle fracture. However, interface debonding could be considered as the second favourable fracture mechanism after particle fracture, as the probability of exposing the healing agent contained within the particle to the crack is likely to be high, potentially leading to healing activation.

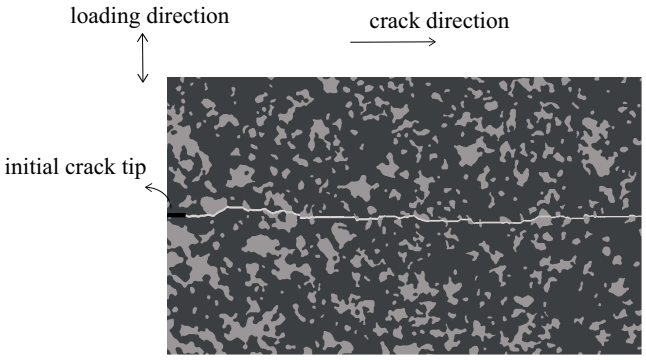

Figure 3.4: Simulated crack growth on a particle/matrix system with relatively weak interface given by the strength mismatch, $\sigma_c^i/\sigma_c^m = 0.75$ between the interface and the matrix (propagating crack path is from left to right). The fracture energy of all the phases are kept equal to 0.1 N/mm. The strength of the particle and the matrix are kept equal.

EXPERIMENTAL OBSERVATIONS ON CRACK PATH AND COMPARISON

This section deals with a qualitative comparison between the simulated crack paths reported above and the actual (experimental) crack path observed in the same microstructure. Fig.3.5 shows the experimental crack trajectory through the microstructure of the nominally Mode I loaded specimen. It can be observed that all the three mechanisms, namely matrix cracking, particle fracture and interface debonding, discussed in the above sections are observed. Upon further analysis of the experimental crack path, interface debonding is found to be the predominant failure mechanism with few instances of particle fracture. The experimental results suggest that the actual material parameters (especially the fracture properties) of the individual constituents correlate well with the values chosen for the simulation corresponding to the weak interface case. The crack path observed in the weaker interface case is qualitatively closest to the experimental crack path in terms of the occurrence of the debonding.

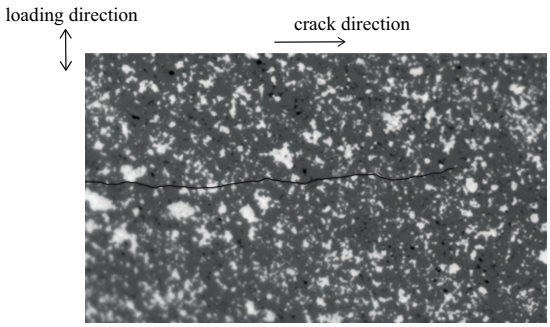

Figure 3.5: Experimental SEM observation of a crack in a microstructure containing $MoSi_2$ particles (white) embedded in Yttria Stabilised Zirconia (YSZ, dark). The crack, highlighted in black, runs from left to right.

Though one-to-one comparison was not feasible with the limited resources of the microstructures and the associated crack path data, a rough quantification of the fracture mechanisms is conducted by defining two quantities in percentage, p_1 and p_2, that quantify the number of instances of particle fracture and interface debonds in the resulting crack path respectively. The quantity p_1 is defined as n_1/N x 100, where n_1 is number of the fractured particles in the simulated crack path and N is the number of particles or interfaces encountered or traversed by a crack if the crack path were a perfect straight line originating from the initial crack tip. The quantity p_2 is defined as n_2/N x 100, where n_2 is the number of interface debonds in the simulated crack path.

In the experimental crack path, p_1 is found to be approximately 25 percent, while the instances of the particle/matrix interface debonding, p_2 is around 80 percent. In the simulation corresponding to the weak particle case, the percentage of particle fracture, p_1 is 160 percent with no instances of interface debonding. In the stronger particle case, the percentage of particle fracture, p_1 is around 45 percent again with no interface debonding. In the simulation result corresponding to a weaker interface, the percentage of interface debonding, p_2 is estimated at around 100 percent, while value p_1 corresponding to the instances of particle fracture is about 35 percent. Thus, the weaker interface case can be correlated well with the experimental observation with instances of both particle fracture and interface debonding with the latter being more predominant. More work on a quantitative comparison of the experimental crack patterns and the simulations are required for a definitive conclusion or inference. This, in turn, will require a statistical data of several microstructures of the composite and experimentally observed crack paths, which were not available during the period of this research.

3.4. EFFECT OF CONSTITUENT PROPERTIES ON GLOBAL MECHANICAL PROPERTIES

In the previous section, the influence of mismatch in fracture strength between the matrix and the particle and the effect of interface strength on the crack propagation path in the microstructure was studied. It is also worth mentioning that in the previous chapter, the influence of the mismatch parameters is analyzed in detail and its effect on cracking mechanisms (crack path) is discussed. However, the effect of the mismatch in constituent's properties on the global mechanical behaviour was not investigated. In other words, the influence on the interface and particle properties w.r.t the matrix on overall fracture properties of the composite were not studied. Hence, in this section, the objective is to examine and understand the same by utilizing the microstructure-based finite element analyses. The approach is to conduct a series of parametric studies and to derive the composite specimen strength and fracture energy from the resulting load-displacement responses. It is to be noted that the term specimen strength is used instead of effective strength, as the objective is not to derive homogenized composite properties, rather to reveal the role of elastic and fracture property mismatch on the global mechanical behaviour. However, the specimen properties obtained from the analysis would become the effective properties of the composite if appropriate measures are taken while applying the boundary conditions and if the specimen size is ensured to be sufficiently large to be considered as a Representative Volume Element (RVE). For convenience, the average specimen stress, the strain and the energy in the composite are denoted by σ_c^e, ϵ_c^e and G_c^e respectively. The results obtained from this study are presented in terms of normalised values of the above measures with respect to the corresponding values of the homogeneous matrix specimen.

This section is organized as follows. Firstly, the effect of mismatch in elastic properties between the particle and the matrix is studied and the resulting average stress-strain response is reported. The term 'average' represents the normalization of the load by the area over which the load is applied and the displacement by the corresponding length in the loading direction. This is followed by investigation of the effect of fracture properties of the particle on the global mechanical behavior and it is demonstrated how strong the particles can influence the global behavior of the composite. Another parameter of interest from a self-healing viewpoint is the number of instances of the particle fracture, which was reported for varying particle strength and fracture energy. Thirdly, the effect of fracture properties of the interface w.r.t the matrix is studied in detail and the results are reported. In this same section towards the end, the importance of mode-mixity in the interface-dominated fracture behaviour is demonstrated through a parametric study varying the mixed-mode interface strength.

The same microstructure used in the analysis in the previous section, Fig. 3.1 is utilised for the parametric study conducted in this section. The material properties of the particle, the matrix and the interface and their variations used in the analyses are specified in the relevant sections.

3.4.1. EFFECT OF ELASTIC PROPERTY MISMATCH ON GLOBAL MECHANICAL BEHAVIOR

To examine the effect of elastic property mismatch, fracture simulations on the microstructure with three different modulus mismatch ratios, $E^{\mathrm{p}}/E^{\mathrm{m}} = 1/3, 1$ and 3 are conducted. The Poisson's ratio of the matrix and the particle are kept the same and equal, with $\nu^{\mathrm{p}} = \nu^{\mathrm{m}} = 0.25$. In order to focus mainly on the effect of the mismatch in elastic modulus, the fracture strength of the matrix and the particle are assumed to be same and equal with $\sigma_{\mathrm{c}}^{\mathrm{p}} = \sigma_{\mathrm{c}}^{\mathrm{m}} = 300$ MPa. The fracture energy is also kept the same, given by $G_{\mathrm{c}}^{\mathrm{p}} = G_{\mathrm{c}}^{\mathrm{m}} = 0.1$ N/mm. Apart from the large variations in the fracture properties reported in the literature, the above values for the fracture properties for the constituents are chosen also for convenience, because it allows to conduct a parametric study whereby the relative fracture properties can be varied over a wide range. In other words, choosing a very low value for the fracture energy for the matrix as the reference value will prevent considering lower relative fracture energy of the particles and the interface due to computational issues associated with the cohesive zone size, and in turn the numerical convergence and intensive computational time. The interface between the particle and the matrix is assumed to be perfectly bonded with high values assigned to its fracture properties.

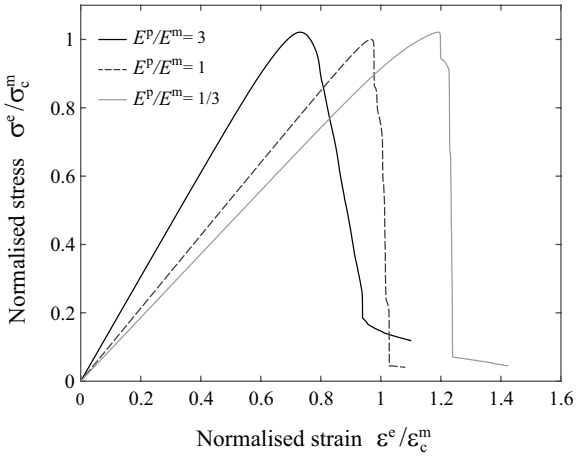

Figure 3.6: Effect of stiffness mismatch on the normalised stress-strain response of the composite. The fracture properties of the particle and the matrix are kept the same. Perfect interface bonding is considered.

The results of the simulations are reported in Fig. 3.6 in terms of the normalised stress-strain response. Three different features, which are relevant for the comparative study are the initial slope of the curve, the peak load and the post-peak response. They are respectively governed directly by elastic modulus, fracture strength and fracture energy and indirectly by their interactions. Apart from the trivial understanding on the effect of stiffness mismatch on the initial slope of the three curves, it can be observed that the specimen strength for all the three cases is approximately the same

irrespective of the stiffness of the particles. This suggests that for the considered system and the assumed fracture properties of the matrix (and the particle relative to the matrix), the stiffness of the particles has little influence on the specimen strength. Coming to the post-peak response of the specimens, it can be seen that the specimen with softer particles shows a brittle response when compared to the response of the specimens with particles of same and higher value of the stiffness. This can be attributed to the fact that reduction in stiffness of a phase reduces the corresponding fracture process zone size within that phase, contributing to a more brittle fracture behavior. Further, once the crack starts propagating, the presence of softer particles tends to accelerate the crack propagation rate, resulting in a brittle fracture. An interesting aspect to notice is that the total energy dissipated due to fracture is higher in the specimen with the softer particles. This observation may appear contradictory as it is established in the literature that stiffer particles enhance the fracture toughness by shielding effects. In this context, it is important to note that the fracture properties (strength and toughness) of the particle and the matrix and their mismatch is often ignored in the literature. In the current results, though the softer particle attracts the crack towards it (producing an anti-shielding effect), it is as strong as the surrounding matrix phase, which in combination with its lower modulus leads to increased strain to fracture and hence the energy dissipation. In other words, the strain corresponding to the peak stress is higher in softer particle case due to its lower stiffness and because the particle is as strong and tough as the matrix material.

In the next two sections, the effect of fracture properties of the particle and the interface on composite specimen strength is investigated. A stiffer particle case is considered, by fixing the modulus mismatch ratio as $E^{\mathrm{p}}/E^{\mathrm{m}} = 3$, representative of the particulate composite considered for the self-healing TBC system.

3.4.2. EFFECT OF PARTICLE FRACTURE PROPERTIES ON MECHANICAL BEHAVIOUR

The influence of the fracture properties of the particles on the specimen strength is analysed in this section. In the context of self-healing materials, two main aspects are important, (i) the probability of opening of the healing particles, favoring crack healing activation and (ii) the effect of particle properties on composite strength, which explains the mechanical integrity of the self-healing material. In essence, achieving both of these factors, i.e., triggering of the healing mechanism and superior structural integrity are often contradictory as promoting particle fracture for healing intuitively is likely to degrade the composite strength. Hence, for an optimal design of the self-healing material, a balance between these two contradicting requirements has to be achieved. With this motivation, the analyses conducted in this section reports the number of fractured healing particles and the resulting strength of the composite material with respect to variations in the particle fracture properties. The strength of the composite in the results presented in the rest of the chapter is normalized w.r.t the matrix strength.

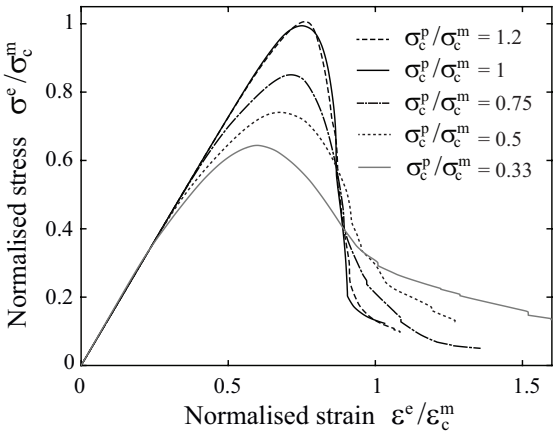

Figure 3.7: Effect of particle strength on the normalised stress-strain response of the composite specimen. The fracture energy of the particle and the matrix are kept the same. Perfect interface bonding is considered.

To analyse the effect of particle fracture properties on composite strength, several values of particle strength ratios are considered, given by σ_c^p/σ_c^m = 0.05, 0.25, 0.33, 0.5, 0.75, 1 and 1.25. To explore the effect of particle fracture energy, for each of the above strength ratios, three different fracture energy ratios of the particles w.r.t the matrix fracture energy are considered and are given by G_c^p/G_c^m=1/5, 1 and 5. The results of the simulations are summarized in Fig. 3.7 and Fig. 3.8. Fig. 3.7 shows the average stress-strain response for some selected strength ratios which provides the insights into the composite response. Some important observations can be made from the plot. Firstly, the strength of the composite specimen decreases with decrease in the particle strength. The strain corresponding to the peak stress (or strength) in the stress-strain curve decreases with decrease in the particle strength. It is also to be noted that the slope of the curve prior to the initiation of crack propagation is not altered by the reduction in particle strength. This can be explained by the fact that the slope corresponds to the elastic modulus of the composite, which is not governed by the fracture properties of the constituents prior to crack propagation.

To summarise the results of all the simulations for varying particle strength and fracture energy, Fig. 3.8 shows the variation of the resulting strength of the composite specimen with respect to the particle fracture properties (strength and energy). The number of instances of particle fracture is shown in Fig. 3.8b. As discussed before, the results clearly show a strong influence of the particle fracture properties on the mechanical response of the composite specimen. From the plot shown in Fig. 3.8, it can be observed that, decreasing the strength of the particle in relation to the matrix strength severely decreases the composite strength. For instance, the strength of the composite is decreased by 25 percent with respect to the reference homogeneous matrix specimen strength, when the particle strength is reduced by 50 percent. On the other hand, increasing the particle strength above the matrix strength does not

improve the strength of the composite as observed from the results. On the effect of fracture energy, a similar effect is observed, i.e., decreasing the fracture energy of the particle reduces the composite strength as shown in Fig. 3.8a. However, it has to be noticed that the effect of fracture energy ratio is pronounced only in the intermediate ranges of the strength ratios. In other words, when the particle strength is higher than that of the matrix or very low, then the composite strength is insensitive to the fracture energy of the particle as observed from the Fig.3.8a.

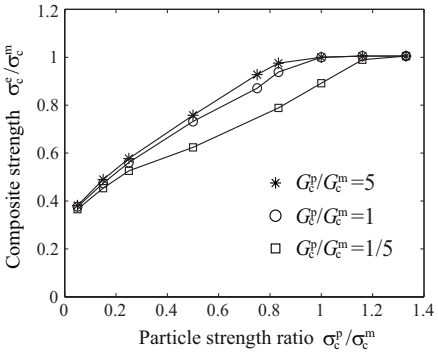

(a) Variation of composite strength vs particle fracture properties

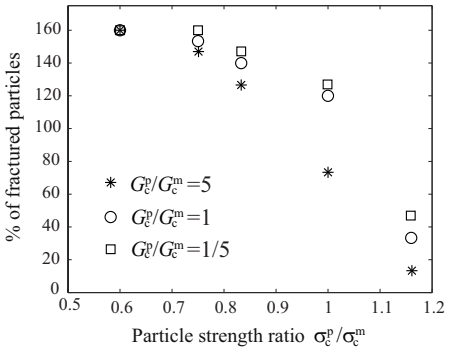

(b) Normalised percentage of fractured particles vs particle fracture properties

Figure 3.8: Effect of particle fracture properties on the composite strength and the percentage of fractured particles. The particle strength is varied over a range, whereas for the particle fracture energy, three different ratios are considered as shown in the plots.

In terms of the crack paths, representative crack paths corresponding to particles of lower and higher strengths w.r.t the matrix strength were already shown and discussed in Sec. 3.3. Hence, the crack paths are not discussed in detail here, rather another parameter of interest derived from the crack path, namely the number of fractured particles in the resulting crack path, defined as the quantity p_1 earlier in Sec.3.3 is reported and discussed. The number of instances of particle fracture, given by p_1 is shown as the function of the fracture properties of the particles in Fig. 3.8b. For the purpose of clarity, p_1 is the percentage of the number of fractured particles normalised with respect to the number of particles that would fracture if the crack were to be a straight line originating from the initial crack tip and traversing across the microstructure. As a general observation, decreasing the strength of the particle favors particle fracture as observed from Fig.3.8b, a requirement for healing activation. However, the maximum number of fractured particles saturates when the particle strength is reduced beyond the strength ratio, $\sigma_c^p/\sigma_c^m = 0.6$ and is around 160 percent. This would mean that the number of fractured particles is 60 percent more than the instances of fractured particles in an ideally straight crack originating from the initial crack tip. On the lower side, the number of fractured particles reduces to just 10 percent if the particle strength ratio is increased to a value beyond $\sigma_c^p/\sigma_c^m = 1$. The

fracture mechanism is very sensitive to the mismatch in the particle strength especially when the particle strength ratio is perturbed around the value of one.

When it comes to the fracture energy mismatch, the effect is less pronounced as compared to the strength ratio, a similar observation made in chapter 2. Increasing the fracture energy does not reduce the number of particle fracture significantly, although reducing the fracture energy of the particle have a more pronounced effect as observed from Fig. 3.8b. The two plots showing the variation of the composite strength and the number of fractured particles, w.r.t particle fracture properties gives an insight on how to achieve the balance between the two contradictory requirements for self-healing material design. For instance, the objective of particle fracture (or healing activation) can be achieved with healing particles that are only slightly weaker than the matrix. For example, for the strength ratio, $\sigma_c^p/\sigma_c^m = 0.833$, a very high percentage of particle fracture can be realised with just 5 percent reduction in composite strength, refer Fig. 3.8b. Thus, if the healing particles can be engineered such that their strength is slightly lower than the matrix strength, a successful self-healing system can be achieved (in terms of healing activation) without significant compromise in the fracture properties of the composite.

3.4.3. EFFECT OF INTERFACE FRACTURE PROPERTIES ON MECHANICAL BEHAVIOUR

Another important feature that governs the global mechanical behaviour of the particulate composite is the interface between the particle and the matrix. In the context of self-healing materials, the requirement on the interface properties is not straightforward. As discussed in chapter 2, the ideal combination for robust self-healing system would be a stronger particle perfectly bonded to the surrounding matrix material. In that case, high interface strength is advantageous for efficient load transfer, whereby both the particles and the matrix are load-bearing constituents in the composite. However, if the particle is stronger than the matrix, particle fracture is less likely to occur, which, in turn, does not activate the healing mechanism when required. In such scenario, a relatively weaker interface could help in facilitating debonding between the particle and the matrix and expose the healing particle to the crack. When the particle is sufficiently exposed to the crack, the healing process can get activated. In other words, the healing agent from the particle, which is now exposed, can diffuse into the crack and fill the crack through oxidation, refer to the healing mechanism in self-healing TBC system in chapter 2.

EFFECT OF INTERFACE FRACTURE STRENGTH

To investigate the role of interface fracture properties, a series of simulations are conducted for varying interface fracture properties, while fixing the stiffness mismatch ratio between the particle and the matrix, given by $E^p/E^m = 3$. The strength and fracture energy of the particle and the matrix are kept the same and are given by $\sigma_c^p = \sigma_c^m = 300$ MPa and $G_c^p = G_c^m = 0.1$ N/mm respectively.

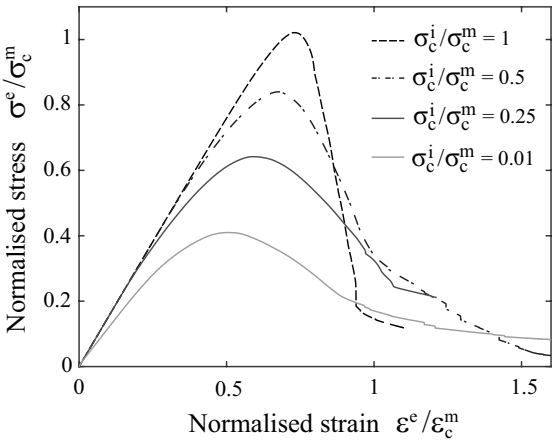

Figure 3.9: Effect of interface strength on the normalised stress-strain response of the composite specimen. The stiffness mismatch ratio is $E^p/E^m = 3$ that corresponds to a stiffer particle. Fracture strength of the matrix and the particle are kept the same. The interface fracture energy is fixed and equal to that of the fracture energy of the particle and the matrix, $G_c^i = G_c^p = G_c^m = 0.1$ N/mm.

3

For the sake of understanding and discussion, responses of the specimen with four different values for the interface fracture strength given by, $\sigma_c^i/\sigma_c^m = 0.01, 0.25, 0.5$ and 1 are reported in Fig. 3.9. From the figure, it can be seen that an interface which is perfectly bonded (or at least having equal fracture properties as that of the matrix and the particle) results in a higher overall strength of the specimen as compared to the other responses corresponding to lower interface strengths. This is an expected outcome as stronger interface leads to better load transfer between the matrix and the particle resulting in higher strength. However, it is worth noting that higher interface strength or perfect bonding leads to a relatively brittle response in the considered setup. As the interface becomes weaker, the fracture mechanism, namely, the interface debonding kicks in and introduces additional energy dissipating mechanism. This, in turn, leads to enhanced energy dissipation and 'ductile' behavior of the composite, albeit with reduced strength. Such a scenario is often useful in composite materials with brittle-brittle phases whereby engineering the interface aids in introducing ductility in the composite material [YJ91]. The term 'ductility' is used in a general sense implying a non-abrupt fracture process and does not mean any plastic deformation.

The results of several simulations are conveniently summarized in Fig. 3.10 showing the variation of composite specimen strength as a function of interface properties. In addition to varying interface strength, three different interface fracture energy ratios are considered in the study, given by $G_c^i/G_c^m = 1/5$, 1 and 5 and the results are shown in the Fig. 3.10. A clear trend is observed revealing the improvement of composite strength with increase in the interface strength. The strength of the composite specimen saturates when the interface fracture strength is increased beyond the

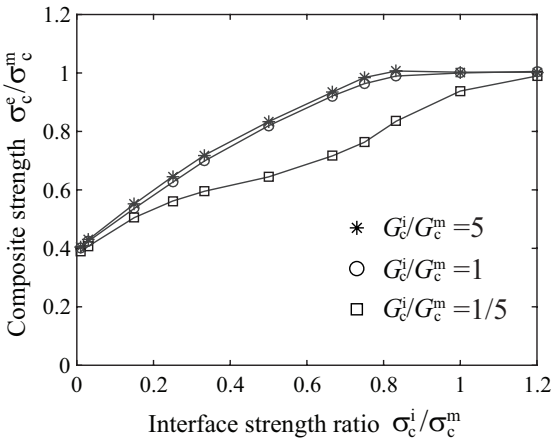

Figure 3.10: Effect of interface strength and fracture energy on strength of the composite specimen. The stiffness mismatch ratio is $E^p/E^m = 3$ that corresponds to a stiffer particle. Fracture properties of the matrix and the particle are kept the same.

strength of the particle and the matrix, which is an expected result as seen from the plateau region of the curve. On the other end, when the interface strength ratio is reduced to a value equal to 0.01 (interface strength is 100 times lower than that of the matrix and particle), the value of the composite specimen strength reaches a lower limit approximately equal to 40 percent of the matrix strength. This can be viewed as the strength of the composite with particles replaced by loose particles as the interface hardly plays any role in load transfer between the particle and the matrix. Such an explanation is applicable and valid only for tensile strength, but for the same composite under compression, completely debonded particles would still contribute significantly to the load carrying capability through contact and frictional forces. On the effect of interface fracture energy, increasing the fracture energy of the interface did not influence the strength of the composite, but decreasing the interface fracture energy reduces the composite strength as observed from the figure, a similar trend as seen in the effect of particle fracture energy in the previous section.

To explore the effect of interface fracture energy in detail, simulations are conducted for a wide range of interface fracture energy while keeping the interface strength to a fixed value and the results are presented in the following subsection.

EFFECT OF INTERFACE FRACTURE ENERGY

In the previous section on examining the effect of interface strength, only three fracture energies were considered. To evaluate the effect of interface fracture energy in more detail, in this subsection, the interface is assigned a range of values for the ratio of interface fracture energy to matrix fracture energy, G_c^i/G_c^m. Meanwhile, the strength of the interface is kept constant and lower than the matrix and particle strength and is given by the ratio, $\sigma_c^i/\sigma_c^m = 0.667$. A lower value for the interface strength is chosen so

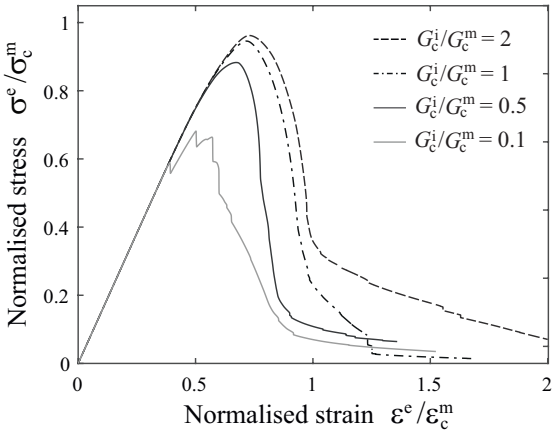

Figure 3.11: Effect of interface fracture energy on the composite stress-strain response. The stiffness mismatch ratio is $E^p/E^m = 3$ that corresponds to a stiffer particle. Fracture properties of the matrix and the particle are kept the same. The interface strength is fixed and given by $\sigma_c^i/\sigma_c^m = 0.667$.

that interface cracks can be initiated and following which, the role of interface fracture energy on the mechanical behavior can be maximized. In other words, if the interface strength is assigned a higher value than that of the particle or the matrix, initiation of interface debonding or cracking will not occur and any large value of interface energy will not affect the fracture behavior.

The simulations are carried out for various fracture energy ratios given by, $G_c^i/G_c^m = 0.1, 0.5, 1, 1.5, 2$ and 3 and the results are summarized in Fig. 3.11. It can be observed from the figure that increasing the fracture energy of the interface, increases the composite strength as well as the energy dissipated during the fracture process (the latter is related to the fracture energy of the composite).

For ease of understanding and better clarity, the effect of interface fracture energy on the composite strength and the dissipated energy is extracted and summarised in Fig. 3.12. With regards to composite strength as shown in Fig. 3.12a, upon increase in the fracture energy ratio, the strength increases gradually until the interface fracture energy ratio is increased to a value of 1. With further increase in the interface fracture energy, the composite strength is only slightly increased, making the composite strength independent of the fracture energy ratio once it is increased beyond the value of 1. The highest composite strength that can be achieved for the considered configuration is equal to 0.97 (normalised with respect to strength of the homogeneous matrix specimen). The lowest composite strength that is attained in the analyses corresponds to the interface fracture energy ratio = 0.1 and is equal to 60 percent of the strength of the homogeneous matrix specimen. On the other hand, unlike the composite strength, the dissipated energy in the composite increases monotonically with increase in interface fracture energy ratio even after the interface fracture energy ratio is increased beyond 1 as seen in Fig. 3.12b. For instance, the dissipated energy in

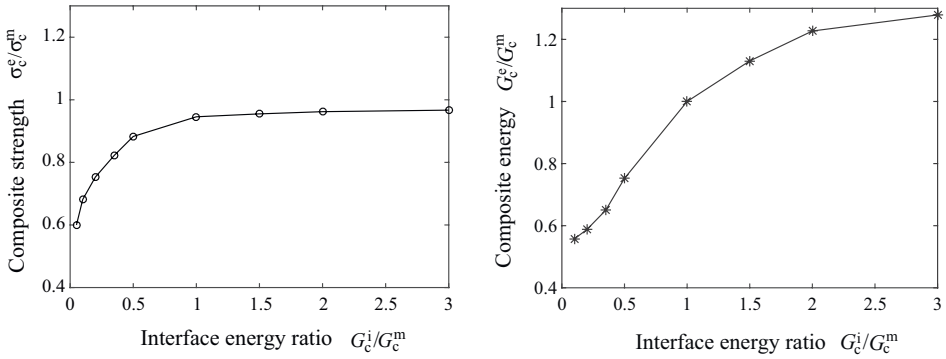

(a) Effect on composite strength

(b) Effect on dissipated energy

Figure 3.12: Influence of interface fracture energy on the composite strength and the dissipated energy in the cracked composite microstructure. Fracture properties of the matrix and the particle are kept the same. The interface strength is fixed and given by $\sigma_c^i/\sigma_c^m = 0.667$.

the composite increases by 28 percent when the interface fracture energy ratio is equal to 3. However, as can be observed from Fig. 3.11, the enhancement in the dissipated energy kicks in only after the stress drops to 40 percent of the peak stress (strength). On the lower side, i.e., for the lowest interface fracture energy ratio considered, the dissipated energy in the composite decreased to a normalised value of 0.55.

Thus, the fracture energy of the interface plays a crucial role in determining the effective composite properties, both in terms of strength and toughness. In the context of self-healing materials, it is important to consider the above aspect as the design of the healing particle-matrix interface can be detrimental to the overall behaviour of the resulting self-healing composite material.

EFFECT OF MODE-MIXITY ON COMPOSITE FRACTURE STRENGTH

While analysing fracture in composite materials (particulate or fiber-reinforced), mixed-mode fracture is a common phenomenon occurring in the failure of such materials. Mixed-mode fracture arises from two main sources, one being the applied boundary or loading conditions in such a way that fracture evolves under globally applied mixed-mode loads. The second source is the inherent heterogeneity of the material microstructure that leads to local mixed-mode fracture conditions in the vicinity of the interfaces between the particles (or fibers) and matrix. This is often the case in composite materials, whereby even when the structure or the composite material is subjected to global Mode-I loading conditions, local stress fields in the crack vicinity are influenced by the presence of particles or fibers (and their interfaces), resulting in crack evolution under mixed-mode conditions. Quite often, the fracture properties of a material phase, i.e., the strength and the toughness, are different for different modes of fracture (normal and shear), which is due to the difference in the associated fracture mechanisms in each mode. More importantly, the fracture

properties of an interface between two material phases are found to be significantly different in opening (normal) and shearing modes of fracture. Thus, it becomes a natural problem of significance to address the effect of varying interface fracture properties in normal and shear modes on the mechanical behavior of the composite.

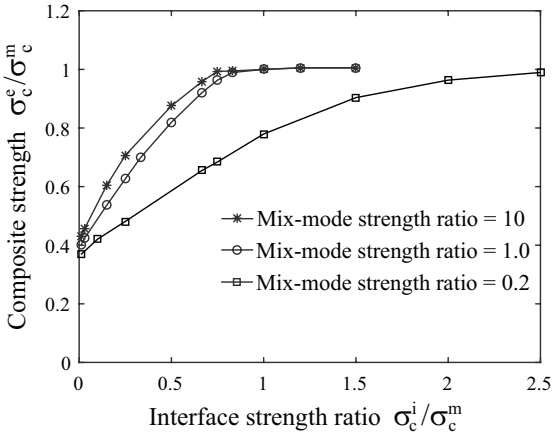

Figure 3.13: Effect of interface mix-mode strength ratio on strength of the composite specimen. Fracture properties of the matrix and the particle are kept the same. The interface fracture energies in both normal and shear modes are fixed and equal to that of the fracture energy of the particle and the matrix, $G_c^i = G_c^p = G_c^m = 0.1$ N/mm.

In this subsection, fracture analyses are conducted considering different values of the interface strength in Mode-I and Mode-II (normal and shear strengths) and the effects are quantified in terms of the resulting composite strength. To this end, three sets of analysis are conducted to address the above problem. Firstly, the interface fracture strength (and the energy) are kept the same in both opening and shearing modes. In the second set of analyses, the interface strength in Mode-II is taken equal to 10 times higher than the strength in Mode-I. By doing this, we ensure, the interface is much stronger in Mode-II, thus majorly providing very high resistance to shearing mode fracture. In the third set, the interface shear strength is reduced by a factor of 5 as compared to its normal strength, enabling us to model an interface which would easily yield to local Mode-II deformation field. In all the three sets, the interface normal strength is varied over a wide range and the shear strength varies accordingly in the three different sets of analyses described above.

The results of the simulations are obtained in terms of the effective composite specimen response. The results are conveniently summarized in Fig. 3.13 in terms of the normalised composite strength vs interface strength for three different sets of simulations. From the plot, it can be generally observed that increasing ratio of interface shear strength to its normal strength increases the resulting composite strength. For the mixed-mode strength ratio = 10, the composite strength is increased by approximately 8 percent w.r.t the baseline case (mixed-mode strength ratio = 1) for

most of the considered interface (normal) strength to matrix strength ratios. However, once the interface (normal) strength is increased beyond the matrix strength, the considered interface mixed-mode strength ratio does not influence the composite strength. This is because of the fact that the interface debonding is automatically arrested when the interface strength is higher than the matrix (and particle) strength and any increased shear to normal strength ratio of the interface will not affect the strength of the composite. On the other hand, for the mixed-mode strength ratio of the interface equal to 0.2, the influence is very strong as observed from the Fig. 3.13. The resulting composite strength is drastically reduced for most of the considered cases of the interface strength ratio. This shows that though the prescribed boundary condition is globally Mode-I loading, local mixed-mode effects can play a significant role, especially if the strength of the interface is different in normal and shear modes. For instance, in the present study, the composite strength under Mode-I loading is reduced by 30 percent for some of the interface (normal) strength ratios considered. Further, in the mixed-mode case with a ratio of 0.2, the reduced shear strength of interface affects the composite strength even after the interface normal strength ratio is increased beyond 1. For example, it is only when the interface strength ratio is increased to 2.5, the saturation of the resulting composite strength occurs as from the figure. As an overall remark, the mixed-mode properties can become important for composite behaviour especially if the fracture properties are significantly different in normal and shear modes despite the loading conditions being pure Mode-I or II.

3.5. SUMMARY AND CONCLUSIONS

In this chapter, micromechanical fracture simulations were conducted to study the effect of constituent's properties on the crack trajectory and the overall fracture properties of the composite specimen. The results obtained from the fracture analysis taking a real $MoSi_2$ particle filled TBC matrix microstructure as the starting configuration agree qualitatively well with an ideal system. As observed in the single-particle simulations reported in the earlier chapter, mismatch in fracture properties of the particle, the matrix and the interface has a significant influence on the resulting crack path in the microstructure-based simulations. Relative fracture strength values of the particle and the interface were found to be the dominating factors in controlling the crack path. One of the conclusions is that a self-healing TBC coating requires an encapsulated healing particle with a strong particle/matrix interface and a tensile strength lower than that of the matrix, which is in line with the observation made in chapter 2. Nonetheless, it is to be expected that in practice the combination of a high temperature and a long exposure time, will ensure that, interface debonding can also expose the healing agent to the crack which, in turn, expands the design space for achieving optimal configurations of the material system for activating the self-healing mechanism. When it comes to the effective mechanical properties of the resulting self-healing composite, the reported results reveal the effect of the particle and the interface fracture properties on the composite strength and dissipated energy. On one hand, the properties of the healing particle and the interface can be tailored to

achieve the healing activation, however, on the other hand, such an approach affects the overall fracture properties of the resulting composite, which becomes detrimental to the material system. Care must be taken in order to achieve a trade-off between the resulting initial composite properties and the healing activation as it is natural that both the requirements could be contradicting in many practical self-healing materials.

From the extensive fracture analyses on the composite microstructure, the following conclusions were arrived at:

- The guidelines established in chapter 1 holds very well for the realistic composite microstructure. In addition to the showcased effect of the fracture properties of the particles and the interface on the crack path, factors such as particle geometry and distribution can also influence the fracture mechanism.
- The mechanical properties of the composite (in particular, the strength) are significantly influenced by the fracture properties of the particle and the interface. The effects of the strength of the particle and the interface are more pronounced than that of the fracture energies in determining the composite properties. In case of interface-dominated fracture, mixed-mode fracture properties of the interface play a crucial role on the resulting composite strength.
- The number of fractured particles in the resulting crack path is very sensitive to the fracture strength of the particle. For instance, particles that are slightly weaker than the matrix can trigger particle fracture (hence the healing mechanism), importantly without compromising the composite properties noticeably.

The results and conclusions from the microstructure-based crack propagation analyses can be used to get insights on pathways to achieve optimal self-healing material system, i.e., a design with the capability to trigger healing process but one which does not significantly lower the structural integrity of the original unfilled matrix material.

4

COHESIVE ZONE-BASED CRACK HEALING MODEL

A cohesive zone-based constitutive model, originally developed to model fracture, is extended to include a healing variable to simulate crack healing processes and thus recovery of mechanical properties. The proposed cohesive relation is a composite-type material model that accounts for the properties of both the original and the healing material, which are typically different. The constitutive model is designed to capture multiple healing events, which is relevant for self-healing materials that are capable of generating repeated healing. The model can be implemented in a finite element framework through the use of cohesive elements or the extended finite element method (XFEM). The resulting numerical framework is capable of modelling both extrinsic and intrinsic self-healing materials. Salient features of the model are demonstrated through various homogeneous deformations and healing processes followed by applications of the model to a self-healing material system based on embedded healing particles under non-homogeneous deformations. It is shown that the model is suitable for analyzing and optimizing existing self-healing materials or for designing new self-healing materials with improved lifetime characteristics based on multiple healing events.

4.1. INTRODUCTION

Though extensive research has been conducted in realizing self-healing material systems experimentally, efforts to develop computational models that could simulate fracture and healing have been scarce. Simulation-based design guidelines can be used to optimize self-healing systems. Consequently, the goal of the present work is to develop a computational framework to model the effect of crack healing behavior on the mechanical performance of the material or the structure under consideration.

The modelling and computational framework is kept sufficiently general such that it is capable of analyzing both extrinsic and intrinsic self-healing materials.

In the context of a capsule (or fiber)-based extrinsic self-healing system, there are two critical aspects that need to be addressed in order to achieve a robust self-healing system. Firstly, a crack initiated in the host (or matrix) material should be attracted towards the healing particle (or fiber) and further should break the particle for healing to occur. Crack-particle interaction, which is a crucial aspect to successfully trigger the healing mechanism, has been analyzed parametrically in [PTvdZ15, PTZX15] to generate design guidelines for the selection of the healing particles in terms of their mechanical properties, refer 2. Other studies in the literature have utilized analytical and numerical techniques to investigate the interaction between the crack and the healing particles or capsules [ZJV11, GGP17, ŠFA+16]. The second critical aspect in a self-healing system, relevant for both extrinsic and intrinsic mechanisms, is centered on how the material recovers its mechanical properties once the healing mechanism is activated in or near the fracture surfaces. In particular, the recovery of load-carrying capability as a function of healing parameters, crack length and capsule properties is a subject of importance but has not received adequate attention in the literature yet. Consequently, one main focus of the present chapter is to simulate the recovery of mechanical properties of the self-healing system.

Research efforts have been made in the literature to model the mechanical behavior of materials taking both fracture and healing into account. Most of the existing models adopt a continuum damage mechanics-based approach whereby cracking and healing are interpreted as a degradation or recovery of material stiffness and strength [BGL05, VSLK12, VSL11, MS13, DAL12, XSKZ14, OON16]. The common feature of these models is that the internal variables describing the continuum degradation and healing of the material refer to the effective behavior of (unresolved) cracking and healing events. Correspondingly, details at the level of individual cracks are not explicitly taken into account. However, a direct description at the level of individual cracks and healing particles is desirable in view of designing or fine-tuning a self-healing material.

Cohesive zone-based approaches have also been proposed for modelling crack healing. Unlike continuum damage models, the advantage of the above cohesive zone approaches is that the material damage is treated in a discrete manner as cohesive cracks, which allows for explicit modelling of crack evolution and its healing. In [MG06], crack healing is simulated through an artificial crack closure technique by introducing a wedge into the crack. The methodology is implemented in a finite element framework using cohesive elements for simulating fracture and a contact law that enforces the conditions for crack healing or retardation. In [SR06] a Mode I exponential cohesive zone model is proposed to simulate crack healing by introducing a jump in crack opening displacement. After model verification, they applied the framework to simulate delamination crack healing in a slender beam specimen to show the capability of the model. Some limitations of the model are with regard to the multiple healing events and their one-dimensionality. In [UKP09], a

cohesive zone model for fatigue crack growth is developed, which also considers crack retardation during unloading regimes. In [AA15] a thermodynamics-based cohesive zone methodology is used to model crack healing behavior by extending previous work on continuum damage-healing mechanics [DAL12]. The model takes into account the effect of various parameters such as temperature, resting time and crack closure on the healing behavior. However, the fracture properties of the healed zone, upon complete healing, assume the values of the original material, which is often not the case even for intrinsic self-healing materials. Furthermore, the capability of simulating multiple healing events is not demonstrated in many of the above-mentioned studies, which is of direct relevance for intrinsic self-healing materials or extrinsic systems with a continuous supply of healing agent. Other approaches explored in the literature to model crack healing are based on the theory of porous media [BSS15] or the discrete element method [LS08, HL08].

To overcome the limitations in the existing models in the literature, a generalized cohesive-zone based crack healing model is developed here, which can be applied to both extrinsic and intrinsic self-healing materials. The model is capable of simulating property recovery after multiple healing events and is also able to handle different fracture properties for the healing material as compared to that of the original material. An additional feature of the model is that the properties of the healing material may be specified separately for different healing instances. This is particularly important as the recovery of the fracture properties in the healed zone is not always complete, resulting in varying fracture properties for each healing instance that depend, among others, on healing time, diffusion-reaction characteristics and temperature. It is noted that the model developed here does not explicitly aim to capture the actual healing kinetics, but to simulate the recovery of the overall load bearing capacity as a function of crack filling and fracture properties of the filling material. Nonetheless, detailed healing kinetics of a material can be coupled to the present model through the fracture properties and crack filling behavior to simulate specific materials. It is worth mentioning that the model does not explicitly take into account of the healed zone or the product, but rather considers it through its fracture properties. Hence, the fracture properties of the healing material here refer to that of the healed zone which represents the combined effect of the healing material and the bonding between the healing material and the surrounding matrix.

The chapter is organized as follows: the proposed crack healing model based on a cohesive zone approach and its finite element implementation are described in detail in Sec. 4.2. Verification of the model is done through basic tests in Sec. 4.3, from which salient features of the model are demonstrated. Sec. 4.4 is devoted to the application of the model to a particle-based extrinsic self-healing system under mechanical loading. Parametric studies are conducted to showcase the applicability of the model considering some realistic scenarios and the results are reported. Concluding remarks and further work are highlighted in Sec. 4.5.

4.2. MODELLING OF FRACTURE AND HEALING

The cohesive zone-based fracture mechanics model presented in chapter 2 is extended to model both the fracture and the healing in a unified constitutive relation. In the present fracture-healing framework, the following modelling considerations are made. Firstly, the crack healing model does not include healing kinetics explicitly, rather the focus is to develop a methodology to simulate cracking and the recovery of mechanical integrity upon healing. Consequently, whenever the healing process is activated at a location within the cohesive crack, the resting period is assumed to be sufficiently long such that complete healing occurs. This assumption is not necessary per se, but enforced in order to have a specific focus on recovery of mechanical properties using a modified cohesive constitutive relation. Nonetheless, depending upon the type of healing process involved in a specific healing material system, appropriate healing kinetics can be treated separately and coupled with the present framework. This, in turn, can govern the effect of parameters such as resting time and temperature on the degree of healing, which can then be fed as an input to the present framework through appropriately defined fracture properties of the healed material phases.

4.2.1. CRACK HEALING MODEL

The single healing case is discussed first, which is then followed by a generalized model capable of multiple healing events.

SINGLE HEALING EVENT

The proposed crack healing model is a composite-based constitutive model for simulating the recovery of fracture properties upon activation of crack healing. The traction components of the composite response, $\tilde{t}_\mathrm{n}$ and $\tilde{t}_\mathrm{s}$, are expressed as a weighted sum of the traction contributions from the original material, $t_\mathrm{n}^{(0)}$ and $t_\mathrm{s}^{(0)}$, and the healing material $t_\mathrm{n}^{(1)}$ and $t_\mathrm{s}^{(1)}$, as follows:

$$\tilde{t}_\mathrm{n} = w^{(0)}\, t_\mathrm{n}^{(0)} + w^{(1)}\, t_\mathrm{n}^{(1)} \qquad \tilde{t}_\mathrm{s} = w^{(0)}\, t_\mathrm{s}^{(0)} + w^{(1)}\, t_\mathrm{s}^{(1)} \tag{4.1}$$

where the superscripts (0) and (1) represent the original and healing materials, respectively. The weighting factors $w^{(0)}$ and $w^{(1)}$ introduced in (4.1), which can take values between 0 and 1, are the primary parameters in the model and can be interpreted as the surface-based volume fractions of the original and healing material respectively at the instance of healing activation. The meaning of "volume fraction" in this context refers to the fraction of the crack area occupied by a material per unit crack opening displacement. In a two-dimensional setting, the crack area fraction refers to the crack length fraction per unit depth. As indicated in (4.1), it is assumed that a partially damaged area that has been healed contains contributions from both the original material and the healing material. Correspondingly, the weighting factors $w^{(0)}$ and $w^{(1)}$ are related to fractions of a partially damaged surface where the original material is still capable of transmitting a force (in the sense of a cohesive relation) while the healing material has occupied the complementary region. Observe that this assumption implies that the model is essentially based on

an "equal strain" distribution among the phases (Voigt model), in this case with the crack opening playing the role of a strain-like variable. Consequently, the tractions in each phase may be overpredicted compared to a model based on an "equal stress" assumption (Reuss model), however the current Voigt-like model preserves kinematic compatibility whereas a Reuss-like model does not.

In order to develop the constitutive model, define an energy-based damage parameter $D^{(0)}$ as follows:

$$D^{(0)}(t) := \frac{G_{\mathrm{d}}^{(0)}(t)}{G_{\mathrm{c}}^{(0)}} \tag{4.2}$$

which represents the ratio between the energy dissipated $G_{\mathrm{d}}^{(0)}(t)$ during decohesion of the original material up to time t and the fracture energy $G_{\mathrm{c}}^{(0)}$ (work required for complete decohesion of the original material). In a bilinear cohesive relation, this parameter may be approximated as

$$D^{(0)}(t) \approx \left(\frac{\kappa^{(0)}(t)}{\Delta_{\mathrm{f}}^{(0)}} \right)^2$$

where the initial, undamaged "elastic" response has been neglected (namely it is assumed in (2.6) that $\Delta_{\mathrm{f}}^{(0)} \gg \Delta_{\mathrm{i}}^{(0)}$).

Prior to healing, the cohesive response is characterized by the cohesive relation of the original material, i.e., with $w^{(1)} = 0$ in (4.1). If a single healing event occurs at a time $t = t^*$, the proposed constitutive model assumes that the factor $w^{(1)}$ is given by the value of the energy-based damage parameter at the instance of healing activation, $D^{(0)^*}$, i.e.,

$$w^{(1)} = D^{(0)^*} := \frac{G_{\mathrm{d}}^{(0)^*}}{G_{\mathrm{c}}^{(0)}} \,. \tag{4.3}$$

Correspondingly, a value $w^{(1)} = 0$ upon healing activation represents zero equivalent damaged area fraction of the original material at a given material point (i.e., the original material is fully intact) while $w^{(1)} = 1$ represents a fully-damaged original material at a given material point (i.e., the healing material would occupy the fully damaged material point upon healing). The interpretation of (4.3) is that the volume fraction $w^{(1)}$ available for the healing material in order to fill and heal can be determined from the value of the energy-based damage parameter of the original material, defined in (4.2) at the instance of the healing activation. Upon healing of the available volume fraction $w^{(1)}$, the volume fraction of the original material, $w^{(0)}$, assumes a value equal to $1 - w^{(1)}$, which is equal to the equivalent undamaged area of the original material. Conversely, the energy-based damage parameter can be interpreted as an equivalent damaged area fraction at a given material point in the context of the cohesive zone framework. A schematic of the traction-separation relations for a material point under damage and healing is shown in Fig.4.1 depicting the features of the model.

In accordance with (4.1) and (4.3), the effective fracture energy $\tilde{G}_{\mathrm{c}}$ of the composite material after healing becomes the weighted sum of the fracture energies of the

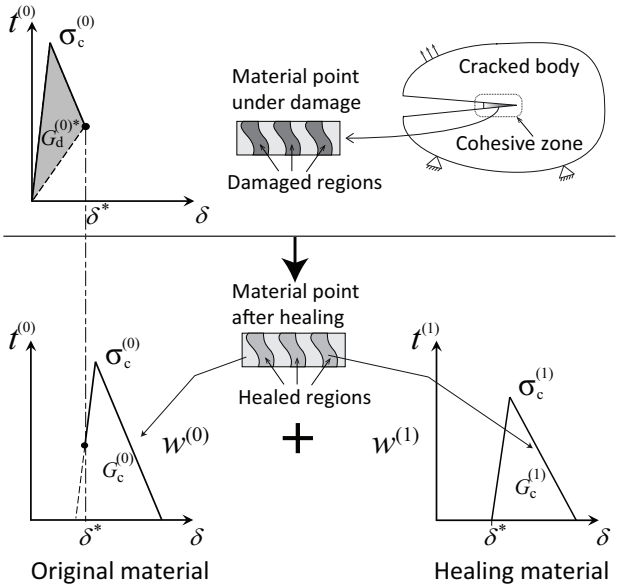

Figure 4.1: Traction-separation laws of original and healing material, which upon weighted addition, results in a composite cohesive relation for the crack-healing model.

original and healing materials, given as

$$\tilde{G}_c = w^{(0)} G_c^{(0)} + w^{(1)} G_c^{(1)} \,. \tag{4.4}$$

TRACTION-CRACK OPENING RELATIONS: ORIGINAL MATERIAL

The traction-separation relation corresponding to the original material *after healing* is governed by a modified effective displacement-based cohesive crack model explained as follows: The effective displacement for the original material defined in the conventional cohesive zone model is modified by introducing shifts in normal and tangential crack opening displacements to take into account the effect of healing. These shifts in the crack opening displacements lead to a modified effective displacement for the original material, $\Delta^{(0)}$, given as

$$\Delta^{(0)} := \sqrt{\left\langle \delta_n - \delta_n^{(0)^*} \right\rangle^2 + \gamma^2 (\delta_s - \delta_s^{(0)^*})^2}, \quad t \geq t^* \,. \tag{4.5}$$

The reason for introducing the shift is as follows: On activation of a healing process, the healing agent diffuses/flows through the crack and crack filling occurs thereby (fully or partially) reducing the crack opening. As a result, the crack opening displacements after complete healing should be considered nominally zero. To simulate this process, displacement shifts are introduced into the crack opening displacements, which make the nominal opening displacement zero upon complete

healing. Further, a shift is also applied in the crack opening history variable, κ, which is reset to its initial value. This is done to simulate the intact portion of the original material point, whereas the damaged portion of the considered material point is assumed to be healed by the healing material.

In a cohesive-zone model, a partially-damaged material has a non-zero crack opening displacement but it may still be capable of transmitting a force. In the present model, if healing is activated in a partially damaged surface, it is assumed that the process occurs at constant stress provided there is no change in the external loading.

The shifts introduced in the normal and the tangential crack opening displacements for the original material are given as follows:

$$\begin{aligned} \delta_{\mathrm{n}}^{(0)*} &= \delta_{\mathrm{n}}^{*} - t_{\mathrm{n}}^{*}/(w^{(0)}K)\,, \\ \delta_{\mathrm{s}}^{(0)*} &= \delta_{\mathrm{s}}^{*} - t_{\mathrm{s}}^{*}/(w^{(0)}K)\,. \end{aligned} \tag{4.6}$$

In the above expressions, δ_{n}^{*} and δ_{s}^{*} are the actual crack opening displacements in the original material at the instant of crack healing activation. As shifts in crack opening displacements are introduced along with restoration of the crack opening history variable κ, the shifts in crack opening displacements are constructed in such a way that the tractions across the cohesive surface maintain their continuity. Consequently, the traction components t_{n}^{*} and t_{s}^{*} across the partially damaged surface remain the same before and after healing activation.

The normal and shear tractions corresponding to the original material during subsequent loading after healing are then obtained from the corresponding traction-separation relations (2.5) and (2.7) using the aforementioned equivalent opening $\Delta^{(0)}$, i.e.,

$$\begin{aligned} t_{\mathrm{n}}^{(0)} &= \begin{cases} \dfrac{(\delta_{\mathrm{n}} - \delta_{\mathrm{n}}^{(0)*})}{\Delta^{(0)}}\, T^{(0)} & \text{if} \quad \delta_{\mathrm{n}} > \delta_{\mathrm{n}}^{(0)*}, \\ K(\delta_{\mathrm{n}} - \delta_{\mathrm{n}}^{(0)*}) & \text{if} \quad \delta_{\mathrm{n}} < \delta_{\mathrm{n}}^{(0)*}, \end{cases} \\ t_{\mathrm{s}}^{(0)} &= \gamma^2 \frac{(\delta_{\mathrm{s}} - \delta_{\mathrm{s}}^{(0)*})}{\Delta^{(0)}}\, T^{(0)}\,. \end{aligned} \tag{4.7}$$

TRACTION-CRACK OPENING RELATIONS: HEALING MATERIAL

Similar to the original material, the traction-separation relations corresponding to the healing material are governed by a modified equivalent displacement variable, $\Delta^{(1)}$ defined as

$$\Delta^{(1)} := \sqrt{\left\langle \delta_{\mathrm{n}} - \delta_{\mathrm{n}}^{(1)*} \right\rangle^2 + \gamma^2 (\delta_{\mathrm{s}} - \delta_{\mathrm{s}}^{(1)*})^2}\,, \tag{4.8}$$

where $\delta_{\mathrm{n}}^{(1)*}$ and $\delta_{\mathrm{s}}^{(1)*}$ are shifts applied to the traction-separation relation of the healing material. The shifts are introduced into the crack opening displacements of the healing material following the same approach as for the original material. The main difference is that the healing material is assumed to transmit zero load at the instant of healing activation. Thus, the shifts in crack opening displacements for the

healing material are the actual crack opening displacements at the instant of healing activation, i.e.,

$$\begin{aligned} \delta_{\mathrm{n}}^{(1)*} &= \delta_{\mathrm{n}}^{*} \\ \delta_{\mathrm{s}}^{(1)*} &= \delta_{\mathrm{s}}^{*}. \end{aligned} \tag{4.9}$$

Similar to the approach adopted for the original material after healing, the normal and tangential traction components corresponding to the healing material are obtained from an equivalent traction $T^{(1)}$ of the corresponding traction-separation relations (2.5) and (2.7) using the equivalent opening $\Delta^{(1)}$, i.e.,

$$\begin{aligned} t_{\mathrm{n}}^{(1)} &= \begin{cases} \dfrac{(\delta_{\mathrm{n}} - \delta_{\mathrm{n}}^{(1)*})}{\Delta^{(1)}}\, T^{(1)} & \text{if} \quad \delta_{\mathrm{n}} > \delta_{\mathrm{n}}^{(1)*}, \\ K(\delta_{\mathrm{n}} - \delta_{\mathrm{n}}^{(1)*}) & \text{if} \quad \delta_{\mathrm{n}} < \delta_{\mathrm{n}}^{(1)*}, \end{cases} \\ t_{\mathrm{s}}^{(1)} &= \gamma^2 \frac{(\delta_{\mathrm{s}} - \delta_{\mathrm{s}}^{(1)*})}{\Delta^{(1)}}\, T^{(1)}. \end{aligned} \tag{4.10}$$

It is worth noticing that, in both the original and healing material phases, the shifts in the crack opening displacements are applied at the component level, i.e., individually on the normal and tangential components. The composite tractions $\tilde{t}_{\mathrm{n}}$ and $\tilde{t}_{\mathrm{s}}$, given in (4.1), are obtained through a rule-of-mixtures approach analogous to an equal strain assumption used for composite materials (in this case an equal crack opening assumption) with material-specific responses given by (4.7) and (4.10). This approach provides sufficient flexibility to specify separate material properties and fracture behavior for the original and healing materials.

4

MULTIPLE HEALING EVENTS

The approach presented in the previous section can be extended to account for multiple healing events. This generalization is capable of dealing with a complex history of (partial) crackings and healings. In the sequel, the index p refers to the number of healing events, ranging from 0 to m, with the convention that $p = 0$ represents the undamaged original state. The index p may also be used to represent the healing material phase that is formed during the p^{th} healing event, again with the convention that $p = 0$ corresponds to the original material. At the end of the m^{th} healing event, the composite-like traction components $\tilde{t}_{\mathrm{n}}^{[m]}$ and $\tilde{t}_{\mathrm{s}}^{[m]}$ of the multiply-healed material are given by

$$\tilde{t}_{\mathrm{n}}^{[m]} = \sum_{p=0}^{m} w^{[m](p)}\, t_{\mathrm{n}}^{(p)} \qquad \tilde{t}_{\mathrm{s}}^{[m]} = \sum_{p=0}^{m} w^{[m](p)}\, t_{\mathrm{s}}^{(p)} \tag{4.11}$$

where $t_{\mathrm{n}}^{(p)}$ and $t_{\mathrm{s}}^{(p)}$ are the normal and tangential traction components of the p^{th} material phase and $w^{[m](p)}$ is the volume fraction of the p^{th} material phase (index in parentheses) present or created at the m^{th} healing event (index in square brackets). The relation given in (4.11) is a generalization of (4.1) for the case $m > 1$. For modelling

purposes, a separate index is assigned to each new healing material created at the p^{th} healing event even though the actual materials (chemical composition) may be physically the same. The purpose is to keep track of their individual evolutions throughout a complex loading and healing process starting at possibly different states (i.e., every healing instance is recorded separately). In accordance with the proposed constitutive model for the single healing event, it is assumed that the volume fraction $w^{[m](p)}$ of the p^{th} material phase is related to the energy-based damage parameter of that phase prior to the m^{th} healing event, which can be expressed recursively as

$$w^{[m](p)} = \begin{cases} 1 & \text{for } p = m = 0, \\ w^{[m-1](p)}(1 - D^{[m](p)}) & \text{for } 1 \le p < m\,, \\ \sum_{p=0}^{m-1} w^{[m-1](p)} D^{[m](p)} & \text{for } 1 \le p = m\,. \end{cases} \tag{4.12}$$

In the above expression, $D^{[m](p)}$ is the value of energy-based damage parameter $D^{(p)}$ corresponding to the p^{th} healing phase at the m^{th} healing event. With this notation, the term $D^{(0)^*}$ in (4.3) can alternatively be expressed as $D^{[1](0)}$ to indicate the value of the energy-based damaged parameter evaluated at the instant at which the first healing event is activated. It is also to be noted that the sum of all $w^{[m](p)}$ is equal to 1, where p ranges from 0 to m.

The fracture energy $\tilde{G}_{\text{c}}^{[m]}$ of a multiply-healed composite-like crack, which is a generalization of (4.4) for $m > 1$, corresponds to the weighted sum of the fracture energies of the phases $p = 0, \dots m-1$ available before healing activation and the fracture energy of the latest formed healing material $p = m$, i.e.,

$$\tilde{G}_{\text{c}}^{[m]} = \sum_{p=0}^{m} w^{[m](p)} G_{\text{c}}^{(p)}\,. \tag{4.13}$$

At the m^{th} healing event, there are $m+1$ material phases at a material point within the cohesive zone for which the tractions in each phase are governed by the corresponding cohesive relations. The shifts in the crack opening displacements are obtained for each phase such that the continuity of the tractions is maintained within each phase, similar to the equations for the shifts given by (4.6) and (4.9).

For subsequent use, the expressions for the volume fractions $w^{[m](p)}$ in the case of two healing events are obtained explicitly from (4.12) with $m = 2$, i.e.,

$$\begin{aligned} w^{[2](0)} &= w^{[1](0)}(1 - D^{[2](0)}) = (1 - D^{[1](0)})(1 - D^{[2](0)})\,, \\ w^{[2](1)} &= w^{[1](1)}(1 - D^{[2](1)}) = D^{[1](0)}(1 - D^{[2](1)})\,, \\ w^{[2](2)} &= w^{[1](0)} D^{[2](0)} + w^{[1](1)} D^{[2](1)} = (1 - D^{[1](0)}) D^{[2](0)} + D^{[1](0)} D^{[2](1)}\,. \end{aligned} \tag{4.14}$$

The damage in the original material up to the first healing event is reflected in the value $D^{[1](0)}$ whereas the subsequent damage in the original material and the first

healing material is accounted for, respectively, through the values $D^{[2](0)}$ and $D^{[2](1)}$. The corresponding composite traction and fracture energy after the second healing event can be computed from (4.11) and (4.13).

4.2.2. NUMERICAL IMPLEMENTATION

The cohesive crack healing model described above can be implemented in a finite element framework using cohesive elements (or using an XFEM approach). In the context of a finite element solution procedure performed using a Newton-Raphson iterative approach, the contribution of the cohesive elements to the global stiffness matrix is provided by their element-wise consistent tangent matrix, which corresponds to the derivative of the traction vector with respect to the crack opening displacement. With respect to a local coordinate system normal (n) and tangential (s) to the crack, the components of the tangent matrix are, in view of (4.11), given by the weighted constitutive (material) tangents of each phase p, i.e.,

$$\frac{\partial \tilde{t}_i^{[1]}}{\partial \delta_j} = \sum_{p=0}^{m} w^{[m](p)} \frac{\partial t_i^{(\mathrm{p})}}{\partial \delta_j} \,, \quad i = \mathrm{n}, \mathrm{s}, \quad j = \mathrm{n}, \mathrm{s} \,. \tag{4.15}$$

Correspondingly, the tangent matrix of the composite-like model requires the individual contributions from the phases. The expressions for the constitutive stiffness tangents depend on the loading-unloading conditions, as indicated in (2.4), applied separately for each phase p.

4

UNDER SOFTENING CONDITION:

For $f^{(p)} = 0$ and $\dot{\kappa}^{(p)} > 0$, the components of the consistent tangent matrix for the phase p are obtained, assuming that $\Delta_{\mathrm{i}}^{(p)} \ll \Delta_{\mathrm{f}}^{(p)}$, from (2.5), (2.6), (4.5) and (4.7), as follows:

$$\frac{\partial t_{\mathrm{n}}^{(p)}}{\partial \delta_{\mathrm{n}}} = \sigma_{\mathrm{c}}^{(p)} \left[\frac{1}{\Delta^{(p)}} - \frac{1}{\Delta_{\mathrm{f}}^{(p)}} - \frac{\left\langle \delta_{\mathrm{n}} - \delta_{\mathrm{n}}^{(p)*} \right\rangle^2}{(\Delta^{(p)})^3} \right] ,$$

$$\frac{\partial t_{\mathrm{s}}^{(p)}}{\partial \delta_{\mathrm{s}}} = \gamma^2 \sigma_{\mathrm{c}}^{(p)} \left[\frac{1}{\Delta^{(p)}} - \frac{1}{\Delta_{\mathrm{f}}^{(p)}} - \frac{\gamma^2 \left(\delta_{\mathrm{s}} - \delta_{\mathrm{s}}^{(p)*} \right)^2}{(\Delta^{(p)})^3} \right] ,$$

$$\frac{\partial t_{\mathrm{n}}^{(p)}}{\partial \delta_{\mathrm{s}}} = \frac{\partial t_{\mathrm{s}}^{(p)}}{\partial \delta_{\mathrm{n}}} = -\frac{\gamma^2 \sigma_{\mathrm{c}}^{(p)} \left\langle \delta_{\mathrm{n}} - \delta_{\mathrm{n}}^{(p)*} \right\rangle \left(\delta_{\mathrm{s}} - \delta_{\mathrm{s}}^{(p)*} \right)}{(\Delta^{(p)})^3} \,.$$

UNDER UNLOADING/RELOADING CONDITIONS

For $f^{(p)} < 0$ and $\dot{\kappa}^{(p)} = 0$, the components of the consistent tangent matrix are, assuming that $\Delta_{\mathrm{i}}^{(p)} \ll \Delta_{\mathrm{f}}^{(p)}$, given as

$$\frac{\partial t_{\mathrm{n}}^{(p)}}{\partial \delta_{\mathrm{n}}} = \sigma_{\mathrm{c}}^{(p)} \left[\frac{1}{\kappa^{(p)}} - \frac{1}{\Delta_{\mathrm{f}}^{(p)}} \right] ,$$
$$\frac{\partial t_{\mathrm{s}}^{(p)}}{\partial \delta_{\mathrm{s}}} = \gamma^2 \sigma_{\mathrm{c}}^{(p)} \left[\frac{1}{\kappa^{(p)}} - \frac{1}{\Delta_{\mathrm{f}}^{(p)}} \right] ,$$
$$\frac{\partial t_{\mathrm{n}}^{(p)}}{\partial \delta_{\mathrm{s}}} = \frac{\partial t_{\mathrm{s}}^{(p)}}{\partial \delta_{\mathrm{n}}} = 0 .$$

The case of the initial "elastic" behavior can in principle be treated formally as a reloading case by assigning an initial damage $\kappa_0^{(p)} = \Delta_{\mathrm{i}}^{(p)}$. However, since in the previous formulas the term $\Delta_{\mathrm{i}}^{(p)}$ has been neglected, the tangent matrix can be separately specified as

$$\frac{\partial t_{\mathrm{n}}^{(p)}}{\partial \delta_{\mathrm{n}}} = \frac{1}{\gamma^2} \frac{\partial t_{\mathrm{s}}^{(p)}}{\partial \delta_{\mathrm{s}}} = K ,$$
$$\frac{\partial t_{\mathrm{n}}^{(p)}}{\partial \delta_{\mathrm{s}}} = \frac{\partial t_{\mathrm{s}}^{(p)}}{\partial \delta_{\mathrm{n}}} = 0 ,$$

where K is the cohesive stiffness, assumed in this case to be the same for all phases.

4.3. MODEL VERIFICATION AND TESTING

In this section, the model is tested using a simple three-element mesh as shown in Fig. 4.2, in which a single zero-thickness cohesive element is placed between two continuum elements of size 20μm $\times$ 20μm each. Several aspects are considered to study the behavior of the model, which include different loading conditions, number of healing events, properties of the healing material and the degree of damage.

4.3.1. FRACTURE AND HEALING IN MONOTONIC STRAINING

In the first set of test simulations, the three-element system is subjected to various monotonic straining conditions to study the behavior of the cohesive element under damage and healing. The loading conditions are prescribed through applied displacements as shown in Fig. 4.2. The time history of the specified displacement is shown in Fig. 4.3a, which corresponds to a three-stage deformation, namely (i) a nominally mode-I opening stage involving a linear increase in applied deformation, (ii) a rest period with healing at the maximum deformation reached in the first stage and (iii) a resumption of the mode-I deformation. In all the simulations, it is assumed that complete healing occurs at the end of the zero loading-rate time period (rest period). The post-healing behavior of the cohesive element corresponds to the third stage. For the present model, the actual duration of the rest period has no direct effect on the

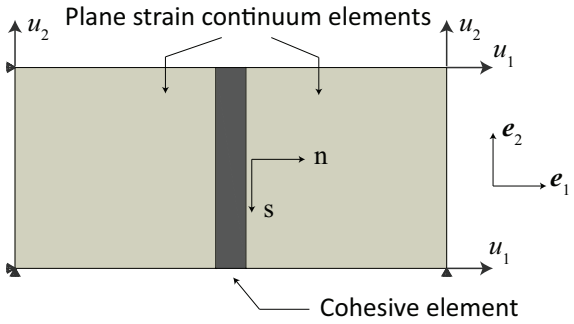

Figure 4.2: Three element model: An initially zero thickness cohesive element placed in between two continuum two dimensional plane strain elements.

simulations since the healing kinetics are not modelled explicitly; only the state of the healing material upon resumption of the loading is relevant. However, the healing period is indicated in the time history for clarity and to emphasize that healing is, in general, a process with time scales comparable to (and sometimes larger than) the time scales associated to mechanical loading.

For the conditions assumed in the simulation, the evolution of the stress in the cohesive zone in a three-element system only depends on the fracture properties but not on the elastic properties of the bulk material. The fracture properties of the original and healing materials are given as

$$\sigma_{\mathrm{c}}^{(0)} = 100\,\mathrm{MPa}\,, \quad \sigma_{\mathrm{c}}^{(1)} = 75,100\,\mathrm{MPa}\,, \quad \Delta_{\mathrm{f}}^{(0)} = \Delta_{\mathrm{f}}^{(1)} = 2\mu\mathrm{m}\,.$$

As indicated above, two values are considered regarding the fracture strength $\sigma_{\mathrm{c}}^{(1)}$ of the healing material, namely a lower strength compared to the original material (chosen as 75% of $\sigma_{\mathrm{c}}^{(0)}$) and an equal strength (100%). The healing materials and the original material have the same final crack opening Δ_{f}. In principle it is possible to consider the case of a healing material that has a higher strength, but in order to study that situation it is more relevant to carry out an analysis with more than one cohesive element where a secondary crack is allowed to initiate elsewhere.

The effective traction as a function of time is shown in Fig. 4.3b for both values of the fracture strength of the healing material. As shown in the figure, the traction in the cohesive element initially increases up to the value equal to cohesive strength $\sigma_{\mathrm{c}}^{(0)}$ of the original material and then decreases as a result of damage evolution. Complete failure occurs when the crack opening reaches the critical crack opening for failure $\Delta_{\mathrm{f}}^{(0)}$ of the original phase. Afterwards, the crack opening continues to grow due to the externally-imposed deformation at essentially zero stress. As indicated in Fig. 4.3a, healing is activated at $t = 100$ s (and is assumed to be completed at $t = 300$ s). Correspondingly, a shift in the crack opening of $\delta_{\mathrm{n}}^{(1)*} = 3\mu$m and $\delta_{\mathrm{s}}^{(1)*} = 0$ is taken into account and the loading is resumed. The maximum load is reached at the corresponding value of the fracture strength of the healing material $\sigma_{\mathrm{c}}^{(1)}$ for both cases

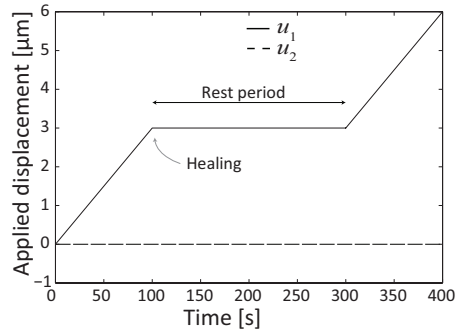

(a) Specified displacement-time history.

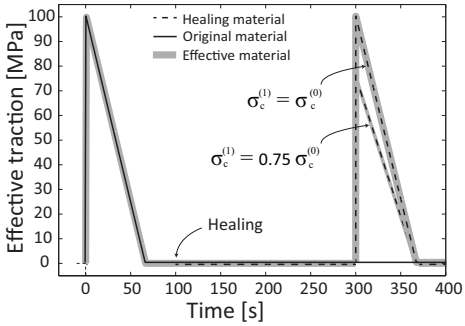

(b) Traction history in the cohesive element

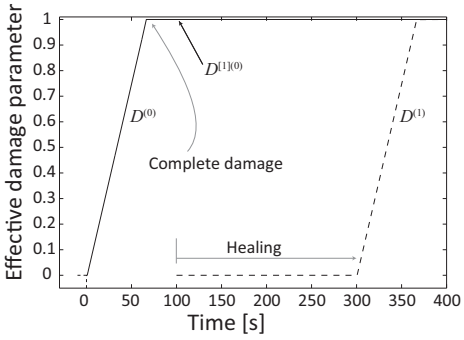

(c) Time history of damage

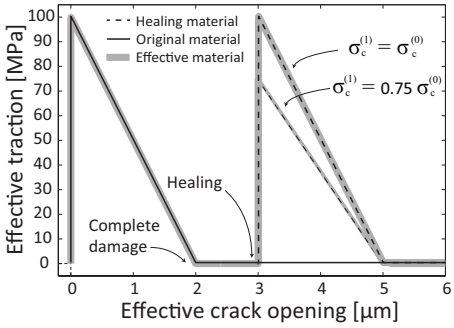

(d) Traction vs. crack opening

Figure 4.3: Case1: Illustration of response of cohesive element under monotonic straining, healing and further straining. The response includes the cases of healing materials with fracture strengths equal 75% and 100% of the strength of the original material.

considered (75% and 100%). The loading continues in the softening (degradation) regime until the healing material completely fails, which occurs when the shifted crack opening is such that $\Delta^{(1)} = \Delta_f^{(1)}$.

The effect of the damage due to loading and the recovery due to healing can be seen in Fig. 4.3c in terms of the relevant damage variables as a function of time. During the first stage of loading, the damage variable $D^{(0)}$ of the original material increases from 0 to 1, which indicates that the original material undergoes full damage. The healing process in the second stage is not modelled explicitly but rather provided as input for the cohesive model to analyze the recovery of strength. During that process, the damage variable $D^{(0)}$ of the original material remains at 1 while the damage variable $D^{(1)}$ of the healing material becomes active with an initial value equal to zero (no damage). During the third stage of the process, the damage variable $D^{(1)}$ of the healing material increases from 0 to 1, hence at the end of the loading process the healing

material is also fully damaged.

The results of the simulation can also be reported in terms of the traction across the cohesive interface as a function of the crack opening displacement as shown in Fig. 4.3d. Although the loading process in this example is relatively simple, it illustrates the importance of using the shift in the crack opening variable to properly simulate the evolution of stress during healing. Indeed, as may be observed in Fig. 4.3d, the material follows the expected cohesive response starting from the value $\Delta^{(1)} = 3\mu$m as a new origin after healing.

4.3.2. MULTIPLE HEALING OF A PARTIALLY-DAMAGED MATERIAL

The next example to illustrate the features of the model pertains to multiple healing of a partially-damaged material. In this case, the material is loaded and healed according to the applied deformation shown in Fig. 4.4a. As indicated in the figure, the material is initially extended and undergoes partial damage. Subsequently the material is healed and the loading is resumed, which generates partial damage of the original and the healing material. The material then experiences a second healing event before loading is resumed until final failure. In this simulation, the fracture strength of the healing materials are chosen as $\sigma_c^{(1)} = \sigma_c^{(2)} = 0.75\sigma_c^{(0)}$ with the actual values as indicated in the previous subsection.

The evolution of the effective (composite) normal traction $\tilde{t}_n^{[m]}$ and the phase-weighted tractions $w^{[m](p)} t_n^{(p)}$ are shown in Fig. 4.4b as a function of time. The effect of healing on the fracture strength is reflected in the distinct peak values of the response. The first peak corresponds to the fracture strength $\sigma_c^{(0)}$ of the original material. The second peak lies between the one of the original material and the healed material since the original material was not fully damaged before healing was activated, hence it partly contributes to the effective (composite) fracture strength. In that case the strength is $w^{[1](0)} t_n^{(0)} + w^{[1](1)} \sigma_c^{(1)}$, with $t_n^{(0)}$ being the stress on the original material at the instant that the stress on the first healing material reaches its critical value. Similarly, the third peak contains contributions from the three phases that are active at that instant, namely it is given by $w^{[2](0)} t_n^{(0)} + w^{[2](1)} t_n^{(1)} + w^{[2](2)} \sigma_c^{(2)}$, with $t_n^{(0)}$ and $t_n^{(1)}$ being the stresses on the original and first healing material at the instant that the stress on the second healing material reaches its critical value.

The evolution of the damage parameter for each phase is shown in Fig. 4.4c, where it can be seen that the rate of damage per phase decreases as the number of active phases increases (i.e., the damage gets distributed among the different phases, with the largest rate corresponding to the most recently created phase). The effective traction-separation relation for multiple healing of a partially-damaged material is shown in Fig. 4.4d. The effective fracture energy, as given by (4.13), depends on the number of healing events and the volume fractions $w^{[m](p)}$. As may be inferred from Fig. 4.4d, the total fracture energy of the material, measured as the area under the curve, increases as a result of the healing process compared to the original material.

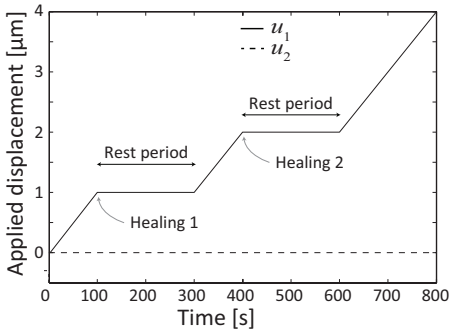

(a) Specified displacement-time history.

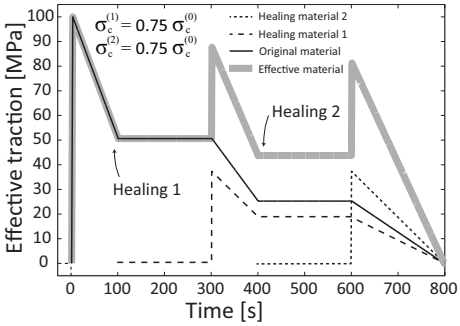

(b) Traction history in the cohesive element

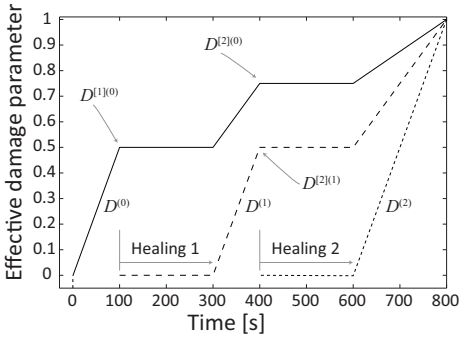

(c) Time history of damage

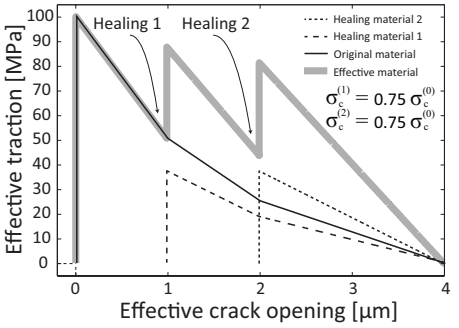

(d) Traction vs. crack opening

Figure 4.4: Case 2: Illustration of response of cohesive element considering multiple damage and healing events. The fracture strength of the healing material is assumed to be equal to 75% of that of the original material.

4.3.3. UNLOADING AFTER HEALING OF PARTIALLY-DAMAGED MATERIAL

In order to validate the unloading features of the cohesive model, the three-element system is subjected to a loading and healing process as indicated in Fig. 4.5a. In this case the material is extended, undergoes partial damage after which extension is resumed and finally the material is unloaded. The unloading is specified in terms of displacement, which ends at the displacement for which the stress vanishes. The fracture strength of the healing material is taken as $\sigma_c^{(1)} = 0.75\sigma_c^{(0)}$. The effective traction as a function of crack opening is shown in Fig.4.5b. As may be observed in the figure, upon unloading, the stress returns elastically to zero along the corresponding unloading curve of each phase, which depends on the damage parameter of the specific phase. The stress is zero at the crack opening displacement at which healing occured according to the shift parameters given in (4.6) and (4.9).

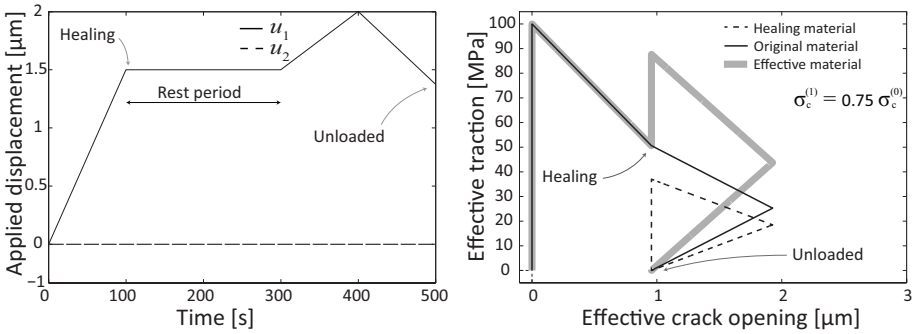

(a) Specified displacement-time history. (b) Traction vs. crack opening displacement

Figure 4.5: Case 3: Partial damage, healing, partial damage and unloading. The fracture strength of the healing material is assumed to be equal to 75% of that of the original material.

Other loading cases, not shown here for conciseness, indicate that the model is able to predict the behavior under complex sequences of mixed-mode loading, unloading and healing. The application of the healing cohesive model under non-homogeneous conditions is analyzed in the following section.

4.4. APPLICATION TO AN EXTRINSIC SELF-HEALING MATERIAL

In this section, the cohesive healing model is applied to a unit cell of an extrinsic self-healing material in which a single healing particle is embedded within a matrix material as shown in Fig. 4.6. In extrinsic systems, the particle contains a healing agent (i.e., the material contained inside the particle) that is normally protected by an encapsulation system to prevent premature activation of the healing process. The working principle of this system is that the healing mechanism is activated when a crack that propagates through the matrix interacts with the particle, usually breaking the encapsulation and allowing transport of the healing agent through the crack. Some self-healing system may involve auxiliary materials that are necessary for triggering and/or participating in a subsequent chemical reaction to create the final form of the healing material. The present simulation assumes that any additional substance required for the process is readily available in the matrix material (e.g., free oxygen transported by diffusion required for oxidation as found in self-healing thermal barrier coatings [STD+15]). Distinct cohesive relations can be used at different spatial locations (matrix, particle, matrix-particle interface), hence phase-specific fracture properties can be specified for the healing agent inside the particle and the healing material that appears in the cracks after activation of the healing mechanism.

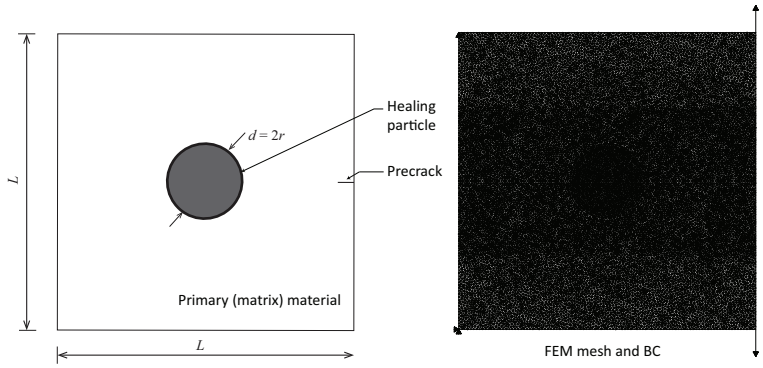

Figure 4.6: Geometry and finite element model of a unit cell of an extrinsic self-healing material. The unit cell is subjected to a nominal mode I loading. A small precrack is used to guide a matrix crack towards the particle. A layer of cohesive elements is placed to allow for crack propagation in a predefined direction given by the initial precrack.

As shown in Fig. 4.6, the unit cell used in the simulations is an $L \times L$ domain with a circular particle of a diameter $d = 2r$. For simplicity a two-dimensional computational domain under plane strain conditions is chosen, meaning that the particle should be interpreted as prismatic (fiber in the out-of-plane direction). Despite this interpretation, the model is assumed to be qualitatively representative of a spherical particle albeit with a different volume fraction. In the simulations the length is chosen as $L = 75\mu$m and the diameter as $d = 10\mu$m, which corresponds to a nominal (in-plane) particle volume fraction of 10%. In the finite element mesh, cohesive elements are inserted along a horizontal plane in the mid-height of the model, by which the crack is allowed to propagate along the pre-defined path. In principle, arbitrary crack growth can be modelled by inserting cohesive elements along all bulk elements in mesh, although that approach is not required for purposes of the present study [PTvdZ15]. The finite element mesh is sufficiently resolved so that proper discretization of the cohesive zone is ensured. Displacement-driven nominal mode I load is applied by specifying vertical displacements at the corner nodes on the right side of the domain while the corner nodes at the left are fixed as shown in the figure. Both the matrix and the healing particle are assumed to be isotropic and linearly elastic up to fracture. For the sake of simplicity, the material properties (both elastic and fracture) of the matrix and the healing particle are kept the same and the values are given as follows:

$$E^{\mathrm{m}} = E^{\mathrm{p}} = 150\ \mathrm{GPa}\,,\ \nu^{\mathrm{m}} = \nu^{\mathrm{p}} = 0.25\,,$$
$$\sigma_{\mathrm{c}}^{\mathrm{m}} = \sigma_{\mathrm{c}}^{\mathrm{p}} = \sigma_{\mathrm{c}}^{(0)} = 400\ \mathrm{MPa}\,,\ G_{\mathrm{c}}^{\mathrm{m}} = G_{\mathrm{c}}^{\mathrm{p}} = G_{\mathrm{c}}^{(0)} = 100\ \mathrm{J/m^2}\,,$$

where E and ν refer to Young's modulus and Poisson's ratio, respectively, and the superscripts m and p refer to the matrix and the particle, respectively. Since the properties of the particle and the matrix are assumed to be equal, the original material, as indicated by the superscript 0, refers to either the particle or the matrix

depending on location. The interface between the particle and the matrix is assumed to be perfectly bonded and interface fracture is taken not to occur. It is worth pointing out that in general the elastic and fracture properties of the healing particle and the matrix are different, which in fact decide whether a matrix crack would break the healing particle or not. This aspect of a matrix crack interacting with healing particles of different properties compared to the matrix is dealt in detail in [PTvdZ15] but is not relevant for the simulations presented in this section. Instead, the emphasis is placed here on how the crack healing behavior affects the recovery of mechanical properties of the material. Further, as indicated above, the fracture properties of the healing particle in its initial state are in general different than the properties of the healing material that fills the cracks, which are specified separately as explained in the sequel.

Several parametric studies are conducted to evaluate the behavior of the unit cell and the results in terms of global load-displacement response are reported in the following subsections. In the first subsection, simulations are conducted to study the effect of variations in the fracture properties of the healing material. In the second subsection, a parametric study is performed to understand how does the available amount of healing agent affect the crack healing behavior. In the third subsection, multiple healing events are simulated and the resulting load-displacement response is reported.

4.4.1. EFFECT OF PROPERTIES OF HEALING MATERIAL AND HEALING CONDITIONS

The fracture properties of the healing material, formed as the result of the healing process, are often different from the surrounding host material. The fracture properties of the healed zone depend on the time available for healing and the properties of the healing product. A second aspect that is relevant for the healing process is the loading conditions during healing. Healing is a process that typically requires time to occur, and the efficiency of the process is often connected to providing a sufficiently long "rest time" in which the loading rate is zero and chemical reactions have sufficient time to be completed. However, even if a sufficient "rest time" is provided, the (constant) loading state influences the subsequent material response of the healed material. In this section, two representative loading states during healing are considered, namely healing under zero-stress (unloaded) conditions and healing under fixed applied displacement (constant load during healing). Different properties for the healing material are considered for each loading state.

HEALING UNDER UNLOADED CONDITION

In the literature, most experimental studies deal with test protocols in which the sample is unloaded and allowed to return to its unstrained state, hence healing occurs under unloaded conditions [KSW03, BSW02, WTB07, PB05b, SPS+08]. In order to analyze the predictions of the model under similar conditions, the unit cell shown in Fig. 4.6 is subjected to a loading and healing sequence as indicated in Fig. 4.7a. Under this loading, the specimen is partially fractured and then unloaded. Healing

is allowed to occur in the unloaded condition, which is then followed by reloading of the healed specimen. The response of the unit cell in terms of the applied vertical displacement and the corresponding reaction force is shown in Fig. 4.7b for various fracture properties of the healing material, namely $\sigma_c^{(1)}/\sigma_c^{(0)}$, $G_c^{(1)}/G_c^{(0)}$ = 0.25, 0.5, 0.75 and 1, where the superscript 1 refers to the healing material. As shown in Fig. 4.7b, the curve corresponding to equal properties of the healing and original material predicts a recovery of the response after healing similar to that of the original material. The next three curves correspond to lower values of the fracture properties of the healing material and hence the load-displacement curves fall below that of the original material after healing.

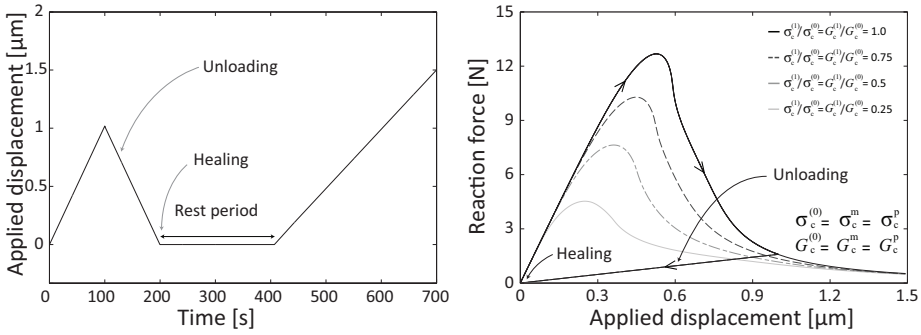

(a) Time history of the specified displacement. (b) Reaction force vs. applied displacement

Figure 4.7: Healing under unloaded condition: applied loading to unit cell and reaction force as a function of applied displacement for various values of the fracture properties of the healed material.

It is to be mentioned that, after healing, recracking occurs along the same path as the initial crack. This is due to the fact the fracture properties of the healing material are lower than or at least equal to that of the original material properties. Nonetheless, if the properties of the healing material are higher than that of the original material, the crack would propagate along a different path which is weaker than the healed zone. However, the recovered load-displacement response would be similar to the one with the same fracture properties, as the crack is traversing along the original material.

HEALING UNDER CONSTANT LOAD CONDITION

In situations of practical interest, healing may occur under a non-zero load, which implies that the crack opening is non-zero as the healing material fills the crack gap. To study the effect of the loading state during healing on the post-healing response of the material, simulations are carried out according to the loading sequence shown in Fig.4.8a. In this case, the specimen is (partially) fractured, allowed to heal at a constant applied displacement and subsequently reloaded. As in the previous case (healing at unloaded conditions), four different fracture properties of the healing material are

considered, given by the strength and fracture energy ratios $\sigma_c^{(1)}/\sigma_c^{(0)}$, $G_c^{(1)}/G_c^{(0)} = 0.25$, 0.5, 0.75 and 1. The load carrying capability of the healed specimens is shown in Fig. 4.8b, which indicates the reaction force of the unit cell as a function of the applied vertical displacement.

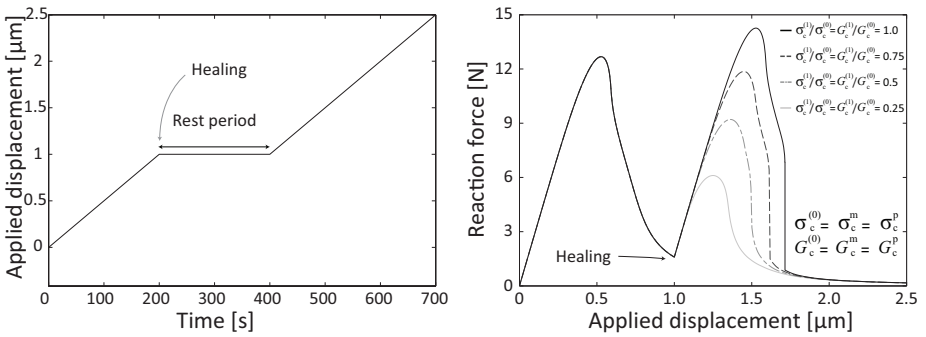

(a) Time history of the specified displacement. (b) Reaction force vs. applied displacement

Figure 4.8: Healing under constant loading condition: applied loading to unit cell and reaction force as a function of applied displacement for various values of the fracture properties of the healed material.

For each set of material properties of the healing material, the state of the specimen is the same prior to healing. After healing at a constant crack opening profile, the specimen recovers its load-carrying capability as shown in Fig. 4.8a. It can be observed that the post-healing force peak is higher than the force peak of the original material for the case when the healing material has the same fracture properties of the original material. This result is partly due to the equal strain kinematic assumption of the Voigt-like composite model, as indicated in Sec. 4.2.1.1, which tends to overpredict the force response. It is anticipated that a more complex composite model, which preserves both linear momentum and kinematic compatibility, would predict a lower post-healing peak. Although the present model provides an upper estimate of the post-healed behavior, it allows to compare the effect of the state of the material during healing on the post-healing behavior. In particular, the post-healing failure in the case of healing under loaded conditions is more sudden (i.e., qualitatively more brittle, see Fig. 4.8b) compared to the case of healing at an unloaded state (see Fig. 4.8b), except when the properties of the healing material are relatively low.

To gain more insight in the healing process under constant crack opening profile, the local response curves at selected locations are shown in Fig. 4.9 for the case when the properties of the healing material are $\sigma_c^{(1)}/\sigma_c^{(0)} = G_c^{(1)}/G_c^{(0)} = 0.5$. As can be observed in the figure, the crack openings at the instant of healing depend on location, with increasing values towards the side where the opening load is applied. Observe that some points undergo healing from a fully-failed state, some from a partially-failed state and some points that are cracked at the end of the loading process experienced

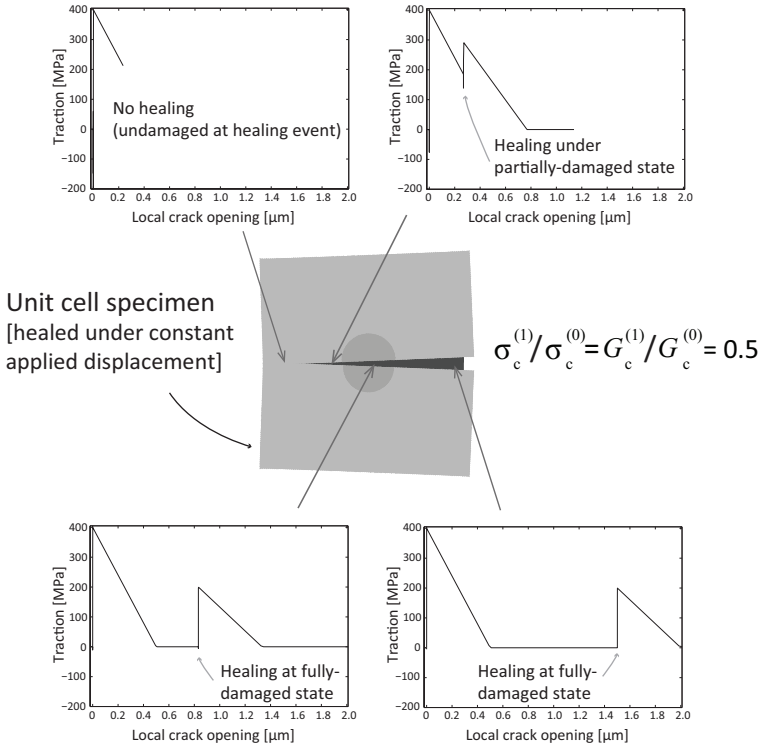

Figure 4.9: Unit cell specimen at the final state of the applied loading given in Fig. 4.8a. Representative local response curves illustrate how the introduction of a shift in the (local) crack opening displacement accounts for the proper origin upon resumption of the load after healing.

no healing since they had not failed at the instant at which healing was activated.

After healing, the effective crack opening displacements become zero in the healed zone due to the displacement shifts introduced in the model to account for crack filling. However, modelling of the crack gap filling and healing is done implicitly through the shift in crack opening displacements, whereby the new material is not explicitly modelled as an additional material (or mass) entering the system.

4.4.2. DEGREE OF CRACK FILLING AND HEALING

In the previous subsection, it was assumed that the healing particle, upon fracture, releases an amount of healing agent (denoted as V_h) that is sufficient for complete filling of the crack opening volume (or crack opening area in two dimension, denoted as V_c). However, depending on the amount of available healing material, the geometrical characteristics of the crack and the mode of transport, it may occur that the crack is only partially filled, which is a key factor affecting the healing characteristics and hence the recovery of mechanical properties. In this section, the effect of the ratio

V_h/V_c of healing agent available to the required healing agent for complete filling is studied. Here, the volume of required healing agent for complete crack filling refers to the total crack volume at the instance of healing activation. The ratio considered is generic and its interpretation in a specific self-healing material system requires understanding of its healing characteristics. For instance, the amount of healing material produced as the result of the healing process is directly related not only to the volume of the healing particle, but also the reaction kinetics of the healing process. For example, in one of the extrinsic self-healing systems reported in the literature, the healing agent within the particle produces healing material through increase in volume by oxidation under high temperature conditions [STD+15, PTZX15]. Hence, the term V_h means here the volume of the healing product formed as the result of the healing process, which is used for healing the crack. The notion of complete or partial filling, measured by the ration V_h/V_c, refers to the amount of crack gap filled with healing material regardless of the fracture properties of the healing material.

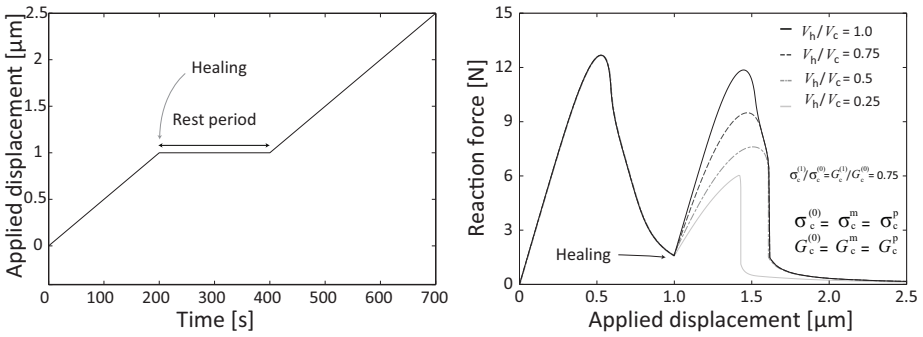

(a) Time history of the specified displacement. (b) Reaction for vs. applied displacement

Figure 4.10: Effect of filling efficiency: applied loading to unit cell and reaction force as a function of applied displacement for various values of healed areas

Simulations are conducted for four different healing processes with filling efficiencies of $V_h/V_c = 1$, 0.75, 0.5 and 0.25. In all cases the properties of the healing material are taken as $\sigma_c^{(1)}/\sigma_c^{(0)}$, $G_c^{(1)}/G_c^{(0)} = 0.75$. The specimens are loaded according to the sequence indicated in Fig. 4.10a and the corresponding force-displacement curves are shown in Fig. 4.10b. To interpret the results for partial filling, it is useful to indicate the spatial location where healing occurs, which is shown in Fig. 4.11. As indicated in the figure, filling is assumed to take place in the zone adjacent to the healing particle.

The curve shown in Fig. 4.10b corresponding to a complete filling (filling ratio $V_h/V_c = 1$) represents the highest possible recovery of the load-carrying capability for the given fracture properties of the healing material. As expected, the recovery of the load-carrying capability decreases with decreasing filling ratios $V_h/V_c = 0.75, 0.5, 0.25$. One relevant difference between the effect of a decrease in filling efficiency and a

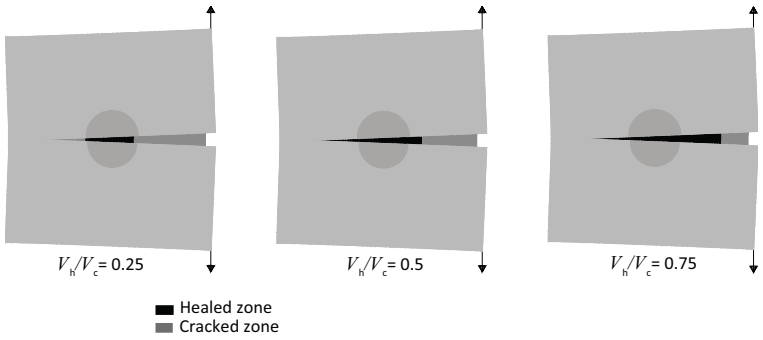

Figure 4.11: Specimen showing the healed cohesive cracks for various degrees of crack filling. For the purpose of clarity, the deformed specimen has a scaling factor of 3

decrease in the fracture properties of the healing material for a fixed filling efficiency is that in the latter case the initial slope of the post-healed behavior remains the same for distinct fracture properties whereas in the former case the initial slope decreases with decreasing filling efficiency (compare Fig. 4.8b and Fig. 4.10b). In the simulations shown in Fig. 4.10b, the initial post-healing slope reflects the increase in compliance due to purely geometrical effects. The un-healed portion of the crack facilitates the (elastic) deformation of the specimen. This effect may potentially be used in the interpretation of experimental curves as an indication of partial filling of a crack.

4.4.3. MULTIPLE HEALING EVENTS

Some materials with intrinsic self-healing capacity (such as MAX phases), may undergo multiple healing events whereby a crack is healed on multiple occasions [LSK+12, SPM+16]. In extrinsic systems, multiple healing may occur in cases where there is an external supply of healing material, but also in particle-based systems when inactivated particles (or portions of partially activated particles) can still supply healing material for an additional healing event . In this section, it is assumed that the particle in the unit cell shown in Fig. 4.6 is capable of providing sufficient healing material for two healing events. The specimen is subjected to a loading and healing process as shown in Fig. 4.12a. The ratio of crack opening volume (or area) to the available healing material volume is assumed to be 1 for both healing events, resulting in complete filling of the crack. The fracture properties of the healing material after the first healing event are taken as 75% of those of the original material, while for the second healing event, the properties are taken as 50% of that of the original material, hence $\sigma_c^{(1)}/\sigma_c^{(0)}$, $G_c^{(1)}/G_c^{(0)} = 0.75$ and $\sigma_c^{(2)}/\sigma_c^{(0)}$, $G_c^{(2)}/G_c^{(0)} = 0.5$. This assumption is meant to implicitly represent a degradation on the quality of the healing material after the first healing event.

The reaction force on the unit cell is shown in Fig. 4.12b as a function of the applied vertical displacement. As can be observed in the figure, the load carrying capacity may be (partially) recovered multiple times provided that the self-healing

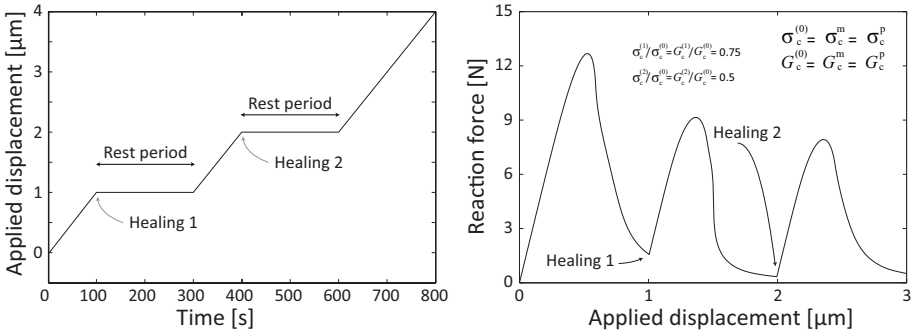

(a) Time history of the specified displacement. (b) Reaction force vs. applied displacement

Figure 4.12: Effect of multiple healing: applied loading to unit cell and reaction force as a function of applied displacement for two healing events

mechanism supplies sufficient healing material for multiple healing events. Although a single healing event can naturally extend the lifetime of a material, a more significant extension can be achieved in a material capable of multiple self healing repairs, even if the quality of the healing material degrades during subsequent healing events. The model developed here may be used for design purposes to optimize the characteristics of a healing particle and/or a cluster of healing particles by further investigating convenient particle characteristics or particle arrangements that provide the capacity of multiple healing events. This may be achieved by, for example, embedding particles large enough to serve as a reservoir for multiple healing events or by placing a cluster of particles that may be activated sequentially as cracks re-appear in a material at adjacent locations. Although those studies are beyond the scope of the current work, the present model may be employed to simulate the recovery of strength and fracture energy under complex loading histories.

4.5. SUMMARY AND OUTLOOK

A cohesive zone-based computational framework for analyzing self-healing materials is presented to model the recovery of mechanical properties. Salient features of the composite model are demonstrated through several test simulations. In particular, the capability of the model to simulate multiple healing events and handling different fracture properties of the healing material for each healing event is relevant for analyzing several realistic self-healing materials. The model can be applied for either extrinsic or intrinsic self-healing material systems with an appropriate coupling to healing kinetics in each case.

For a unit cell of an extrinsic self healing material, the simulations show that the recovery of the load carrying capacity upon healing depends both on the fracture

properties of the healing material that fills the cracks as well as the filling efficiency, which may be seen as a geometrical characteristic. Further, it is found that the post-healed behavior of a material healed under loaded conditions appears to be more brittle than for a material healed under unloaded conditions, although this conclusion is based on the assumption that the healing material has the same fracture properties in both cases, which may not be necessarily the case in some self-healing materials. The simulations also indicate that the characteristics of the initial post-healing response in a force-displacement diagram may be used as an indicator of the filling efficiency of a healing event whereby an initial response similar to that of the original material corresponds to maximum crack filling efficiency regardless of the fracture properties of the healing material. A decrease in the initial post-healing force-displacement slope compared to the initial slope of the original material is an indication of an incomplete filling process, again regardless of the fracture properties of the healing material.

The developed framework does not explicitly model the crack healing kinetics, rather the results of the healing process are provided as input parameters to the model. Nonetheless, the coupling of crack healing kinetics into the model is in principle straightforward in the form of the amount of healing material produced as the result of the healing process, which is then geometrically related to the crack volume healed. For modelling purposes, it is also possible to treat the properties of the healing material as a variable during multiple healing events to implicitly account for a continuous degradation in the healing quality. In general, the model may be used for designing new self-healing material systems with the capacity of undergoing multiple healing events and, correspondingly, extending significantly the lifetime of a material with minimal external intervention.

5

APPLICATION OF THE HEALING MODEL TO A SELF-HEALING MAX PHASE CERAMIC SYSTEM: EXPERIMENTAL OBSERVATIONS AND COMPARISONS

In the previous chapter, a generalised modelling framework based on cohesive zone fracture mechanics is presented to analyse cracking and healing of a self-healing material, taking into account the fact that the mechanical properties of the base material and the reaction product formed in the healed crack may be different. In the present chapter, an attempt is made to apply the developed numerical model to simulate fracture and healing behaviour of an intrinsic self-healing material. The material under consideration is a MAX phase ceramic, Ti_2AlC, in which the monatomic thick layer of aluminium atoms in the unit cell of the material acts as the intrinsic healing agent [SPS+08, LSK+12]. A diffusion-oxidation mechanism drives the healing process, resulting primarily in the formation of alumina (Al_2O_3). Once the crack is adequately filled, the reaction product binds the crack faces together. A chevron-notched wedge loaded test methodology is utilised for the experiments [1] to fracture the virgin and the healed specimens. Finite element modelling of the experimental set up in conjunction with the newly developed micromechanical healing model is utilised to simulate and compare the mechanical response of the virgin and healed specimens

[1] The physical experiments were conducted by collaborator, Ann-Sophie Farle from the Department of Materials Science and Engineering at 3mE Faculty, TU Delft. Modelling and simulation part of the chapter was conducted by the author.

obtained from the experiments. At the end, two different healing efficiencies are defined, which can be used to quantify the effectiveness of the healing mechanism.

5.1. INTRODUCTION

Quantification of healing efficiency in self-healing materials relies on the comparison of the mechanical response of reference, damaged and healed samples to determine the property regain as a result of the healing process. Several testing methodologies have been proposed and used for this purpose which include three or four point bending and modified double cantilever beam tests, to name a few [GLPCC07, PB05b, Bro11, FKC14]. To study the effectiveness of the healing in a more scientific than engineering method, it is necessary to have a carefully designed experimental test-up that is capable of studying the behavior of the specimens during fracture, healing and post-healing processes altogether in a sequential manner. This is particularly challenging for ceramic-based material systems due to their inherent brittleness which prevents controlled cracking, ie., generating the crack without splitting the sample into two separate pieces during testing.

Most of the existing experimental approaches work such that each sample can yield only data for only one particular condition (virgin, cracked or healing) leading to a high material consumption, a growing error margin and somewhat incomparable results. Standard four-point bending test [Sta17] requires slow and stable crack propagation to be considered valid, something not commonly achieved with MAX-phase ceramics. Furthermore, while MAX phases are considered to be relatively tough, four-point bending testing in ceramic materials often leads to full sample splitting and this mode of fracture renders the sample rather useless for quantitative determination of the recovery of its mechanical and fracture properties upon high temperature annealing. In contrast the combination of a new sample geometry, experimental setup and data processing protocol proposed by my research collaborators [FKT+18] allow controlled crack growth along a designated path without complete splitting of the sample and extraction of fracture properties via finite element modeling using cohesive zone elements. The experimental setup consists of a chevron notched specimen loaded by a rigid wedge, which, in turn, induces a controlled crack growth. Due to the crack tip being located within the sample at the end of the first fracture experiment, the partially cracked sample can thereafter be heat treated (or healed) and re-cracked to determine the composite properties after healing. The direct comparison of the fracture response in both conditions for a single Spark Plasma Sintering (SPS) produced Ti_2AlC sample is reported here.

Ti_2AlC was selected as the MAX phase material to be used as its high temperature healing behavior is relatively well documented [LSK+12]. Cracks in Ti_2AlC are healed by the formation of dense and well-adhering Al_2O_3 within the crack when heated in air to a high temperature, as demonstrated by in-situ high resolution 3D X-ray tomography [SPM+16]. Furthermore, non-catastrophic bending tests showed successive strength regain of bulk Ti_2AlC for up to seven healing cycles [LSK+12]. While the work reported in this chapter deals with only one (technically successful)

multi-step cracking and healing experiment, we believe the results reported here give a realistic indication of the actual material behavior and demonstrate the potential of the methodology to quantify the fracture behaviour of the virgin and healed specimens.

The main objective of the chapter is to quantify the fracture properties of the virgin and the healed ceramic specimens through numerical analysis developed in the previous chapters. In the literature, several healing models have been proposed and implemented in a numerical framework in order to model the property recovery of the material upon healing [BGL05, BGB06, VSLK12, VSL11, MS13, DAL12, XSKZ14, OON16, MG06, SR06, UKP09, AA15, OON16, ZCK+16]. However, very few studies exist in the literature which utilise the models to actually quantify the recovery of mechanical properties of specimens tested in real physical experiments [JD10, SSL15, SBNS17]. In this chapter, an attempt is made to utilise finite element modelling of the wedge experiment to simulate the fracture of the virgin specimen and re-fracture of the healed specimen and from this to quantify the property recovery of the specimen upon healing. For this purpose, the cohesive zone healing model developed in chapter 4 is applied.

5.2. MODIFIED WEDGE TEST FOR FRACTURE AND HEALING STUDIES

In this section, the experimental set-up and the inverse computational modelling approach for characterising the fracture and the property recovery in the MAX-phase ceramic, Ti_2AlC are briefly discussed. More detailed information on the experimental procedure can be found in [FKT+18], however, basic details are furnished for completeness. Following which, the most salient details of the finite element model employed for modelling both cracking and recracking after healing are provided here, but for the conceptual details building up the micromechanical model, the reader is referred to the previous chapter.

5.2.1. SPECIMEN MANUFACTURING AND TEST SETUP

Reactive sintering of Ti_2AlC was performed using a spark plasma sintering (SPS) furnace (HP D 25 SD, FCT Systeme GmbH, Germany). Starting powders of Ti (100 µm, >99.5%, TLS Technik GmbH & Co., Germany), Al (45 µm, > 99.99%, TLS Technik GmbH & Co., Germany) and Graphite (> 99.5, 6 µm, Graphit Kropfmühl AG, Germany) were mixed in a molar ratio of 0.85 : 1.05 : 1.15 for 12 h using a Turbula T2C Mixer (Willy A. Bachofer, Switzerland) with 5 mm alumina balls. Ti_2AlC disks with a diameter of 40 mm and 5 mm thickness were sintered at 1400^{o}C for 30 min.

The phase purity of the samples was determined via X-ray diffraction using a Bruker D8 ADVANCE diffractometer (Bruker, Germany) in the Bragg-Brentano geometry with a graphite monochromator and Co Kα radiation. The recorded X-ray diffractrograms were processed with Bruker software DIFFRAC.EVA 4.1 software. Elastic properties and Vickers Hardness were determined by Vickers indentation using

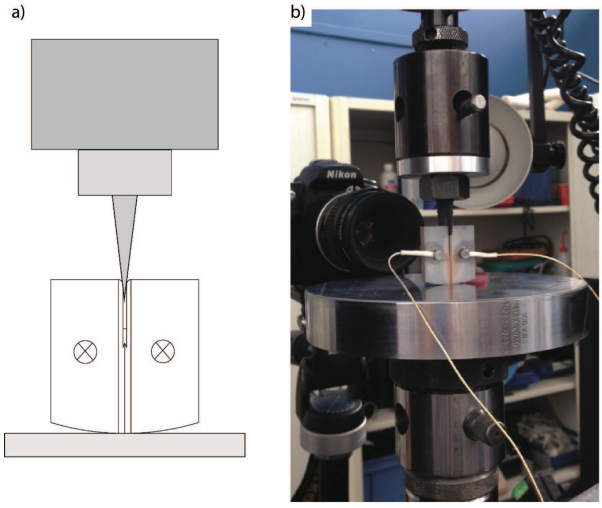

Figure 5.1: Experimental test set-up of the wedge-loaded chevron notched MAX-phase ceramic specimen: (a) Schematic of the test set-up; (b) Actual test set-up showing microphones for acoustic data acquisitions.

a hardness tester (Zwick-Z2.5, Germany). Indents were created by loading the indenter with 5 N/s up to 50 N, holding for 12 s and unloading with 3.7 N/s. The density of the material was measured with the Archimedes method using an analytical balance (Mettler Toledo AG-204, Switzerland) according to ASTM B-962 test standards. The Ti_2AlC samples had a relative density of 95% or higher. All machining was carried out by electric discharge machining (EDM) with wire diameters of 0.25 and 0.1 mm.

The details of the chevron-notched, wedge-loaded specimen geometry (WLS) are shown in Fig. 5.1 which contains a schematic of the test set-up and a picture of the actual test set-up. Samples with a basal half-length HW of 12 mm, a height W of 25 mm and thickness B of 5 mm were used. Experiments were carried out using a 100 kN electro-mechanical load frame (Series 5500R, Instron, USA) that was fitted with a 10 kN load cell to suit the recorded load levels. The sample was placed on a flat steel base-plate without further clamping. The quenched and tempered steel 10^oC wedge was lowered into the sample grove until it reached a pre-load of approximately 10 N. Tests were carried out under closed-loop displacement control, with a fixed crosshead displacement rate of 0.01 or 0.1 mm/s, monitored by a dynamic strain gauge extensometer (2620 Series, Instron). The crosshead motion was stopped when a load drop of 50 percent from peak load was recorded. Upon termination, the crosshead motion was reversed leading to retraction of the wedge. Unloading curves were not recorded. To determine the residual load bearing capacity, reloading of an un-oxidized specimen was performed up to 95% load drop.

All tests were accompanied by the recording of the acoustic events during the fracturing process, using the Physical Acoustics module (PCI-2, 2 channel 40 MHz

18 bit data-acquisition combined with ILS40 pre-amplifiers). Registration and post-processing were performed using the Physical Acoustics AEWin 1.70 (2005) software module. Prior to each experiment, two microphones were attached to the right and left of the sample groove using a paraffin wax as a reversible adhesive. A sampling rate of 2 MHz with a 20 dB amplification factor was used. An acoustic event was recorded if the signal level of any microphone exceeded 5 mV. The energies recorded varied over a wide range between 1 aJ to 1 nJ. A cumulative energy as a function of time, termed the "acoustic energy", was obtained through post-processing of the acoustic events. Samples subjected to healing were oxidized at 1200^{o}C for 2 hours in laboratory air using an alumina tube furnace (LTF 16/75/610, Lenton, UK) and cooled with a rate of 10^{o}C per minute. Subsequently, the healed sample was tested in the wedge set-up without applying any further treatment to the sample apart from cleaning the wedge-sample contact zone.

5.2.2. FINITE ELEMENT MODEL

The experimental set-up containing the wedge-loaded chevron-notched specimen is modelled in a finite element framework using Abaqus software. For computational efficiency, a two-dimensional finite element model of the set-up is considered and shown in Fig. 5.2. The three-dimensional features of the specimen such as the groove and the notch are simulated by assigning varying thickness to the corresponding finite elements in those regions. The steel wedge and the base support are discretised using two dimensional quadrilateral, linear plane stress elements, CPS4. For the specimen, the mesh consists predominantly of quadrilateral elements, but in the groove region, circled in Fig. 5.2, linear triangular elements, CPS3 are used to enable embedding cohesive elements. In particular, three layers of zero thickness cohesive elements are inserted between the existing continuum triangular elements. The behaviour of the cohesive elements is modelled using the bilinear cohesive zone model developed in chapter 4 and the bulk elements are assumed to be linear elastic and isotropic. In the finite element mesh, it is ensured that one of the layers of cohesive elements is inclined at an angle approximately equal to 45 degrees to the expected crack path direction, which facilitates a crack to take a different path than just following a straight line. This is particularly relevant and necessary in the context of self-healing material modelling. This is because, as the recracking occurs after completion of the healing process, the induced crack post-healing may take a different path adjacent to the original crack path, in case the healed crack is stronger and/or tougher than the host matrix material surrounding the healed crack or zone.

The value for the friction coefficient between the wedge and the specimen has been found to be very crucial for data interpretation from the experiments, hence becomes an important feature to consider it in the modelling procedure. To be precise, the measured load or the external work supplied is only partially spent to crack the specimen, the rest being spent to overcome the friction between the wedge and the specimen. Hence, appropriate modeling of the frictional effects is necessary to be able to extract the properties of the material under consideration. To achieve it,

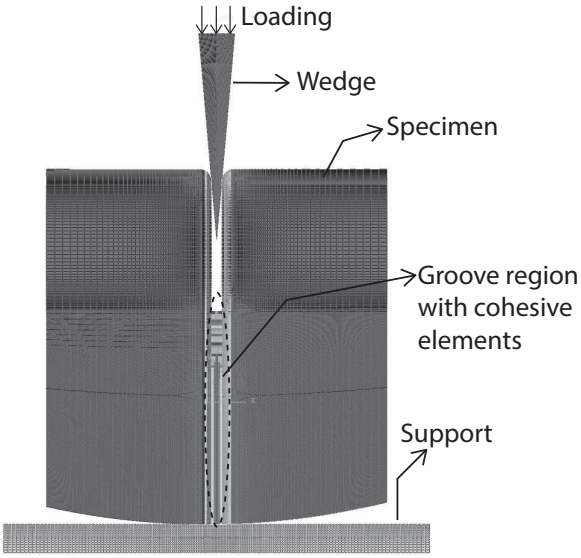

Figure 5.2: Finite element model of the test set-up showing the wedge in contact with the ceramic specimen supported underneath by a steel base. The model consists of 194560 finite elements which include three layers of 3350 cohesive elements present in the circled region to simulate cracking and healing.

adopting the methodology discussed in [FKT+18], the kinematic friction coefficient is calibrated for a Coulomb's friction model. After which, the extraction of the fracture properties, namely the cohesive strength and the fracture energy is done through fracture simulations involving cohesive elements. The approach is based on inverse modelling, whereby the fracture properties are varied until the simulated response matches with the experimental observations in terms of both the load-displacement response and the crack path. In the following section, experimental and numerical results corresponding to fracture of virgin and healed specimens are reported and the results are discussed in detail.

5.3. RESULTS AND DISCUSSIONS: COMPARISON OF SIMULATION RESULTS AGAINST EXPERIMENTAL DATA

5.3.1. FRACTURE OF VIRGIN SPECIMEN

The fracture response of the Ti_2AlC virgin specimen subjected to wedge loading is shown in Fig. 5.3. The crack growth is stable during loading, as can be seen from the recorded acoustic emission data shown in Fig. 5.4. In case the crack was to propagate catastrophically, it becomes difficult to control the loading process which would ultimately lead to complete splitting of the specimen, thereby making it unfeasible for subsequent quantitative self-healing testing.

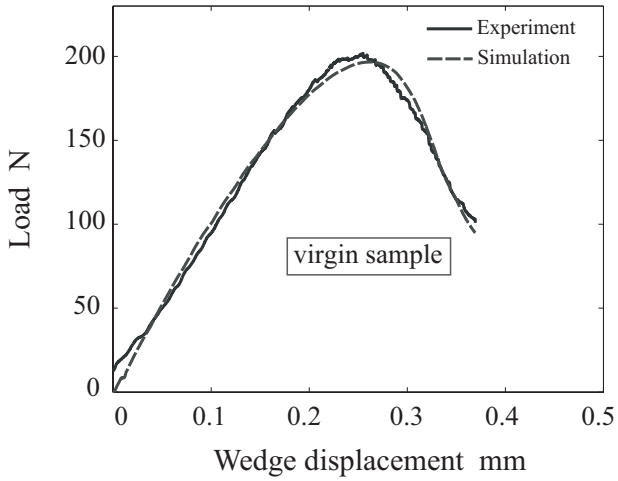

Figure 5.3: Load-displacement response of virgin specimen. Comparison between experiment and simulation. Material properties used for the simulation: fracture strength = 200 MPa, fracture energy = 1.5 N/mm, Young's modulus = 260 GPa, friction coefficient = 0.05.

From the load-crack tip displacement measurements, it is clear that the transition from chevron notch to groove causes a jump in crack growth and cracking begins before peak load is reached. The final crack length, as determined by scanning electron microscopy of the cracked specimen, is 11.36 mm. For the Ti_2AlC sample considered here, finite element simulations of the wedge test using cohesive elements are conducted with varying parameters that include friction coefficient, fracture strength and fracture energy of the material. Young's modulus of the Ti_2AlC ceramic is well documented in the literature and a value of 260 GPa is used in the simulations. The friction coefficient is tuned to a value such that the initial slope of the load-displacement response from the simulations matches with the experiments and a value of 0.05 was obtained.

A range of fracture property values (strength and fracture energy) are considered as a set of parametric simulations, and the results are compared with the experimental load-wedge displacement curve and the crack area-wedge displacement curves. The crack area refers to the surface area of the crack created during the fracture process as determined by acoustic emission and assuming a linear relation between the transient integrated acoustic emission signal and the transient crack area (crack length x actual sample width at the crack tip position). The constant in this relation was determined from the final crack length of 11.36 mm and the total integrated acoustical signal up to the corresponding wedge displacement. It should be mentioned that experiments using long range optical microscopy and digital image capturing to track the crack tip position did not lead to the actual crack tip positions with enough accuracy. The simulations for a fracture strength of 200 MPa and a fracture energy equal to 1.5

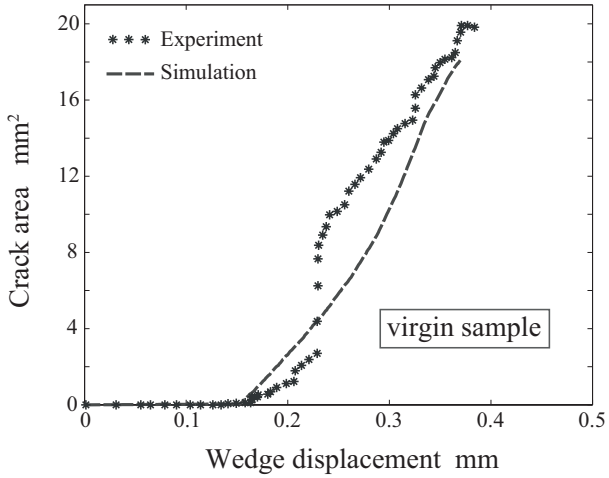

Figure 5.4: Evolution of crack growth. Comparison of crack area between experiment and simulation.

N/mm yielded an excellent agreement between experimental and computed behavior for both the load-displacement response and the crack area as shown in Fig. 5.3 and Fig. 5.4. It can be observed that the actual initiation of the crack is well captured in the simulation while the actual evolution of the crack area with increasing wedge displacement shows a slightly bigger deviation, but well within the expected variability of such a tough ceramic.

5.3.2. HEALING AND RE-FRACTURE OF HEALED SPECIMEN

Before going into the healing experiments and corresponding simulations, the definitions of healing efficiencies are established. Such a generic definition is particularly relevant as the self-healing community is yet to formulate test condition-independent protocols to quantify self healing behaviour. In this sense the situation is comparable to the early stages of the field of fracture mechanics in which the transition had to be made from simply documenting the failure load of a sample containing a specific crack under conditions of simple monotonic uniaxial loading to the current situation in which the failure load of a sample containing a crack of arbitrary dimension under a multi-axial load can be predicted with adequate accuracy using a simple scalar material property, the fracture toughness, and the far-field loading conditions. Two main recovery factors or efficiencies could be relevant to quantify the effect of healing. First, the change in peak load before and after healing of the fractured specimen, given by η_p in (5.1). And the second, the normalised change in the amount of energy that can be dissipated during fracture of the cracked specimen before and after healing, given by η_g in (5.2). These two factors given below, are utilized to arrive at quantification of property recovery from the resulting load-displacement response of virgin and healed samples.

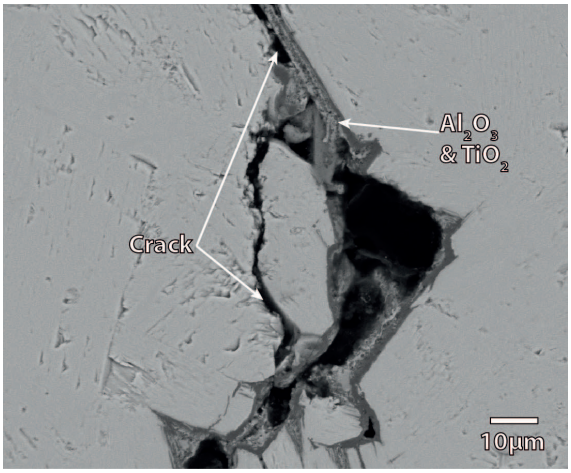

Figure 5.5: SEM backscattered electron image of cross-sectioned Ti_2AlC sample cracked 3 times with two intermediate healing treatments. The final induced crack runs through the TiO_2 and Al_2O_3 phases.

$$\eta_p = \frac{P_h - P_r}{P_o - P_r}, \tag{5.1}$$

$$\eta_g = \frac{G_h - G_r}{G_o - G_r}. \tag{5.2}$$

The subscripts h, r and o stand for healed, fractured and original sample, respectively.

The total testing protocol of the experiment reported here consisted of three cracking cycles with two intermediate healing cycles. Healing treatments were conducted in air at 1200°C for 2 hours. The oxidation treatments resulted in a total surface oxide scale of 350 µm. According to post-mortem sample investigations, complete oxidative crack filling was found for a crack length of approx. 4 mm, starting from the crack tip. Hence, the remaining approx. 7 mm of the crack at the onset of the third wedge-loading cycle were taken to be effectively unfilled. As known, Ti_2AlC heals micro cracks by formation of Al_2O_3 and minor amounts of TiO_2 [SPM+16, SPS+08, LSK+12]. The double oxidation treatment at 1200^oC for 2 hours of the Ti_2AlC sample considered here resulted in a mixture of both oxides. Rutile is present almost to the same extent as Al_2O_3. The oxidation treatment of the induced cracks resulted in a lower degree of crack gap filling than previously reported, [SPM+16] possibly due to a larger crack gap (±101.55µm), but the reason for the less than anticipated crack filling it not fully understood at this point. According to post-mortem cross-section analysis, cracks in the Ti_2AlC specimen propagated roughly along the same path during each loading. Consecutive cracks weave in and out of the oxides formed during the previous healing step, see Fig.5.5.

The experiment and simulation-based quantification of healing efficiency of Ti_2AlC require clear and reliable data on loading, wedge-displacement and crack length. During re-loading after a first oxidation treatment at 1200°C for 2 hours, technical difficulties rendered the results insufficient for a simulation-based evaluation. Specifically, the wedge displacement recording was deemed unrealistic (visual observation and recorded values did not coincide) and hence the recorded data were declared to be unreliable. Thus, the final recorded loading curve is presented, after two oxidation treatments at 1200°C at 2 hours and an intermediate loading experiment. The objective, to demonstrate self-healing quantification by means of experiments and a cohesive zone based finite element modeling is not impaired by use of the final load-displacement recording. The peak load of 160 N for the wedge-loaded Ti_2AlC specimen treated twice at 1200°C for 2 hours clearly exceeds the residual load of approx. 100 N of the virgin sample, see Fig. 5.6.

One of the key parameters that determines the healing efficiency is the extent to which the crack is filled and healed by the formation of well-adhering oxides. The healing product formed by oxidation of Ti_2AlC is assumed to be mainly alumina Al_2O_3, which is a strong but brittle material in relation to the original material, i.e. Ti_2AlC. In this context, the strength of the healing material is taken equal to 400 MPa and the fracture energy is assumed to be 0.1 N/mm as against the values 200 MPa and 1.5 N/mm for Ti_2AlC. To study the effect of crack filling, different ratios of the healed to total crack length, l_h/l_c are considered in the simulations. The resulting load-displacement responses for five different ratios are shown in Fig. 5.6. It is worth mentioning that the initial crack length, l_c , is the length of the crack after first cracking of the specimen and before any healing process is started.

One particular feature observed in the load-displacement response is the unloading path of the specimen, shown in Fig. 5.6. Such a behaviour is the effect of the friction between the wedge and the specimen. In other words, the area enclosed by the unloading-reloading curves (3, 4, 5, 6a) corresponds to the frictional dissipation. From an experimental data acquisition point of view, recording the unloading and the reloading paths would help in estimating the friction coefficient between the specimen and the wedge before and after healing. This, in turn, would help as inputs to the simulation and improve the predicting capability of the model, hence communicated to experimental collaborators for the next phases of testing.

From the results, it can be seen that with increasing ratio of the healed crack length to the initial crack length (prior to healing), the recovery of the load increases. To better visualize the recovery of the load carrying capability, the two efficiencies defined earlier are used. From the plots shown in Fig. 5.7, it can be observed that if the crack is completely healed as a result of the formation of high strength alumina, complete recovery of mechanical properties is obtained both in terms of strength and fracture energy, revealed through the data points corresponding to 100% efficiency. For cases in which partial healing is considered, the efficiencies decrease to lower values as shown in the figure. For instance, for a healed crack length ratio of 0.5, the strength and energy-based healing efficiencies are about 20% and 40% respectively. This indicates

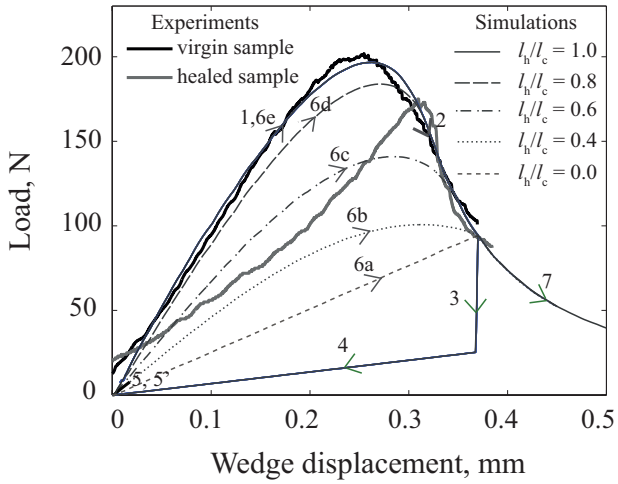

Figure 5.6: Load-displacement responses for varying ratios of healed length to total crack length. 1,2- loading (cracking); 3,4,5- unloading; 5,5'- healing phase; 5',6,7'- reloading post-healing

that strength recovery is more affected by the healed length ratio than the fracture energy recovery. It is to be noted that the strength and energy that are referred to, are ultimately related to the properties at specimen level rather than the material properties.

From the results shown in Fig. 5.6, the best match of simulation to experimental loading curve is found for a ratio between 0.6 and 0.8 of healed to original crack length. This approximately corresponds to a healing efficiency of up to 80% in terms of strength. As fracture energy is a measure of the area beneath the load-displacement curve, the best match ratio of $l_h/l_c = 0.6$ results in a healing efficiency of approximately 55% (Fig.5.7).

The experimentally resolved value of 0.4 for l_h/l_c does not match the amount of healing the model required in order to match the recorded load-displacement curve. The effect of TiO_2 formation within the crack, modifying the healing material properties, is neglected in the simulation approach. Finally, it should be stated that the path of the crack as observed experimentally is not explicitly modeled at the level of the actual microstructure in the healed crack. The incomplete healing and oxide mixture leads subsequent cracks to wind in and out of the scar zone, as shown in Fig. 5.5. The simulation cannot, at this point, capture the crack evolution through areas of incomplete oxide filling, but assumes full and ideal healing in oxidized areas. Further experimental testing along with detailed data acquisition would be valuable to test and further validate the modelling framework.

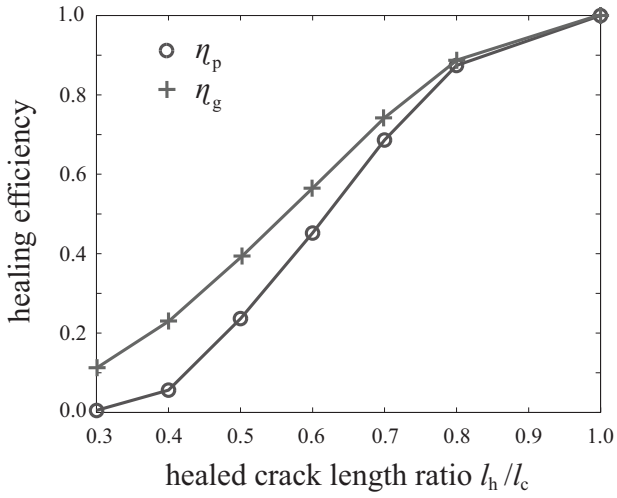

Figure 5.7: Healing efficiency with reference to recovered specimen strength η_p and fracture energy η_g.

5.4. SUMMARY AND OUTLOOK

The crack healing model developed in the previous chapter has been applied to analyse and quantify the fracture and load recovery characteristics of the intrinsic self-healing material, the MAX phase ceramic Ti_2AlC. The framework for the determination of healing efficiency in terms of strength and recovered energy using an integrated computational-experimental approach was to some degree successfully demonstrated for Ti_2AlC. It is shown that the model can be used to evaluate the healing efficiency of the self-healing material and correlate the effect of the amount of healed crack zones with efficiency through simulations. The modelling framework clearly is not yet predictive, but was able to capture the pre-healed response, or in other words, the response of the virgin material accurately. However, when it comes to the post-healed response, lack of detailed experimental data limits the validation process and hence the predictive capability of the model could not be demonstrated. Nonetheless, qualitative inferences have been made from the simulated results obtained using the healing model in terms of the healing mechanism and the healing efficiencies. The current cohesive-zone based crack healing model, when enriched with suitable healing kinetics, would yield better understanding and quantification of the healing efficiency in self-healing material systems.

6

ASSESSMENT OF CRACK DRIVING FORCE USING CONFIGURATIONAL FORCES

In chapter 2 which deals with the issue of crack-single particle interaction, multiple studies have been conducted to predict the crack *path* and hence the fracture mechanism as a function of mismatch in elastic and fracture properties between the particle and the matrix. On a different front in chapter 3, the effect of the mismatch in properties on the global mechanical properties of the particulate composite is studied. However, at a local level in the vicinity of the particles, the effect of their presence on the *crack driving force* is not quantified explicitly. It is the objective of this chapter to determine the driving force for different mismatches in the mechanical properties between the particle and the matrix. For this purpose, the concept of configurational forces is utilized and the eXtended Finite Element Method (XFEM) in Abaqus is employed as a tool to simulate crack propagation. Two broad aims are set and addressed in this chapter. Firstly, the configurational forces associated with the crack and the inhomogeneities (i.e. the particles) are quantified, which in turn yield the crack driving force at the crack tip and also the direction of the crack propagation. The second major aim of this chapter is to quantify the contribution of the particles to the crack driving force and the associated crack path in the *presence of the fracture process zone*. Such a study is very relevant to crack-particle interaction studies conducted using cohesive fracture mechanics framework. The study serves to allow an unbiased comparison between two different fracture mechanics approaches (classical and cohesive) for particulate systems.

6.1. INTRODUCTION

Methods based on Linear Elastic Fracture Mechanics (LEFM) have been extensively used to study the change in the crack tip driving force (usually expressed as the stress intensity factor or the energy release rate) in the presence of particles in an otherwise homogeneous medium [LK95, LC93, Bus97, KWHD02, KPTK06, AC06, WPT+07, LS94, NSK+99, AC07, NKMB14]. The key conclusion of those studies is that the crack driving force is amplified in the presence of a softer particle ahead of the crack tip and diminished if the particle is stiffer than the surrounding matrix material.

The above classical fracture mechanics approaches yield a singular stress field at the crack tip and the crack tip driving force is governed by a single parameter such as Stress Intensity Factors (SIF) or Strain Energy Release Rate (SERR) or J-integral [T.L05]. All these parameters directly or indirectly represent the amount of energy available at the crack tip for crack propagation. The crack is advanced if the driving force parameter exceeds a critical limit, usually a material parameter such as fracture toughness or critical energy release rate.

In a more generalized framework, the concept of configurational forces or material forces, introduced as an alternative to classical fracture mechanics, can be used as an effective tool to analyse fracture problems. Configurational forces may be interpreted as an energetically-conjugate system of forces associated with the motion of material points in the reference configuration, unlike the Newtonian forces which are associated with the deformation described by the motion of material points in the current deformed configuration. In other words, such forces result from changes in the reference configurations, which are due to processes such as fracture, phase transformation or plastic deformation [Gur00]. Phenomena like fracture alter the reference configuration as new surfaces are created and hence new material points are created in the reference configuration. Similar to the balance principles in classical mechanics, balance relations are postulated to relate changes in the reference configuration and the configurational forces. These relations serve as the basis for crack propagation studies [GPG98, GPG96]. The theory of configurational forces has been successfully applied to elasto-plastic fracture problems [NGKG05, SFS+08, ÖKLB14].

Simha *et al.* [SFK+05] extended the theory of configurational forces to account for the presence of smooth and discontinuous inhomogeneities in the material. The effect of the inhomogeneities on crack tip driving force is quantified for the case of a two-phase material with a sharp interface [KPF10]. Several other studies utilise configurational force approach to quantify the effect of interface (either a bimaterial planar interface or particle-matrix interface) [KBG02, KPS+05, CPF+07].

In this work, finite element analyses are carried out to quantify the effect of particles on crack driving force using the concept of configurational forces and utilising XFEM as a tool to model the crack topology. The crack driving force is evaluated numerically in a finite element simulation using the configurational force integrals. The implementation of this calculation is achieved through the user subroutine URDFIL in Abaqus, which provides access to the mechanical fields in

a simulation (stresses, strains and displacements) that are required to compute the crack driving force. Geometries with single and multiple particles are considered with different particle stiffnesses relative to that of the matrix as well as various particle offsets. After presenting this framework of crack modelling, the theory of configurational forces is extended to a cohesive zone fracture mechanics framework, whereby the effect of particles on the crack driving force is quantified in the presence of a cohesive or fracture process zone.

The key aspects addressed in this chapter are listed below:

- A general framework to analyse crack propagation in a particulate system is presented using the concept of configurational forces and employing XFEM as a tool. Multiple cases are considered for the analysis, whereby the effect of material (stiffness) and geometric properties (offset) of the particle(s) are quantified in terms of crack driving force and crack trajectory.

- The analysis using cohesive zone approach does not provide direct quantification of the effect of particles on the crack driving force, as the CZM approach does not involve parameters such as energy release rate or stress intensity factor to do so. Hence, given the goal of quantifying the particle effect in the presence of cohesive zone, configurational force-based energy integrals are utilized as a postprocessing tool with the results obtained using cohesive elements in a particulate system. Further, the influence of varying fracture process zone on the shielding effect of the particles is quantified. Such a study aims to provide insights on the differences between classical sharp tip fracture mechanics and cohesive zone fracture mechanics, for which the fracture process zone is the key parameter differentiating between the two approaches of fracture mechanics.

- The concept of quantifying the particle effect based on configurational forces is proposed for use in a cohesive zone-based XFEM in order to determine the direction of crack propagation. Using the configurational force-based energy integrals, a maximum energy dissipation-based criteria is proposed for the prediction of crack propagation direction within the cohesive zone-based XFEM framework. Most of the cohesive-XFEM techniques use the plane of maximum principal stress-based criterion for predicting the crack growth direction, which sometimes leads to spurious oscillations in crack path due to the numerical issues associated with XFEM-based crack tip stress fields. Further, the effect of fracture process zone on the crack trajectory is analysed and quantified, which is again relevant for a cohesive zone fracture mechanics approach. Finally, crack paths predicted by maximum principal stress criterion and maximum energy dissipation criterion are compared in the presence of varying fracture process zone lengths.

6.2. CONFIGURATIONAL FORCES FOR FRACTURE PROBLEMS IN INHOMOGENEOUS SYSTEMS

The concept of configurational forces for a heterogeneous material system presented in [SFK+05] is adopted in this work, in which the inhomogeneity is the particle, separated from the matrix by a sharp interface. The system of equations based on configurational forces in the presence of particles is discussed below.

Consider a two-dimensional body Γ which contains a sharp precrack and a pair of particles embedded in the matrix as shown in the Fig. 6.1. Considering small strain conditions, the configurational force at the crack tip is given by

$$\mathbf{f}_{\text{tip}} = -\lim_{q\to 0}\int_{\Gamma_{\text{tip}}} (\phi\mathbf{I} - \nabla\mathbf{u}^{\text{T}}\boldsymbol{\sigma})\hat{\mathbf{m}}\,\mathrm{d}l \tag{6.1}$$

where ϕ is the strain energy density, $\nabla\mathbf{u}$ is displacement gradient, $\boldsymbol{\sigma}$ is the stress tensor, Γ_{tip} is the contour of radius q surrounding the crack tip and $\hat{\mathbf{m}}$ is the unit normal to the contour considered. From thermodynamic considerations in terms of rate of dissipation of energy associated to the fracture process, the driving force for the propagation of the crack tip is identified as -$\mathbf{f}_{\text{tip}}$. It can be noticed that the configurational force at the tip, $\mathbf{f}_{\text{tip}}$, is the negative of the *J*- integral vector at the crack tip, $\mathbf{J}_{\text{tip}}$, where the terms inside the parenthesis represent the Eshelby's energy-momentum tensor [Esh75].

In the presence of the particle, the configurational force at the crack tip can be expressed as the sum of two components, schematically shown in Fig. 6.1. One component is from far field conditions specified on the boundary and the other component is due to the presence of the particle, which is induced by the mismatch in the material properties across the particle/matrix interface. Using the relation between the configurational force and the crack driving force ($\mathbf{J}_{\text{tip}}$= -$\mathbf{f}_{\text{tip}}$), the driving force at the crack tip can be expressed as

$$\mathbf{J}_{\text{tip}} = \mathbf{J}_{\text{far}} + \mathbf{C}_{\text{int}} \tag{6.2}$$

where $\mathbf{J}_{\text{far}}$ is the far field driving force and $\mathbf{C}_{\text{int}}$ represents the contribution due to the presence of the particle. The far field driving force vector is given by the line integral along the external boundary Γ_{far} with unit normal $\hat{\mathbf{s}}$ and the contribution from the crack faces with unit normal $\hat{\mathbf{p}}$ given by

$$\mathbf{J}_{\text{far}} = \int_{\Gamma_{\text{far}}} (\phi\mathbf{I} - \nabla\mathbf{u}^{\text{T}}\boldsymbol{\sigma})\hat{\mathbf{s}}\,\mathrm{d}l \tag{6.3}$$

The interface driving force, which measures the contribution due to the presence of the particle, is given by the integral along the particle-matrix interface Γ_{int} as

$$\mathbf{C}_{\text{int}} = -\int_{\Gamma_{\mathbf{int}}} (\llbracket\phi\rrbracket - \langle\boldsymbol{\sigma}\rangle\,\llbracket\boldsymbol{\varepsilon}\rrbracket)\,\hat{\mathbf{n}}\mathbf{d}\mathbf{l} \tag{6.4}$$

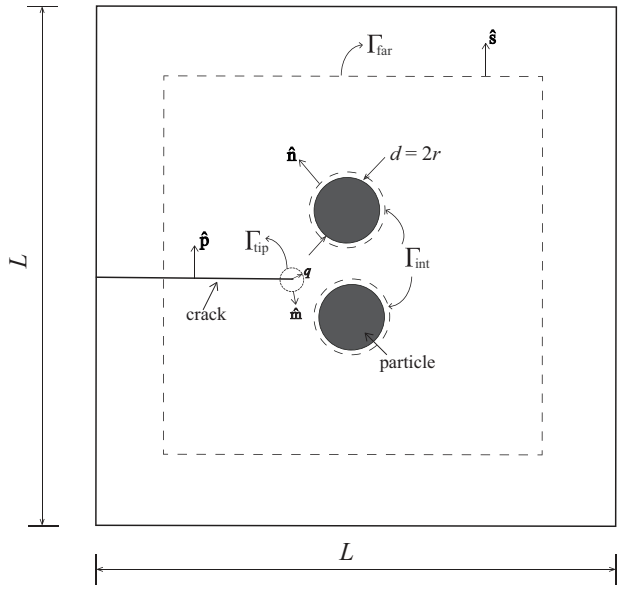

Figure 6.1: Schematic of the configurational forces associated with a material system containing a crack and inclusion(s).

where $\hat{\mathbf{n}}$ is the unit normal to the interface pointing away from the particle. The quantities $[\![\bullet]\!]$ and $\langle\bullet\rangle$ represent, respectively, the jump and the average of the fields across the particle/matrix interface.

The interface configurational force is also found to be related to the J-integral around the interface, i.e.,

$$\mathbf{C}_{\text{int}} = -\mathbf{J}_{\text{int}} = -\int_{\Gamma_{\text{int}}} (\phi\mathbf{I} - \nabla\mathbf{u}^{\text{T}}\boldsymbol{\sigma})\hat{\mathbf{n}}\text{d}\mathbf{l} \tag{6.5}$$

Using these relations, one can quantify the effect of the particle on the crack driving force, especially with the interface term $\mathbf{C}_{\text{int}}$. For a homogeneous system with a straight crack, the crack tip driving force reduces to the classical J-integral.

In addition, using the maximum energy dissipation criteria, the crack propagation direction can also be obtained from the above relations. The rate of energy dissipation due to the propagation of the crack tip is given by the product of the crack tip driving force and the crack tip velocity,

$$\text{E}_{\text{tip}} = \mathbf{J}_{\text{tip}}.\mathbf{v}_{\text{tip}}. \tag{6.6}$$

In accordance with the Clausius-Duhem inequality, the rate of energy dissipation due to cracking is greater than or equal to zero. From a modeling point of view, the fracture process requires a constitutive relation between the crack tip velocity and

the driving force (in terms of magnitude and orientation). The maximum energy dissipation criterion indicates that the direction of crack propagation will be the direction of the crack driving force vector $\mathbf{J}_{\text{tip}}$ itself. In other words, the rate of energy dissipation is maximized when the angle between the crack tip velocity and the crack driving force vector is equal to zero. In this work, the crack tip driving force is obtained as the sum of far-field J-integral vector, $\mathbf{J}_{\text{far}}$ and the interface integral vector $\mathbf{C}_{\text{int}}$.

6.3. EXTENDED FINITE ELEMENT METHOD FOR CRACK PROBLEMS

XFEM is a numerical technique to model discontinuities such as cracks and is an extension of the conventional continuous displacement-based finite element method. In XFEM, the presence of cracks is modeled by enriching the conventional bulk elements with additional displacement degrees of freedom to capture the crack openings [BB99, MDB99, MB02, FB10]. Within the context of XFEM, the use of the level set method or similar techniques makes it possible to model arbitrary crack growth without remeshing [SCMB01]. As a result, the FE mesh is not required to have the element boundaries aligned with the crack faces. Further, no explicit remeshing is required to accommodate the propagated crack geometry at every time step.

In Abaqus, XFEM is available for modelling crack problems using two different fracture mechanics approaches [ABA11]. One approach utilises classical fracture mechanics solutions (i.e., from LEFM) to enrich the crack tip and use virtual crack closure technique to simulate crack propagation. The second one relies on a surface-based cohesive zone model whereby a traction-separation relation governs the crack growth [RdBN08, MB02]. In this work, XFEM technique in Abaqus is merely used as a tool to represent crack geometry, while the crack driving force and the crack direction are separately determined using configurational forces as described in the previous section. Further, in Sec. 6.4, the crack growth is modelled using XFEM without the presence of a cohesive zone whereas, in Sec. 6.5 and Sec. 6.6, the XFEM approach is used to analyse the effect of the particle on the crack path in the presence of cohesive zone, i.e., within the cohesive zone fracture mechanics framework. In both cases, the crack driving forces and the crack propagation direction are evaluated using configurational forces.

6.4. QUANTIFICATION OF CRACK DRIVING FORCE WITHOUT COHESIVE ZONE

6.4.1. CRACK PROPAGATION IN A SYMMETRICALLY LOCATED PARTICLE-MATRIX SYSTEM

A two-dimensional rectangular domain of length L and height W is considered for the analysis, which contains a symmetrically located pair of particles of diameter $d = 2r$ each embedded in a matrix (see Fig. 6.1). The domain contains an initially straight edge crack of length a with its crack tip located at a horizontal distance b and vertical

distance c measured from the bottom edge of the particle, as shown in Fig. 6.2. The initial crack length is taken as $a = L/6$. The horizontal distance is chosen as $b = 7r$, which is sufficiently large such that the influence of the particle on the crack driving force is initially negligible, regardless of the vertical offset c (see [Bus97, KWHD02]). The following convention is used for the definition of the variable c in this chapter. For a single particle case, c refers to the separation between the edge of the particle and the initial crack plane, whereas for the case of a pair of particles or array, it refers to the vertical distance between the edges of the particles located above and below the initial crack plane. Plane strain deformation is assumed for all the simulations and linear elastic material properties are assumed for the bulk behaviour of both the particle and the matrix.

Traction boundary condition is specified on the top and the bottom edges of the 2-D domain. Crack propagation is assumed to occur under constant applied traction and the crack extension is chosen sufficiently small for a given time increment. The above assumptions suffice for the objective of the study which is to evaluate the effect of the particle and its properties on the crack driving force and the trajectory as the crack traverses through it. The user subroutine UDMGINI in Abaqus is utilised to control the length and direction of the crack extension. The configurational forces-based approach is employed in an explicit way to evaluate the crack driving force based on the deformation and stress fields of the previously converged time step. The direction of crack extension is then determined based on the maximum energy release rate hypothesis, which in this case, would be the direction of the crack driving force vector as discussed above in section Sec. 6.2.

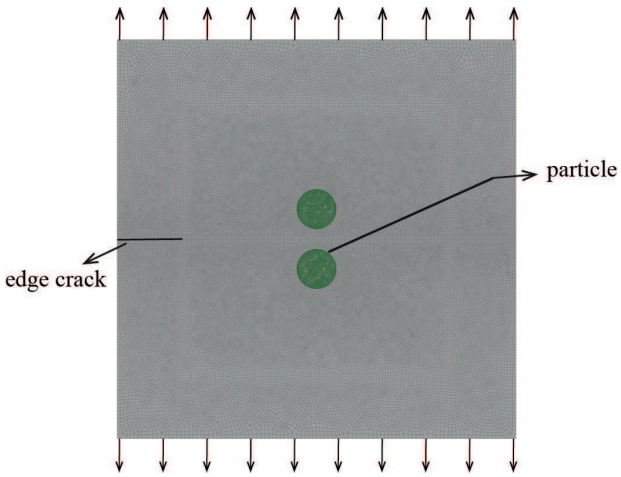

Figure 6.2: Two dimensional model of the crack-particle system considered for the analysis. Two particles are placed symmetrically to the initial crack line, separated by a distance, given by c. The initial crack tip is located at a distance, $b = 7r$.

VALIDATION OF THE APPROACH

To validate the present approach, a case reported in the literature [Bus97] is simulated. The test case for the validation considers the geometry and the boundary conditions described in 6.4.1, which is the same as used in [Bus97], where the inter-particle separation is given as $c = r$. The material properties of the particle and the matrix are kept the same as in the literature, which corresponds to the following: The Young's modulus of the matrix and the particle are given as $E^{\mathrm{m}} = 70$ GPa and $E^{\mathrm{p}} = 450$ GPa respectively, representative of a silicon carbide matrix dispersed with aluminium particles. The Poisson's ratio of the matrix and the particle are given by $\nu^{\mathrm{m}} = 0.33$ and $\nu^{\mathrm{p}} = 0.17$ respectively. The resulting variation of the energy release rate is plotted in Fig. 6.3a along with the result reported in the pertinent literature. It can be observed that the results obtained in the current simulation match very well with the literature results.

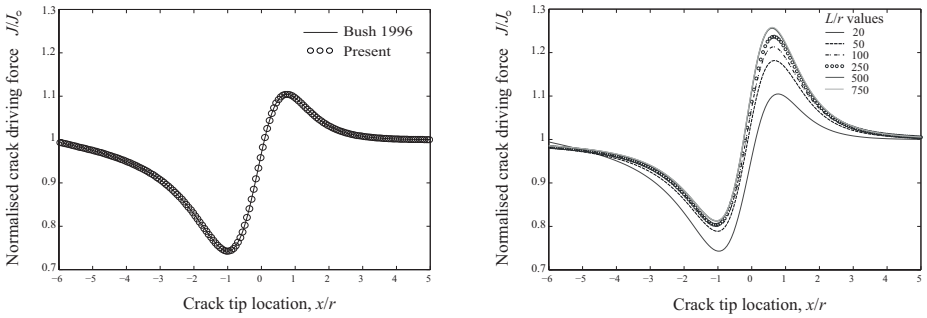

(a) Comparison with literature result.

(b) Effect of domain size.

Figure 6.3: Validation result and the convergence of crack driving force with size of the domain w.r.t the particle size. The result corresponds to a 2D domain with a embedded pair of particles separated by $c = r$ as shown in Fig. 6.2. The following material properties are used: $(E^{\mathrm{p}}/E^{\mathrm{m}} = 6.43$, $\nu^{\mathrm{p}} = 0.17$ and $\nu^{\mathrm{m}} = 0.33$. For the validation result (a), the domain size ratio taken is given by $L/r = 20$; in (b), the domain size ratio is varied from $L/r = 20$ to $L/r = 750$.

It is important to address the effect of the boundary conditions and the domain size on the crack driving force. In order to capture only the effect of the particle on the driving force, a large domain of length L relative to the size r of the particle must be used, i.e., the ratio L/r should be sufficiently large. In the literature studies reported in [Bus97, KWHD02, KPTK06, WPT+07, NKMB14], the authors used a domain size ratio, $L/r = 20$ and traction boundary conditions are used. In [Bus97], it was indicated that the ratio $L/r = 20$ results in a converged solution, in other words, increasing the domain size further w.r.t particle size would presumably not influence the crack driving force. Correspondingly, shielding and antishielding effects predicted in Fig. 6.3a should be purely ascribed to the presence of the particle and not influenced by the boundary effects. To ascertain this claim, simulations are conducted to explore the effect of domain size and the results are plotted in Fig. 6.3b. The plot shows the variation of crack driving force in the considered particulate system normalised with

corresponding crack driving force values obtained for various crack tip locations in a homogenous matrix. From the results, it can be observed that the domain considered in the literature is not sufficiently large to exclude the boundary effects, thus the boundary conditions still have an effect on crack driving force predictions.

From the results on the effect of domain size, as shown in Fig. 6.3b, it can be concluded that a domain size ratio of at least $L/r = 500$ should be used to minimize the influence of the boundary conditions on the crack driving force. Further, it can be observed that a smaller domain size ratio overpredicts the shielding effect that occurs when the crack tip is, in general, ahead of the particle centre and largely underpredicts the antishielding effect that occurs when the crack tip traverses across the particle. Thus, to analyse solely the effect of the particle on the crack driving force, the size of the domain is henceforth fixed at $L/r = 500$.

QUANTIFICATION OF SHIELDING EFFECTS

In this section, the effect of the modulus mismatch on the crack driving force is evaluated through a parametric analysis. Unless mentioned differently, for all the simulations, the Young's modulus of the matrix is taken as $E^{\mathrm{m}} = 150$ GPa. The Young's modulus of the particle, E^{p} is varied, resulting in various mismatch ratios $E^{\mathrm{p}}/E^{\mathrm{m}}$ to study the mismatch effect. The Poisson's ratios of the particle and the matrix, ν^{p} and ν^{m}, are kept constant with $\nu^{\mathrm{p}} = \nu^{\mathrm{m}} = 0.25$.

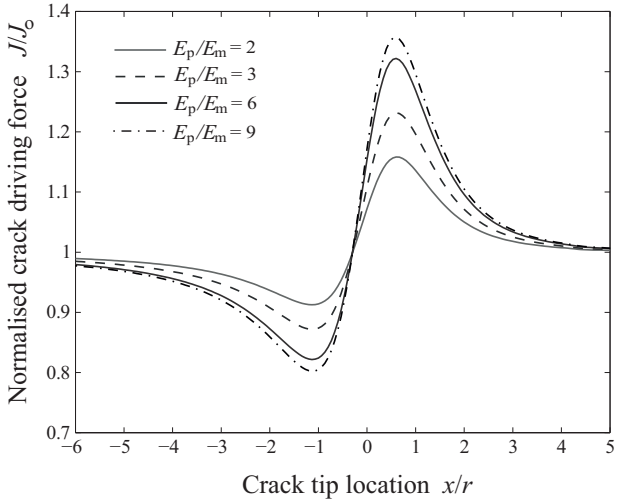

Figure 6.4: Effect of stiffness mismatch on crack driving force.

The following four different modulus mismatch ratios, $E^{\mathrm{p}}/E^{\mathrm{m}} = 2, 3, 6$ and 9 are analyzed. The results of the normalized crack driving force for the above ratios are reported in Fig. 6.4. It can be clearly observed from the results that a stiffer particle, in general, shields the approaching crack by reducing the crack driving force. It can be observed that the shielding effect starts at a distance equal to $5r$ from the centre

of the particle. As the crack approaches the particle, the shielding effect reaches its maximum for the crack tip located at a distance equal to the particle radius from the centre of the particle. Upon further traversing of the crack tip, the driving force increases. When the crack tip crosses the centre of the particle, the normalized crack driving force increases above the value of one. This indicates an anti-shielding effect as the crack tip moves from the stiffer to the softer regime. The shielding or the anti-shielding effect increases with increasing particle stiffness. However, it attains a saturation, whereby an increase in the stiffness of the particle beyond a certain value has only a minimal influence on the crack driving force.

6.4.2. CRACK PROPAGATION IN THE PRESENCE OF AN ASYMMETRICALLY LOCATED PARTICLE

The above set of simulations clearly established that the mismatch in elastic modulus significantly alters the crack driving force magnitude and hence the fracture behaviour of particulate systems. Nonetheless, the crack path remains straight despite the modulus mismatch, which is expected because of the symmetric location of the particles with respect to the initial crack plane. Hence, in the following section, a single particle-matrix system is considered with the objective of simulating a curved crack path resulting from the shielding effects of the particle. Different offsets of the particle w.r.t the initial crack plane are considered and the results are reported in terms of the crack driving force and the crack path.

DIFFERENT PARTICLE OFFSET

For this study, a similar set up as shown in Fig. 6.2 is considered except that only one particle is embedded within the matrix material and the size of the domain is fixed at $L/r = 500$. To create the asymmetry in the crack-particle-matrix system, different offsets are introduced between the initial crack path and the centre of the particle. The offsets considered in the study are given by $c = r/2, r$ and $2r$, where c here refers to the vertical distance between the edge of the particle and the initial crack plane. The stiffness mismatch ratio given by $E^{\mathrm{p}}/E^{\mathrm{m}} = 6$ is considered for the analysis.

Fig. 6.5a shows the variation of the normalised crack driving force as the crack traverses through the matrix. As with the previous set of studies, it can be observed that, as the crack approaches the particle, the crack driving force is diminished because of the shielding effect caused by the presence of the stiffer particle ahead of the crack tip. More importantly, the crack driving force vector changes its orientation as it approaches the particle. As explained before, the direction of the crack propagation may be determined according to the maximum energy release rate criterion that indicates that the direction of the crack propagation lies along the direction of the crack driving force vector. In the simulations reported in the previous section, the crack path remained straight (in the horizontal direction) due to symmetry. In the simulations reported in this section, the interface integral around the interface of the particle at an offset results in a non-zero inhomogeneity term in the direction normal to the incoming crack, leading to a deflected crack path upon further growth.

The resulting crack path is shown in Fig. 6.5b. It can be seen from the figure that, when the offset between the particle and the initial crack plane is increased, the effect of the particle is less pronounced and so is the change in the magnitude and direction of the crack driving force. Another observation is that though the crack felt the presence of the particle at a horizontal distance equal to 5 times the radius of the particle (shown by the change in the driving force), the crack deflection occurs only when the crack tip reaches a distance equal to the radius of the particle. It can be safely argued that the toughening effect of the stiff particle is a combination of the shielding effect and the crack path traversed due to the deflection induced. Further, it can be observed from Fig.6.5a that once the crack passes further down the particle, an amplification of the driving force occurs, similar to the results reported in the previous straight path cases. From the crack paths reported in Fig.6.5b, the deflection created by the particle is not significant especially when the offset becomes larger, though the crack driving force is altered by a noticeable amount.

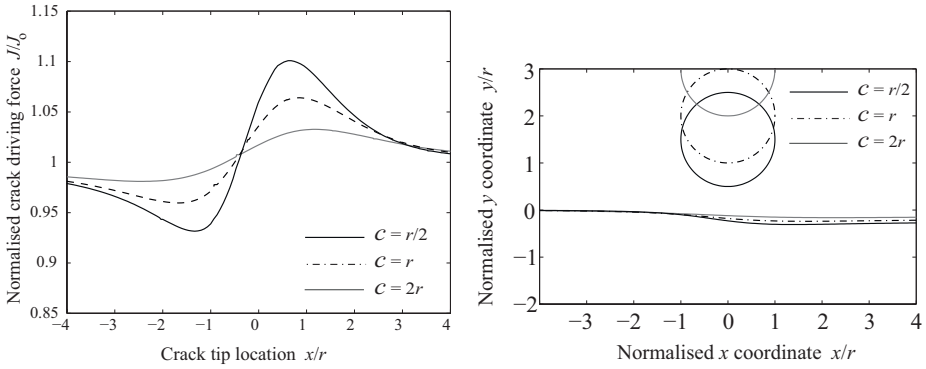

(a) Crack driving force for various offsets.

(b) Crack path for various offsets.

Figure 6.5: Effect of particle offset on crack driving force and crack path. Modulus mismatch ratio, $E^{\mathrm{p}}/E^{\mathrm{m}} = 6$ is used.

6

EFFECT OF STIFFNESS MISMATCH

In the second parametric study, the offset of the particle is fixed at a value given by $c = r/2$ and the stiffness of the particle is increased relative to the stiffness of the particle. The considered stiffness mismatch values are given as $E^{\mathrm{p}}/E^{\mathrm{m}} = 2, 3, 6$ and 9. The resulting variations in the crack driving force and the crack path are reported in the Fig.6.6a and Fig.6.6b. From the Fig.6.6a, one can observe the expected increase in the change in the driving force as the stiffness mismatch increases. The crack paths corresponding to the stiffness mismatch values are shown in figure Fig. 6.6b. With an increase in stiffness of the particle, there is an increase in the deflection of the crack away from the particle, however, the amount of deflection does not increase

proportionally with the stiffness mismatch. In fact, comparing the two different mismatch ratios, $E^{\mathrm{p}}/E^{\mathrm{m}} = 6$ and 9, there is little change in the crack path. In other words, the change in the crack driving force and the crack path does not get affected when the stiffness mismatch is increased further beyond a certain level.

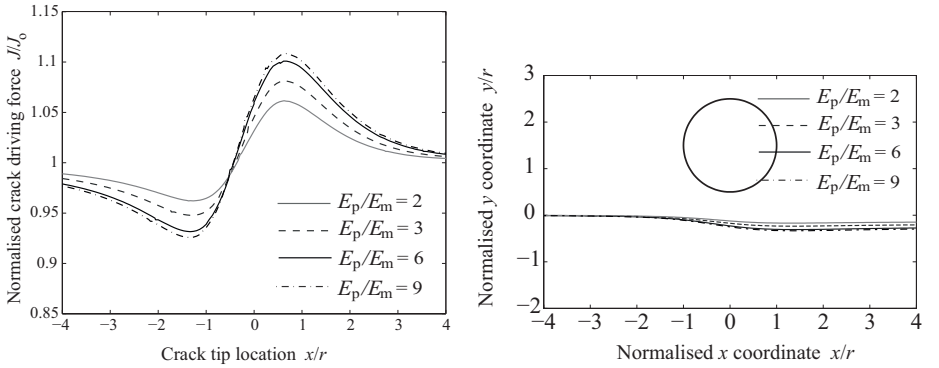

(a) Crack driving force.

(b) Deflected crack path.

Figure 6.6: Effect of particle stiffness on crack driving force and crack path. The particle offset used is given by $c = r/2$.

6.4.3. CRACK PROPAGATION THROUGH AN ARRAY OF PARTICLES

In all previous cases, either a single particle or a pair of symmetrically located particles were considered to address the dependence of the crack driving force and the crack path on the stiffness mismatch. It is more realistic to consider an array of particles for the crack propagation studies, where interactions between a crack and multiple particles and between the different particles on the stress distributions exist. In this context, two different configurations are considered, each of which is explained in the sections below.

6

SYMMETRIC ARRAY OF EIGHT PARTICLES

In this set of study, crack propagation studies are carried out with an array of eight particles located, four above and four below, with respect to the initial crack plane. The result of interest in this study is the change in crack driving force and not the crack path, which is trivial in the case considered because of the symmetry. Two different parameters, namely the inter-particle distance between the top and bottom array of particles and the stiffness mismatch, are altered to study their effect on the crack driving force.

EFFECT OF PARTICLE OFFSET OR SEPARATION

Four different particle offsets are considered, given by $c = r/2, r, 2r$ and $4r$. The vertical distance between the initial crack plane and the top array of particles and that of the

bottom array of particles are kept the same. The horizontal edge to edge distance between the particles is assigned a distance equal to twice the radius of the particle. A stiffness mismatch of $E^{\mathrm{p}}/E^{\mathrm{m}} = 6$ is assumed for all particles and simulations. The results of the change in the crack driving force are reported in the figure Fig. 6.7a. As a general and an expected observation, with an increase in the particle separation, the effect that it has on the crack driving force decreases, which is also observed in the case of a pair of symmetrically located particles studies in the earlier section. A distinguishing observation in the multiple particle case is that, as the crack traverses through each pair of particles, the driving force curve tend to shift towards the positive y-axis direction. In other words, the shielding and antishielding peaks in each section of the curve (corresponding to each pair) shifts above. This indicates that the crack tip is now influenced by a cluster of particles rather than just a pair of particles located near the current crack tip. When the crack tip is at a location, $x/r = -1$, it is influenced by eight stiffer particles ahead of it, whereas, for a crack tip at a location, $x/r = 3$, it is affected by two pairs of particles ahead and two behind. In the former scenario, the crack tip is shielded by four pairs of particles. In the latter case, the crack tip is shielded by two pairs of particles ahead and antishielded by two pairs of stiffer particles behind the crack tip. In addition, when the crack tip crosses the first pair of particles, it experiences both shielding effect by the remaining three pair of particles ahead of it and antishielding effect by the pair of particles behind the crack tip. Naturally, the negative and the positive peaks in the normalised crack driving force keeps decreasing and increasing respectively as the crack tip encounters a lesser number of particles as it traverses through the array. Hence, the crack tip at different locations experiences different combinations of shielding and antishielding effects as can easily be observed from the results.

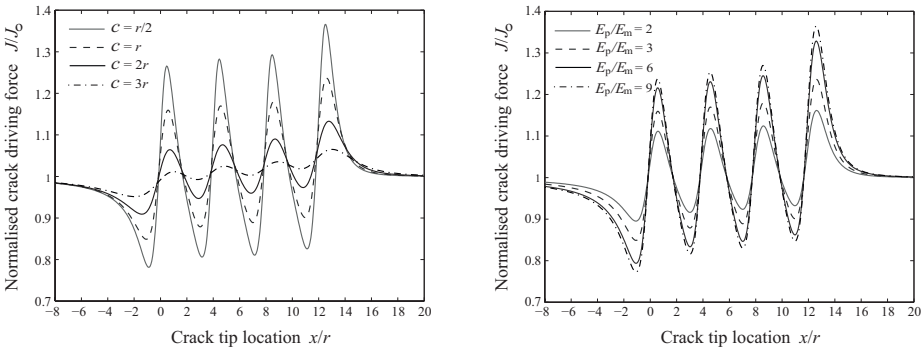

(a) Effect of particle separation. Modulus ratio, $E^{\mathrm{p}}/E^{\mathrm{m}} = 6$ is used for the simulations.

(b) Effect of particle stiffness. Particle offset, c= r/2 is used.

Figure 6.7: Effect of symmetrically located particle array on crack driving force.

EFFECT OF STIFFNESS MISMATCH

In this case, the particle separation distance is fixed at $c = r/2$ and the effect of stiffness mismatch is studied. The particles are assumed to be stiffer than that of the matrix and four different mismatch ratios are considered given by $E^{\mathrm{p}}/E^{\mathrm{m}} = 2, 3, 6$ and 9. The corresponding results of the crack driving force for various crack tip locations are shown in Fig.6.7b. From the figure, a similar trend in the variation of the crack driving force with respect to the crack tip location is observed as compared with the results corresponding to the particle separation. In other words, increase in stiffness match is equivalent to the decrease in the particle separation. As with the results reported earlier for particle offset (or separation) case, it can be observed that the negative and positive peaks shift upwards towards the positive y-axis.

ASYMMETRIC ARRAY OF FOUR PARTICLES

In the previous case, a symmetric array of eight particles is considered, resulting in a trivially straight crack path. In this subsection, an array of four particles located asymmetrically with respect to the initial crack plane is considered. The resulting deflecting crack path with corresponding variations in crack driving force is reported. Again, two different parameters are varied, namely the stiffness mismatch ratio and the particle separation.

EFFECT OF PARTICLE SEPARATION

As with the symmetrically located case, four different values for the particle separation, $c = r/2, r, 2r$ and $4r$, are considered. The value of stiffness mismatch is fixed with the value $E^{\mathrm{p}}/E^{\mathrm{m}} = 6$. The results of the simulations are summarized in Fig. 6.8. From the plot of crack driving force as the function of crack tip location, it can be observed that the effect of decreasing particle separation is reflected through the increase in the shielding and antishielding effects. An interesting feature can be seen, when the present case is compared with the case of symmetrically located particles, refer Fig.6.7a. In the case of symmetric array, the positive and negative peaks in the crack driving force kept shifting upwards, whereas in the present case, such a monotonic shifting behaviour is not observed. The crack driving force vector changes its direction because of the asymmetry and hence a change in the crack propagation direction is resulted, as seen in Fig. 6.8b. The pattern of the variation in crack driving force as a function of crack tip location is explained as follows. Once the crack tip felt the presence of the first particle ahead of it, due to the offset/asymmetry, the crack deflects away from it due to the higher stiffness of the particle. Because of this deflection, when it reaches the proximity of the second particle, it is now closer to the particle than in the case when it approached the first particle. This results in a higher shielding effect naturally when it traverses the second particle. In a nutshell, the effect that the particle has on the crack driving force could be very different in different scenarios. It depends on the arrangement and distribution of the particles, which ultimately reveals that the particle distribution may have a direct influence on toughness enhancement of particulate composite systems. In this context, a relevant and a detailed study dealing with controlling the effective toughness by engineering the particulate microstructure

can be found in [SON17]. It should be pointed out that in real life 3D materials filled with discrete particles, the effect of the topological distribution of the reinforcing particles may be less outspoken than in the 2D simulation presented here.

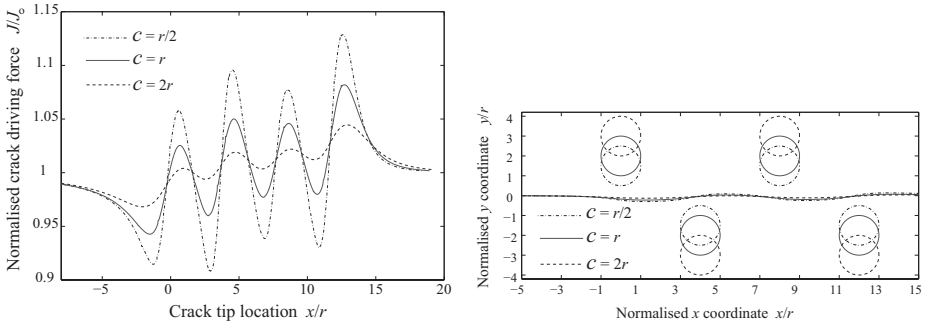

(a) Variation of crack driving force. (b) Crack path traversing through particle array.

Figure 6.8: Effect of asymmetrically located particle array on crack driving force and crack path, for various particle separations.

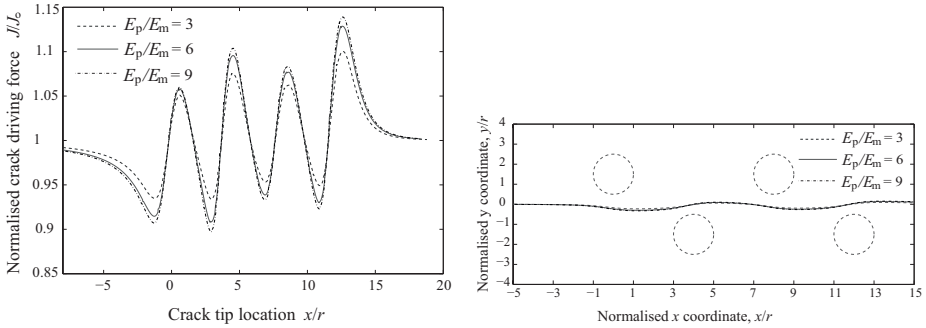

(a) Variation of crack driving force. (b) Crack path traversing through particle array.

Figure 6.9: Effect of asymmetrically located particle array on crack driving force and crack path, for various stiffness mismatch ratios.

EFFECT OF STIFFNESS MISMATCH

In this set of analyses, the particle separation is fixed with $c = r/2$ and the stiffness mismatch ratio is altered by considering three different values, $E^p/E^m = 3, 6$ and 9. The results of the variation of crack driving force and the associated crack paths for different stiffness mismatch ratios are reported in Fig.6.9. As expected, the trend is not

altered when compared with the previous study on the effect of particle separation, refer Fig. 6.8. In other words, increasing the particle separation has a similar effect as decreasing the stiffness of the particle with respect to the matrix, though one-to-one correspondence is not established between particle separation and stiffness mismatch ratio. Upon observing the Fig. 6.9b, the crack path becomes more torturous with increase in stiffness mismatch ratio. It can be logically extrapolated that such a torturous path leads to additional energy dissipation in a realistic microstructure, thus contributing to fracture toughness of the composite.

6.5. QUANTIFICATION OF CRACK DRIVING FORCE WITH COHESIVE ZONE

In the previous sections, the variations of the crack driving force and the crack path as a function of geometric and material properties are analysed using configurational forces approach and XFEM. It is to be noted that in all those above studies, no cohesive or fracture process zone is considered, thus leading to modelling based on classical sharp crack tip fracture mechanics. In other words, for the configurations considered, the results of the crack driving force would correspond to linear elastic fracture mechanics solutions, see for instance Fig. 6.3a. If cohesive zone fracture mechanics is applied to the particulate system, as discussed before, it introduces a nonlinear cohesive zone ahead of the actual crack tip, quantified by the length scale parameter $\bar{l}^{\mathrm{m}}_{\mathrm{fpz}}$ defined in (2.8), whereby the LEFM stress fields are no longer present. Such an approach is utilised in the previous chapters for studying the interaction between the crack and the particle(s). When the cohesive zone approach is utilised for fracture analysis, it is not straightforward to quantify the effect of particles on the crack driving force. This is primarily because, unlike classical fracture mechanics (linear elastic or elastoplastic), CZM-based fracture mechanics does not require crack driving force parameters such as energy release rate or stress intensity factor. Rather, the modelling framework invokes a constitutive relation in the cohesive zone which implicitly contains the crack driving force and the crack propagation kinetics.

Thus, it is important to analyze the effect of this distinct length scale feature inherent to cohesive fracture mechanics and to determine how the crack driving force in a particulate system is influenced as compared to classical fracture mechanics-based results. Studies exist in the literature on the comparison between cohesive zone and classical fracture mechanics approaches [Wan10, JS06, Rab08, Abe16, CM10, PT06], some of which highlight the conditions under which the cohesive fracture mechanics coincides with classical fracture mechanics. One of the conclusions is that when the process zone is very small, the solutions obtained from cohesive fracture mechanics should coincide with classical fracture mechanics. This is expected as the singular crack tip stress fields can be recovered when the process zone length tends to zero. However, the effect of the length scale parameter is not addressed before in the context of crack-particle interactions in the literature. The effect of process zone length on fracture in particulate composite system deserves a particular

attention especially to reveal the toughening characteristics of particle reinforcement in materials with varying fracture process zone lengths. It is therefore the objective of this section to quantify the effect of the particle on the crack propagation characteristics in the presence of a cohesive or process zone. It is important to emphasize that in this section the driving force based on the configurational force is not required to conduct the simulations because the crack propagation analysis in CZM does not require such parameters. For comparison purposes, the simulations in this section are conducted for the same configurations used in above sections using a bilinear traction-separation relation in conjunction with cohesive elements or XFEM-cohesive segments approach. The results of the stresses, strains and deformation fields obtained from the cohesive zone analysis are utilised to evaluate the effect of particles on the crack driving force by using the configurational force approach only as a post-processing tool to facilitate the comparative analysis.

With the introduction of the cohesive zone, the singular stress fields are replaced. Consequently, in the presence of cohesive zone, the framework of the configurational forces has to be revisited. Effectively, the crack driving force is governed by the initiation and growth of the cohesive zone, which in turn is governed by a traction-separation relation. The configurational force at the crack tip becomes the configurational force integral around the cohesive zone as shown in Fig.6.10.

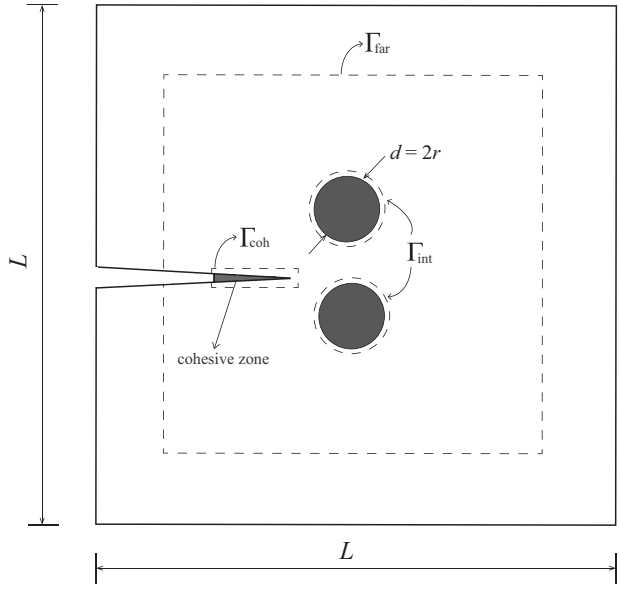

Figure 6.10: Configurational forces in the presence of cohesive zone. To show the cohesive zone, the crack is shown in its opened/deformed state.

The driving force associated with the cohesive zone-based crack can be expressed as

$$\mathbf{J}_{\text{coh}} = \mathbf{J}_{\text{far}} + \mathbf{C}_{\text{int}} \tag{6.7}$$

where $\mathbf{J}_{\text{far}}$ is the far field driving force and $\mathbf{C}_{\text{int}}$ represents the contribution due to the presence of the particle.

For a fully developed crack, such an integral is equal to the cohesive fracture energy, i.e, the area under the traction-separation curve. From the converged equilibrium solutions in a finite element analysis involving cohesive elements, the integral around the cohesive zone is equal to the sum of the far-field J integral and the inhomogeneity term associated with the presence of the particles. It is worth mentioning that, this integral is always constant once the cohesive zone is fully developed and the evolution of the cohesive crack zone is self-similar. Thus, the effect of the particle on crack growth can be quantified by using the ratio of the inhomogeneity/interface integral to the integral around the cohesive zone. The different integral paths are summarised in Fig. 6.10.

6.5.1. EFFECT OF FRACTURE PROCESS ZONE ON CRACK KINETICS

In this section, the configuration containing a pair of symmetrically located particles is considered, see Fig. 6.2. Symmetry is maintained which allows us to focus on the effect of the fracture process zone on the driving forces in the presence of the particles, without concerning about the crack trajectory. The Young's modulus of the matrix is taken as $E^{\text{m}} = 150$ GPa and a stiffness mismatch ratio given by $E^{\text{p}}/E^{\text{m}} = 3$ is considered. The offset between the initial crack line and the centre of the particle is given by $c = r/4$. To study the effect of the particle in the presence of cohesive zone, the fracture process zone length is varied over a range by assigning various values for the cohesive strengths of both the particle and the matrix. The fracture energy is kept constant and equal to 0.1 N/mm. Various values are given to the local cohesive strength value in the model, such as 200, 300, 400, 500, 700, 1000 MPa, which correspond to the process zone length scales, $\bar{l}^{\text{m}}_{\text{fpz}} = 25$, 11, 6.25, 4, 2 and 1 respectively, obtained using (2.8). It is emphasized that increasing the cohesive strength, by keeping all other parameters constant results in a reduction in the length of the fracture process zone as it is proportional to the square of the strength, see (2.1). A similar reduction in the fracture process zone can be achieved by reducing the fracture energy, which in principle results in a more brittle-like fracture behaviour. The parameter of interest here is the effect of the size of the fracture process zone in relation to the size of the particle, as defined by $\bar{l}^{\text{m}}_{\text{fpz}}$.

The results of the analysis are summarised in Fig. 6.11. The plot shows the variation of the inhomogeneity integral term associated with the particle normalised with the cohesive fracture energy (J-integral around the cohesive zone) as the crack propagates, for various cohesive strengths (or fracture process zone lengths). From the figure, a striking feature that can be observed is that the variation of the configurational force associated with the particle changes when the fracture process zone length is changed.

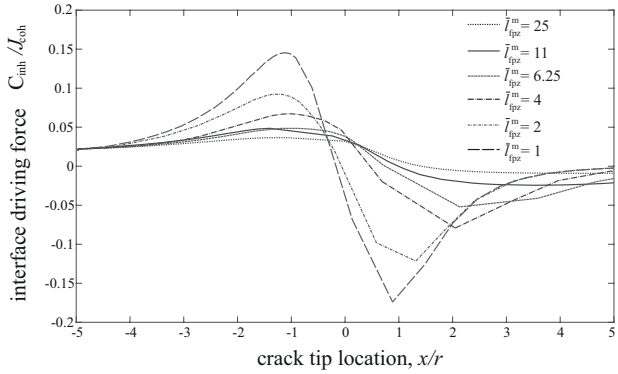

Figure 6.11: Effect of fracture process zone length on crack driving force. A pair of symmetrically located particles w.r.t the initial crack direction is considered for the analysis.

This is the direct effect of the inherent length scale parameter associated with cohesive zone fracture mechanics. Upon closer observation, the influence of the presence of the particle increases (in terms of the driving force contribution) with the reduction in the fracture process zone. Such an observation provides an insight that the shielding effects of the particles are not constant if the cohesive zone is introduced, which is not the case in the classical fracture mechanics approach. It can be observed that the contribution of the particle to the crack driving force decreases as the fracture process zone length increases. For instance, for the length scale parameter given by $\bar{l}^{m}_{fpz}$ =25, the contribution of the particle to the crack driving force becomes negligible as seen from the figure. On the other hand, for $\bar{l}^{m}_{fpz}$ =1, the influence of the particle is the highest among the different cases considered. In particular, the positive peak occurs when the crack approaches the particle and is located at a distance equal to a radius of the particle from its centre. The positive peak corresponds to a normalised value of 0.15 reflecting the shielding effect of the particle because of its higher stiffness relative to the particle. This would mean that for a crack to propagate a unit length (unit area in 3D), 15 percent additional energy (when compared to a homogenous matrix case) is required to be dissipated in order to overcome the shielding effect of the particle when the crack is ahead of the particle. On the other hand, a negative peak would mean an antishielding effect attributed to the transition of the crack tip from stiffer to softer region. From the above results, it can be established that for a very large process zone length, the presence of a stiffness mismatched particle becomes insignificant and does not influence the crack kinetics.

The following interpretation can be done to understand such an effect of the fracture process zone on the crack driving force in the presence of the particles. When the fracture process zone length is larger, the particles are effectively embedded in the diffused crack zone, which in turn reduces its influence on the change in the crack driving force. This aspect can be further explained in Fig.6.12 which shows the stress fields in the presence of a cohesive crack tip ahead of the particles for varying fracture

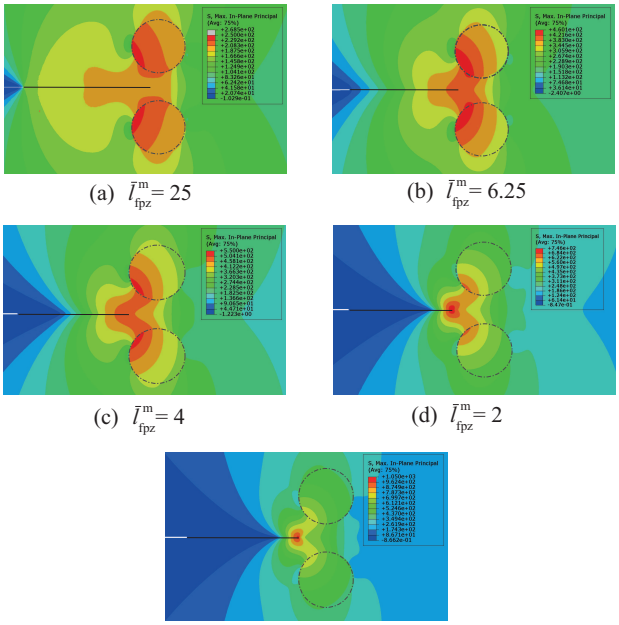

(a) $\bar{l}^{m}_{fpz} = 25$ (b) $\bar{l}^{m}_{fpz} = 6.25$

(c) $\bar{l}^{m}_{fpz} = 4$ (d) $\bar{l}^{m}_{fpz} = 2$

(e) $\bar{l}^{m}_{fpz} = 1$

Figure 6.12: Cohesive crack tip stress fields for varying fracture process zone lengths.

process zone lengths. From the stress fields shown in the figure, it can be interpreted that the 'strength' of the crack tip is gradually reduced with increase in the fracture process zone length. In physical terms, the influence of the cohesive crack tip on the particle is weaker (or the vice versa) as the process zone increases in size w.r.t the particle size. Another way of interpretation on the effect of process zone can be given as follows: with a larger process zone, the extension of the cohesive crack tip is governed majorly by the cohesive strength parameter, leaving the cohesive fracture energy insignificant for the crack extension. In other words, the extension of a cohesive crack tip by a unit length in the presence of large process zone requires very less energy to be dissipated, as compared with a crack tip extension in the presence of a smaller process zone. This is reflected in the results on the energy contributions of the particle to the crack extension as shown in Fig. 6.11. A similar observation is made in chapter Sec. 2, whereby the strength is the determining factor for larger cohesive zone lengths and fracture energy is the dominant factor for smaller process zones in deciding the fracture mechanism.

Thus, it can be concluded that the shielding and antishielding characteristics of the inclusions in a matrix is significantly influenced by the fracture process zone. If the length of the zone reduces, in other words, for a brittle-like behaviour, the effect of the particle is more pronounced. The obtained solution would coincide with classical fracture mechanics-based singular stress field if the length of the fracture process zone

becomes or tends to zero. Ultimately, the length scale parameter becomes one of the determining factors in crack-particle interactions. The effect needs to be considered during analysing toughening mechanisms in heterogeneous materials, especially if the material's process zone length is large and more importantly if the inclusions in the material are smaller w.r.t the process zone length.

6.6. CRACK PATH PREDICTION IN THE PRESENCE OF COHESIVE ZONE

In the previous section, the effect of fracture process zone on the particle shielding/antishielding effects is quantified. In this section, the configurational forces are used to calculate the crack propagation direction and hence the crack paths in a cohesive zone fracture mechanics-XFEM framework. It is worth emphasizing that, in section 1, the crack driving force and the crack path are analysed using configurational forces and XFEM without the presence of cohesive zone, hence the results presented therein corresponds to linear elastic fracture mechanics-based solutions. The objectives in this section are to propose a criterion based on maximum energy dissipation for cohesive XFEM problem and further to analyse the crack path as a function of process zone length. Finally, the results are compared with crack paths obtained using maximum principal stress criterion, within the context of cohesive XFEM.

Invoking the maximum energy dissipation criterion, the direction of crack propagation at each step can be obtained as the following.

$$\theta_c = \tan^{-1}\left(\frac{J^2_{coh}}{J^1_{coh}}\right) \tag{6.8}$$

In the above equation, J^1_{coh} and J^2_{coh} are the components of the crack driving force integral along horizontal and vertical directions respectively. For the crack propagation direction, the user subroutine UDMGINI in ABAQUS XFEM capability is utilised and the crack propagation direction is provided as input to ABAQUS.

6.6.1. CRACK PATH FOR VARYING FRACTURE PROCESS ZONE LENGTHS

The two-dimensional domain, shown in Fig. 6.2 is used for the analysis, but with a single particle embedded in the matrix at an offset equal to half the radius of the particle. The elastic properties of the matrix and the particle are kept the same as used in section Sec. 6.5. The fracture energy of the matrix and the particle are kept the same and equal to 0.1 N/mm. The strength of the matrix and the particle are varied together over a range in order to achieve various process zone lengths. Four different strengths are considered, given by 200, 500, 700 and 1000 MPa. This results in fracture process zone length scales quantified by the ratio, $\bar{l}^m_{fpz}$ = 25, 4, 2 and 1 respectively. The simulations are conducted in Abaqus using quadratic stress criterion for crack initiation and a linear cohesive damage law is used for the damage evolution. The crack propagation direction is fed as input to ABAQUS through the subroutine UDMGINI for each increment in the analysis. The results of the simulated crack path

and the associated crack driving forces are presented in Fig. 6.13 and Fig. 6.14. For conciseness, the results corresponding to selected length scale values are shown in the figures.

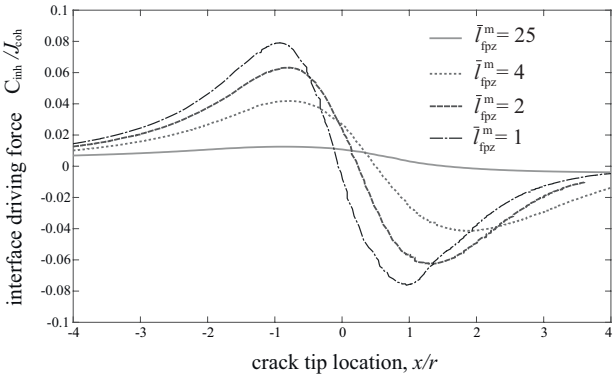

Figure 6.13: Effect of fracture process zone length on crack driving force for a particle with an offset.

The variation of the interface driving force during crack propagation for the above set of simulations is shown in Fig.6.13, whereas the resulting crack paths are shown in Fig.6.14. The results of the crack paths and the variations in driving force contribution from the particle have a one-to-one correspondence. In other words, the crack paths are the outcomes resulting from the variations in the crack driving force contribution associated with the particle. From the Fig.6.13, it can be inferred that, as the process zone length decreases, the influence of the particle increases, an observation similar to the symmetric particles case reported in section Sec.6.5.1.

An interesting observation from the resulted crack paths (see Fig. 6.14) is that, despite the stiffness mismatch ratio is kept the same for all reported simulations, the crack path is distinctly different for varying process zone lengths. In particular, if the process zone length is very large, the change in the crack trajectory is very small or even negligible. On the hand, if the fracture process zone length becomes small, the deflection in the crack path is more and more pronounced as observed from the figure. For instance, the crack path corresponding to the case, $\bar{l}^{m}_{fpz}$ = 25 is almost straight, emphasizing a negligible influence of the particle on the resulting crack path. This is similar to the case observed in the previous section, whereby the change in crack driving force associated with the particle is close to zero if the fracture process zone length is very large as compared to the size of the particle. For the case of $\bar{l}^{m}_{fpz}$ = 1, a relatively significant deflection of the crack path away from the particle is observed, see Fig. 6.14. In this case, the initially straight crack remains almost straight until it reaches a distance equal to one radius from the centre of the particle, after which the deflection in the path is observed as determined by maximum energy dissipation criterion. For very low fracture process zone length scales, the crack path observed is similar to the one observed in the literature, where linear elastic fracture mechanics-

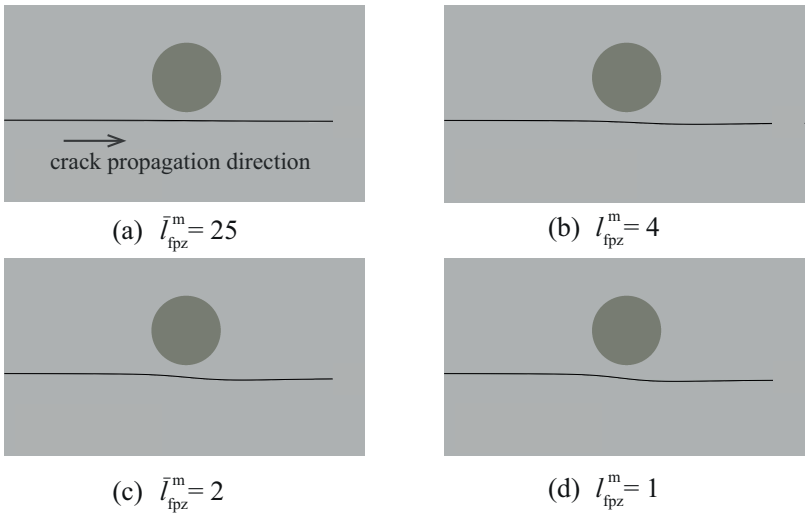

Figure 6.14: Effect of varying fracture process zone length on crack path. Same stiffness mismatch, $E^{p}/E^{m} = 3$ of the particle w.r.t the matrix is considered for all the four simulations.

based approach is used for crack path studies in combination with maximum energy dissipation-based criterion for crack propagation direction prediction. This implies, that as the fracture process zone length becomes negligible, the results of the crack driving force and the crack path would coincide with the LEFM results.

Thus, the above observation is distinctly different from the results reported in the literature using classical fracture mechanics-based approaches. The length scale associated with cohesive zone approach has a significant influence in determining the effect of the particle on the crack driving force and the resulting crack path.

6.6.2. COMPARISON BETWEEN TWO CRACK PROPAGATION CRITERIA FOR CRACK DIRECTION

Having studied the effect of process zone length, in this section, two different criteria for predicting the crack propagation are used and the resulting crack paths are compared against each other. One of the criteria is based on maximum dissipation as used in the previous subsection and the other is based on the direction of maximum principal stress plane, a commonly used criterion in cohesive-XFEM [MKS05, WS01, MP03]. For this study, the single particle-matrix system considered above is used and analysis is conducted using Abaqus cohesive XFEM. Two sets of simulations are conducted, one set with a fracture process zone length scale given by $\bar{l}^{m}_{fpz} = 25$ and the other with the length scale given by $\bar{l}^{m}_{fpz} = 1$.

The results of the first set of simulations using the two different criteria are shown in Fig. 6.15 a and b, that corresponds to the larger fracture process zone length. From the results, it is evident that the two criteria predict totally different paths for the same

material system. The maximum energy dissipation-based criterion predicts more or less a straight path. In contrast, the maximum principal stress-based criterion results in a significant crack deflection away from the particle. This implies that a stress-based direction criterion results in a deflected path even when the fracture process zone is very large, for which the influence of the particle is negligible if one observes the variation of the energy-based crack driving force contribution from the particle, see Fig.6.11 and Fig.6.13.

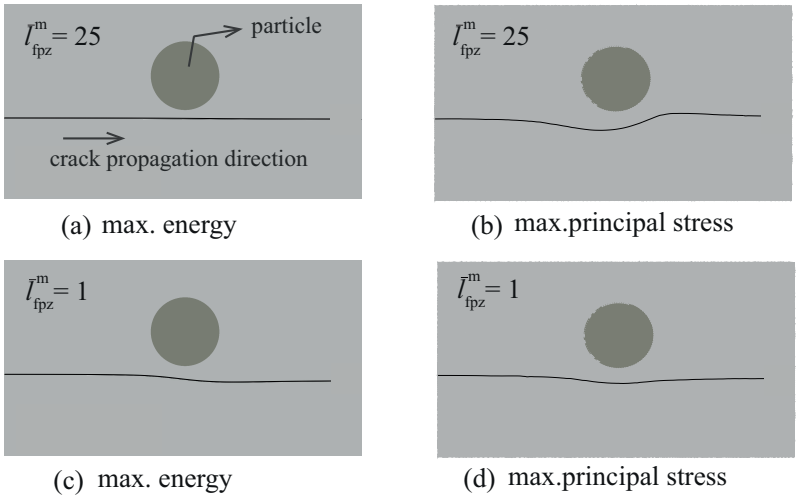

Figure 6.15: Effect of crack propagation direction criterion on resulting crack path for two different process zone lengths. For all the four crack paths, stiffness mismatch ratio of the particle w.r.t the matrix is the same and given by $E^{p}/E^{m} = 3$.

The outcome of the second set of simulations with a very small fracture process zone length, given by $\bar{l}^{m}_{fpz} = 1$, is shown in Fig. 6.15 c and d. This time, the maximum dissipation-based criterion predicts a significantly deflected crack path, an expected result from previous observations in Fig. 6.14 when the fracture process zone length is small. Another interesting feature is that, for the smaller fracture process zone length, both the criteria tend to predict similar crack paths when compared with the crack paths reported for larger process zone length. Upon comparing the crack paths for larger and smaller process zones using maximum principal stress-based criterion (b and d), the deflection in the crack path is less severe in the latter case. Upon further comparison between the two criteria from Fig. 6.15, in general, the initially straight crack starts to deflect away from the particle at a distance when the crack tip is approximately (atleast) two radii away from the centre of the particle. On the other hand, in the energy dissipation criteria, the crack starts to get deflected only when it reaches the edge of the particle, i.e., at a distance equal to one radius of the particle from its centre. Further, once the crack deflects away from the particle and propagates further, an upward deflection is observed in the crack path resulting

from principal stress-based criterion, whereas in the energy dissipation criterion, such an upward deflection is not observed. In general, it can be concluded that in particulate composites, the choice of crack propagation criterion is important in predicting fracture mechanisms using cohesive zone fracture mechanics.

6.7. SUMMARY AND CONCLUSIONS

The concept of configurational forces has been used to evaluate the crack driving force in an elastically homogeneous matrix containing one or more particles having a higher stiffness. While the chapters 2 and 3 aimed at quantifying the effect of particles on crack path and mechanical properties of the composite, the current chapter quantified locally the change in the crack driving force in the presence of a particle or an array of particles with and without the presence of fracture process zone. In the first section, crack propagation through the symmetric and asymmetric array of particles were analysed using the concept of configurational forces and XFEM and the results in terms of variation of crack driving force and crack paths were reported. In the second section, the effect of process zone length in determining the contribution of the particles to crack driving force is analysed using cohesive elements and configurational forces, followed by addressing the effect of fracture process zone length on the crack path using XFEM and configurational forces. This important analysis highlights the differences between the two entirely different fracture mechanics approaches, namely the classical fracture mechanics and the cohesive zone fracture mechanics. Finally, a comparison between different crack propagation direction criteria was discussed with varying fracture process zone lengths. The following major conclusions and insights were drawn from the analyses.

- The well-established shielding and antishielding effects of particles addressed using LEFM principles are revisited and studied using the concept of configurational forces and XFEM. It was shown that the established size of the domain w.r.t particle size for convergence of crack driving force is not sufficient, and to quantify the effect of particles without the influence of the boundary, a domain size of at least $L/r = 500$ is found to be required instead of $L/r = 20$ as reported in the literature.

- While the particle/matrix stiffness ratio is a major factor in influencing the crack driving force, it is shown that the arrangement of particles can be an important feature in determining the shielding or antishielding effect of the particles and hence the effective toughness of a particle reinforced system.

- The process zone length significantly influences the contribution of the particle to the crack driving force. In particular, a cohesive crack with larger fracture process zone length does not feel the presence of the particle ahead of the cohesive crack tip. On the other hand, in case of a smaller process zone, the influence of the particle on the crack driving force is much more pronounced. With a very small process zone length w.r.t the particle size, the crack driving

force contribution from the particle tends to coincide with values predicted by classical fracture mechanics-based approaches.

- The crack path is also significantly affected by the fracture process zone length. Lesser the process zone length w.r.t the particle size, larger is the deflection in the crack trajectory. For the same stiffness mismatch ratio, largely different crack trajectories are observed depending on the length of the fracture process zone. For a stiffness mismatch of 3 (stiffer particle), the crack path is almost straight if the process zone is large, an observation distinctly different from classical fracture mechanics based approaches. This suggests that the process zone is an important parameter in determining the effective toughness of a particulate composite, especially that involves cohesive ductile-like fracture instead of brittle fracture.

- The choice of criterion for the direction of crack propagation severely influences the resulting crack path. Using the maximum energy dissipation criterion for crack direction, no or little crack deflection is observed for larger process zone lengths, whereas significant deflection is observed for smaller process zone lengths. On the other hand, the criteria for crack propagation based on maximum principal stress predicts a deflected path irrespective of the length of the fracture process zone, however, severe deflection is observed for larger process zone case. For smaller process zone length, both the criteria tend to predict a similar crack path in relation to the larger process zone case.

7

APPENDIX

7.1. STUDY ON MESH DEPENDENCY

In the quasi-static computational approach adopted in the simulations conducted in chapters 2 and 3, the cohesive elements are embedded within the edges of the solid elements (see Fig. 2.5). Correspondingly, a crack can only move along cohesive elements and the issue of mesh dependency becomes relevant. In this case, the evolution of a crack path is not associated to a kinetic law (e.g., orientation for maximum dissipation criterion), but, instead, it is naturally chosen from the cohesive elements that "break" first according to their orientation and the local stress field. To mitigate the effect of mesh dependency, a fine random mesh is generated, which allows for a good resolution of the cohesive zone (see, e.g., [MCDH98]) and, equally important, a relatively arbitrary crack propagation. In practice, the crack path direction is chosen from an equilibrium path, which means that an effective kinetic law emerges from the simulations.

An overview of mesh-dependency effects with the use of cohesive elements can be found in [SR09, RRK12]. In order to quantify the mitigating effects of a refined, random mesh in the present analysis, a mesh refinement analysis has been carried out for a fixed particle offset of $c = 3d/4$, considering two different cases. In the first case, the particle and the matrix are assumed to have the same elastic and fracture properties. Consequently, in accordance with the maximum dissipation criterion for a homogeneous linearly elastic matrix, a straight crack path is expected as a solution under remote mode I loading. Five different mesh densities are considered in the analysis and the resulting crack paths are shown in Fig. 7.1a. The characteristic element length l_e, normalized with the fracture process zone length l^m_{fpz}, is used as the parameter representing the mesh density. The finest mesh used in the analysis contains 447 522 nodes and 372 824 elements, of which 223 650 are cohesive elements. In the second case analyzed, the elastic properties are kept equal, but the fracture strength of the particle is reduced by a factor of two relative to the matrix. In this case,

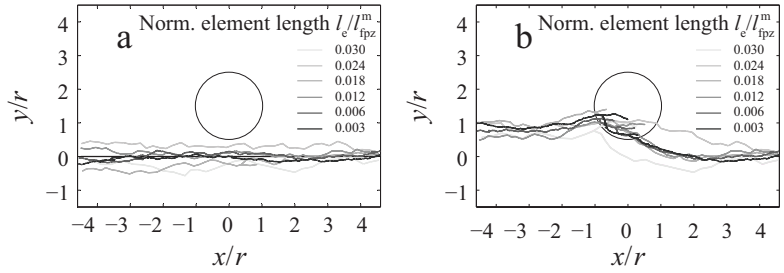

Figure 7.1: Mesh convergence studies for (a) a straight crack path (homogeneous system) and (b) a deflected crack path (weaker particle). Crack path is from right to left.

a deflected crack path is observed, where a secondary microcrack initiates within the weaker particle and coalesces with the approaching primary crack (see Fig. 7.1b).

In both cases, crack path convergence can be achieved by having a sufficiently fine mesh. For the first case, the crack paths converge to one that fluctuates about the straight path. The fluctuations are inherent to the fact that the crack is constrained to propagate only along element boundaries. In the second case, it is important to have a refined mesh for crack path convergence, since crack coalescence is only observed inside the particle once the mesh is sufficiently fine.

To further verify the convergence, the first case (straight path) is analyzed in more detail. Figure 7.2 shows the differences in the crack paths corresponding to the case shown in Fig. 7.1a. The error is obtained by taking an L_2 norm of the difference between the computed and the straight crack. The norm is proportional to the gray area shown schematically in the inset in Fig. 7.2 and is computed in the region of interest shown in the figures (i.e., $-4 \leq x/r \leq 4$), using all the completely failed cohesive elements. It can be observed that the error over the crack path decreases with an increase in mesh density. This trend confirms that the magnitude of the fluctuations of the crack path around the straight path, decreases.

A related parameter that is relevant for monitoring convergence is the total crack length. Although the magnitude of the fluctuations decreases, it is in general not possible to converge to the length of a straight crack unless the mesh is artificially aligned with the anticipated crack path. However, it was found that the simulated crack length is longer than the ideal straight crack length by only about 4% to 8% in the different mesh densities considered (crack length is calculated by summing up the length of the completely failed cohesive elements). This range of values does not correlate with the mesh density since it is mostly related to a geometrical characteristic of the elements, namely the angle between two edges. Indeed, as can be schematically seen in the inset in Fig. 7.2, the error in the length scales with the cosine of the average angle between the straight crack and the fluctuating crack, which is typically between 15° and 25° in the simulations.

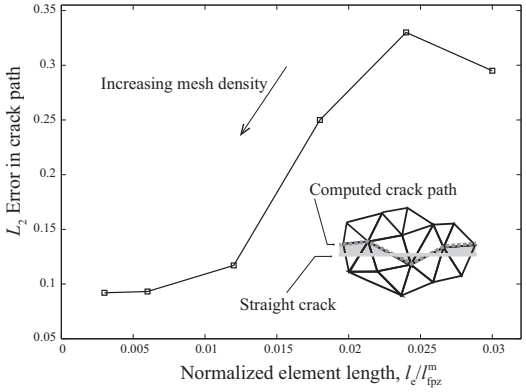

Figure 7.2: Error in crack path convergence.

As indicated above, mesh dependency with the use of cohesive elements can be significantly mitigated through the use of a sufficiently fine mesh. However, increasing the mesh density not only increases the computational costs, but also it induces an artificial compliance to the system due to the presence of an initial linearly elastic region in the cohesive law. Ideally, the problem of the artificial compliance can be nullified if an initially rigid cohesive law is used. In the present analysis, the rigid behavior is approximated using a sufficiently large stiffness in the cohesive law. Correspondingly, the overall approach adopted here mimics the properties of the XFEM. More importantly, it provides a robust alternative for handling crack coalescence, an issue that still remains elusive within XFEM.

REFERENCES

[AA15] Ammar A. Alsheghri and Rashid K. Abu Al-Rub. Thermodynamic-based cohesive zone healing model for self-healing materials. *Mechanics Research Communications*, 70:102–113, 2015.

[ABA11] ABAQUS. version 6.14 documentation. *Dassault Systemes Simulia Corp., Providence, RI, USA*, 2011.

[Abe16] R. Abedi. A comparative and parametric study of dynamic cohesive and linear elastic fracture mechanics models. *International Journal of Solids and Structures*, 102-103:163–175, 2016.

[AC06] A. Ayyar and N. Chawla. Microstructure-based modeling of crack growth in particle reinforced composites. *Composites Science and Technology*, 66(13):1980–1994, 2006.

[AC07] A. Ayyar and N. Chawla. Microstructure-based modeling of the influence of particle spatial distribution and fracture on crack growth in particle-reinforced composites. *Acta Materialia*, 55(18):6064–6073, 2007.

[ARM97] J W Adams, R Ruh, and K S Mazdiyasni. Young's Modulus, Flexural Strength, and Fracture of Yttria-Stabilized Zirconia versus Temperature. *J. Am. Ceram. Soc.*, 80(4):903–908, 1997.

[Atk72] C. Atkinson. The interaction between a crack and an inclusion. *International Journal of Engineering Science*, 10(2):127–136, 1972.

[Bar62] G.I. Barenblatt. The Mathematical Theory of Equilibrium Cracks in Brittle Fracture. *Advances in Applied Mechanics*, 7:55–129, 1962.

[BB99] T. Belytschko and T. Black. Elastic crack growth in finite elements with minimal remeshing. *International Journal for Numerical Methods in Engineering*, 45(5):601–620, 1999.

[BGB06] D. S. Burton, X. Gao, and L. C. Brinson. Finite element simulation of a self-healing shape memory alloy composite. *Mechanics of Materials*, 38(5-6):525–537, 2006.

[BGL05] Ever J. Barbero, Fabrizio Greco, and Paolo Lonetti. Continuum Damage-Healing Mechanics with application to self-healing composites. *International Journal of Damage Mechanics*, 14(1):51–81, 2005.

[BKO+10] B.J. Blaiszik, S.L.B. Kramer, S.C. Olugebefola, J.S. Moore, N.R. Sottos, and S.R. White. Self-Healing Polymers and Composites. *Annual Review of Materials Research*, 40(1):179–211, 2010.

[Bro11] E. N. Brown. Use of the tapered double-cantilever beam geometry for fracture toughness measurements and its application to the quantification of self-healing. *Journal of Strain Analysis for Engineering Design*, 46(3):167–186, 2011.

[BSS15] J. Bluhm, S. Specht, and J. Schröder. Modeling of self-healing effects in polymeric composites. *Archive of Applied Mechanics*, 85(9-10):1469–1481, 2015.

[BSW02] Eric N. Brown, Nancy R. Sottos, and Scott R. White. Fracture testing of a self-healing polymer composite. *Experimental Mechanics*, 42(4):372–379, 2002.

[Bus97] M.B. Bush. The Interaction between a Crack and a Particle Cluster. *International Journal of Fracture*, 88(3):215–232, 1997.

[BW08] Sheba D. Bergman and Fred Wudl. Mendable polymers. *J. Mater. Chem.*, 18(1):41–62, 2008.

[Cla03] David R. Clarke. Materials selections guidelines for low thermal conductivity thermal barrier coatings. *Surface and Coatings Technology*, 163-164:67–74, 2003.

[CM10] Chang Rong Chen and Yiu Wing Mai. Comparison of cohesive zone model and linear elastic fracture mechanics for a mode I crack near a compliant/stiff interface. *Engineering Fracture Mechanics*, 77(17):3408–3417, 2010.

[CMM+06] V. Cannillo, T. Manfredini, M. Montorsi, C. Siligardi, and A. Sola. Microstructure-based modelling and experimental investigation of crack propagation in glass-alumina functionally graded materials. *Journal of the European Ceramic Society*, 26(15):3067–3073, 2006.

[CNS89] T. Christman, A. Needleman, and S. Suresh. An experimental and numerical study of deformation in metal-ceramic composites. *Acta Metallurgica*, 37(11):3029–3050, 1989.

[CPCT06] Pietro Cornetti, Nicola Pugno, Alberto Carpinteri, and David Taylor. Finite fracture mechanics: A coupled stress and energy failure criterion. *Engineering Fracture Mechanics*, 73(14):2021–2033, 2006.

[CPF+07] C. R. Chen, J. Pascual, F. D. Fischer, O. Kolednik, and R. Danzer. Prediction of the fracture toughness of a ceramic multilayer composite - Modeling and experiments. *Acta Materialia*, 55(2):409–421, 2007.

[CSS03] Alfred Cornec, Ingo Scheider, and Karl Heinz Schwalbe. On the practical application of the cohesive model. *Engineering Fracture Mechanics*, 70(14):1963–1987, 2003.

[CSVdB10] M. V. Cid Alfaro, A. S.J. Suiker, C. V. Verhoosel, and R. de Borst. Numerical homogenization of cracking processes in thin fibre-epoxy layers. *European Journal of Mechanics, A/Solids*, 29(2):119–131, 2010.

[CvS15] Alexandra L. Carabat, Sybrand van der Zwaag, and Willem G. Sloof. Creating a Protective Shell for Reactive MoSi2 Particles in High-Temperature Ceramics. *Journal of the American Ceramic Society*, 98(8):2609–2616, 2015.

[DAL12] Masoud K. Darabi, Rashid K. Abu Al-Rub, and Dallas N. Little. A continuum damage mechanics framework for modeling micro-damage healing. *International Journal of Solids and Structures*, 49(3-4):492–513, 2012.

[Dry94] Carolyn Dry. Matrix cracking repair and filling using active and passive modes for smart timed release of chemicals from fibers into cement matrices. *Smart Materials and Structures*, 3(2):118–123, 1994.

[Dug60] D.S. Dugdale. Yielding of steel sheets containing slits. *Journal of the Mechanics and Physics of Solids*, 8(2):100–104, 1960.

[EG75] F. Erdogan and G. D. Gupta. The inclusion problem with a crack crossing the boundary. *International Journal of Fracture*, 11(1):13–27, 1975.

[EGGP01] M. Elices, G. V. Guinea, J. Gómez, and J. Planas. The cohesive zone model: Advantages, limitations and challenges. *Engineering Fracture Mechanics*, 69(2):137–163, 2001.

[EGR74] F. Erdogan, G.D. Gupta, and M. Ratwani. Interaction Between a Circular Inclusion and an Arbitrarily Oriented. *Journal of Applied Mechanics*, 41(4):1007–1013, 1974.

[EMH+01] A. G. Evans, D. R. Mumm, J. W. Hutchinson, G. H. Meier, and F. S. Pettit. Mechanisms controlling the durability of thermal barrier coatings. *Progress in Materials Science*, 46(5):505–553, 2001.

[Esh75] J. D. Eshelby. The elastic energy-momentum tensor. *Journal of Elasticity*, 5(3-4):321–335, 1975.

[FB10] Thomas Peter Fries and Ted Belytschko. The extended/generalized finite element method: An overview of the method and its applications. *International Journal for Numerical Methods in Engineering*, 84(3):253–304, 2010.

[FFLM08] Shao-Yun Fu, Xi-Qiao Feng, Bernd Lauke, and Yiu-Wing Mai. Effects of particle size, particle/matrix interface adhesion and particle loading on mechanical properties of particulate–polymer composites. *Composites Part B: Engineering*, 39(6):933–961, 2008.

[FKC14] Liberato Ferrara, Visar Krelani, and Maddalena Carsana. A "fracture testing" based approach to assess crack healing of concrete with and without crystalline admixtures. *Construction and Building Materials*, 68:535–551, 2014.

[FKT+18] A. S. Farle, J. Krishnasamy, S. Turteltaub, C. Kwakernaak, S. van der Zwaag, and W. G. Sloof. Determination of fracture strength and fracture energy of (metallo-) ceramics by a wedge loading methodology and corresponding cohesive zone-based finite element analysis. *Engineering Fracture Mechanics*, Accepted, 2018.

[GB98] Philippe H. Geubelle and Jeffrey S. Baylor. Impact-induced delamination of composites: A 2D simulation. *Composites Part B: Engineering*, 29(5):589–602, 1998.

[GGP17] F. A. Gilabert, D. Garoz, and W. Van Paepegem. Macro- and micro-modeling of crack propagation in encapsulation-based self-healing materials: Application of XFEM and cohesive surface techniques. *Materials and Design*, 130:459–478, 2017.

[GLPCC07] L Granger, A Loukili, G Pijaudier-Cabot, and G Chanvillard. Experimental characterization of the self healing of cracks in an ultra high performance cementitious material: mechanical tests and acoustic emission analysis. *Cement and Concrete Research*, 37(4):519–527, 2007.

[GPG96] Morton E. Gurtin and Paolo Podio-Guidugli. Configurational forces and the basic laws for crack propagation. *Journal of the Mechanics and Physics of Solids*, 44(6):905–927, 1996.

[GPG98] Morton E. Gurtin and Paolo Podio-Guidugli. Configurational forces and a constitutive theory for crack propagation that allows for kinking and curving. *Journal of the Mechanics and Physics of Solids*, 46(8):1343–1378, 1998.

[Gur00] Morton E Gurtin. *Configurational Forces as Basic Concepts of Continuum Physics*, volume 137 of *Applied Mathematical Sciences*. Springer New York, New York, NY, 2000.

[GVT+17] F. A. Gilabert, K. Van Tittelboom, E. Tsangouri, D. Van Hemelrijck, N. De Belie, and W. Van Paepegem. Determination of strength and debonding energy of a glass-concrete interface for encapsulation-based self-healing concrete. *Cement and Concrete Composites*, 79:76–93, 2017.

[HL08] Olaf Herbst and Stefan Luding. Modeling particulate self-healing materials and application to uni-axial compression. *International Journal of Fracture*, 154(1-2):87–103, 2008.

[HST09] T. S. Hille, A. S J Suiker, and S. Turteltaub. Microcrack nucleation in thermal barrier coating systems. *Engineering Fracture Mechanics*, 76(6):813–825, 2009.

[HWS94] Jody N. Hall, J. Wayne Jones, and Anil K. Sachdev. Particle size, volume fraction and matrix strength effects on fatigue behavior and particle fracture in 2124 aluminum-SiCpcomposites. *Materials Science and Engineering A*, 183(1-2):69–80, 1994.

[JD10] A. S. Jones and Haimanti Dutta. Fatigue life modeling of self-healing polymer systems. *Mechanics of Materials*, 42(4):481–490, 2010.

[JS06] Z. H. Jin and C. T. Sun. A comparison of cohesive zone modeling and classical fracture mechanics based on near tip stress field. *International Journal of Solids and Structures*, 43(5):1047–1060, 2006.

[KBG02] S. Kolling, H. Baaser, and D. Gross. Material forces due to crack-inclusion interaction. *International Journal of Fracture*, 118(3):229–238, 2002.

[KMZC+16] Justyna Kulczyk-Malecka, Xun Zhang, James Carr, Alexandra L. Carabat, Willem G. Sloof, Sybrand van der Zwaag, Federico Cernuschi, Franck Nozahic, Daniel Monceau, Claude Estournès, Philip J. Withers, and Ping Xiao. Influence of embedded MoSi2particles on the high temperature thermal conductivity of SPS produced yttria-stabilised zirconia model thermal barrier coatings. *Surface and Coatings Technology*, 308:31–39, 2016.

[KNH81] Vladimir V. Krstric, Patrick S Nicholson, and Richard G Hoagland. Toughening of Glasses by Metallic Particles. *Journal of the American Ceramic Society*, 64(9):499–504, 1981.

[KPF10] O. Kolednik, J. Predan, and F. D. Fischer. Reprint of "Cracks in inhomogeneous materials: Comprehensive assessment using the configurational forces concept". *Engineering Fracture Mechanics*, 77(18):3611–3624, 2010.

[KPS+05] O. Kolednik, J. Predan, G. X. Shan, N. K. Simha, and F. D. Fischer. On the fracture behavior of inhomogeneous materials - A case study for elastically inhomogeneous bimaterials. *International Journal of Solids and Structures*, 42(2):605–620, 2005.

[KPTK06] R. Kitey, A.-V. Phan, H. V. Tippur, and T. Kaplan. Modeling of crack growth through particulate clusters in brittle matrix by symmetric-Galerkin boundary element method. *International Journal of Fracture*, 141(1-2):11–25, 2006.

[Krs83] V. D. Krstic. On the fracture of brittle-matrix/ductile-particle composites. *Philosophical Magazine A: Physics of Condensed Matter, Structure, Defects and Mechanical Properties*, 48(5):695–708, 1983.

[KSKN04] Junya Kondoh, Hirohisa Shiota, Katsuhiro Kawachi, and Toshio Nakatani. Yttria concentration dependence of tensile strength in yttria-stabilized zirconia. *Journal of Alloys and Compounds*, 365(1-2):253–258, 2004.

[KSW03] M. R. Kessler, N. R. Sottos, and S. R. White. Self-healing structural composite materials. *Composites Part A: Applied Science and Manufacturing*, 34(8):743–753, 2003.

[KWHD02] M.G. Knight, L.C. Wrobel, J.L. Henshall, and L.A. De Lacerda. A study of the interaction between a propagating crack and an uncoated/coated elastic inclusion using the BE technique. *International Journal of Fracture*, 114(1):47–61, 2002.

[LC93] Rongshun Li and A. Chudnovsky. Energy analysis of crack interaction with an elastic inclusion. *International Journal of Fracture*, 63(3):247–261, 1993.

[LC02] Zhonghua Li and Qiang Chen. Crack-inclusion interaction for mode I crack analyzed by Eshelby equivalent inclusion method. *International Journal of Fracture*, 118(1):29–40, 2002.

[LHB96] J. W. Leggoe, X. Z. Hu, and M. B. Bush. Crack tip damage development and crack growth resistance in particulate reinforced metal matrix composites. *Engineering Fracture Mechanics*, 53(6):873–895, 1996.

[LJYY16] Wenting Li, Zhengwu Jiang, Zhenghong Yang, and Haitao Yu. Effective mechanical properties of self-healing cement matrices with microcapsules. *Materials and Design*, 95:422–430, 2016.

[LK95] P. Lipetzky and Z. Knesl. Crack-particle interaction in a two-phase composite Part II: crack deflection. *International Journal of Fracture*, 73(1):81–92, 1995.

[Llo91] D.J. Lloyd. Aspects of fracture in particulate reinforced metal matrix composites. *Acta Metallurgica et Materialia*, 39(1):59–71, 1991.

[LS94] P. Lipetzky and S. Schmauder. Crack-particle interaction in two-phase composites Part I: Particle shape effects. *International Journal of Fracture*, 65(4):345–358, 1994.

[LS08] S. Luding and A. S.J. Suiker. Self-healing of damaged particulate materials through sintering. *Philosophical Magazine*, 88(28-29):3445–3457, 2008.

[LSK+12] Shibo Li, Guiming Song, Kees Kwakernaak, Sybrand van der Zwaag, and Wim G. Sloof. Multiple crack healing of a Ti2AlC ceramic. *Journal of the European Ceramic Society*, 32(8):1813–1820, 2012.

[LZ13a] Yan Li and Min Zhou. Prediction of fracture toughness of ceramic composites as function of microstructure: I. Numerical simulations. *Journal of the Mechanics and Physics of Solids*, 61(2):472–488, 2013.

[LZ13b] Yan Li and Min Zhou. Prediction of fracturess toughness of ceramic composites as function of microstructure: II. analytical model. *Journal of the Mechanics and Physics of Solids*, 61(2):489–503, 2013.

[LZWZ10] J. Li, B. Y. Zong, Y. M. Wang, and W. B. Zhuang. Experiment and modeling of mechanical properties on iron matrix composites reinforced by different types of ceramic particles. *Materials Science and Engineering A*, 527(29-30):7545–7551, 2010.

[MB02] Nicolas Moës and Ted Belytschko. Extended finite element method for cohesive crack growth. *Engineering Fracture Mechanics*, 69(7):813–833, 2002.

[MCDH98] Y. Mi, M. A. Crisfield, G. A.O. Davies, and H. B. Hellweg. Progressive delamination using interface elements. *Journal of Composite Materials*, 32(14):1246–1272, 1998.

[MDB99] Nicolas Moës, John Dolbow, and Ted Belytschko. A finite element method for crack growth without remeshing. *International Journal for Numerical Methods in Engineering*, 46(1):131–150, 1999.

[MDB04] L Mishnaevsky, K Derrien, and D Baptiste. Effect of microstructure of particle reinforced composites on the damage evolution: probabilistic and numerical analysis. *Composites Science and Technology*, 64(12):1805–1818, 2004.

[MFvdZ09] Steven D. Mookhoek, Hartmut R. Fischer, and Sybrand van der Zwaag. A numerical study into the effects of elongated capsules on the healing efficiency of liquid-based systems. *Computational Materials Science*, 47(2):506–511, 2009.

[MG06] Spandan Maiti and Philippe H. Geubelle. Cohesive modeling of fatigue crack retardation in polymers: Crack closure effect. *Engineering Fracture Mechanics*, 73(1):22–41, 2006.

[MKS05] J. Mergheim, E. Kuhl, and P. Steinmann. A finite element method for the computational modelling of cohesive cracks. *International Journal for Numerical Methods in Engineering*, 63(2):276–289, 2005.

[ML90] M. Manoharan and J. J. Lewandowski. Crack initiation and growth toughness of an aluminum metal-matrix composite. *Acta Metallurgica Et Materialia*, 38(3):489–496, 1990.

[MP03] Stefano Mariani and Umberto Perego. Extended finite element method for quasi-brittle fracture. *International Journal for Numerical Methods in Engineering*, 58(1):103–126, 2003.

[MS13] Julia Mergheim and Paul Steinmann. Phenomenological modelling of self-healing polymers based on integrated healing agents. *Computational Mechanics*, 52(3):681–692, 2013.

[Nee90] A. Needleman. An analysis of tensile decohesion along an interface. *Journal of the Mechanics and Physics of Solids*, 38(3):289–324, 1990.

[NGKG05] T. D. Nguyen, S. Govindjee, P. A. Klein, and H. Gao. A material force method for inelastic fracture mechanics. *Journal of the Mechanics and Physics of Solids*, 53(1):91–121, 2005.

[NKMB14] S. Natarajan, P. Kerfriden, D. Roy Mahapatra, and S. P. A. Bordas. Numerical Analysis of the Inclusion-Crack Interaction by the Extended Finite Element Method. *International Journal for Computational Methods in Engineering Science and Mechanics*, 15(1):26–32, 2014.

[NSK+99] Marc-Oliver Nandy, Siegfried Schmauder, Byung-Nam Kim, Makoto Watanabe, and Teruo Kishi. Simulation of crack propagation in Alumina particle-dispersed SiC composites. *Journal of the European Ceramic Society*, 19(3):329–334, 1999.

[ÖKLB14] Kaan Özenç, Michael Kaliske, Guoyu Lin, and Grama Bhashyam. Evaluation of energy contributions in elasto-plastic fracture: A review of the configurational force approach. *Engineering Fracture Mechanics*, 115:137–153, 2014.

[OON16] Shingo Ozaki, Toshio Osada, and Wataru Nakao. Finite element analysis of the damage and healing behavior of self-healing ceramic materials. *International Journal of Solids and Structures*, 100-101:307–318, 2016.

[OP99] M. Ortiz and A. Pandolfi. Finite-deformation irreversible cohesive elements for three-dimensional crack-propagation analysis. *International Journal for Numerical Methods in Engineering*, 44(9):1267–1282, 1999.

[PB05a] J. W C Pang and I. P. Bond. 'Bleeding composites' - Damage detection and self-repair using a biomimetic approach. *Composites Part A: Applied Science and Manufacturing*, 36(2 SPEC. ISS.):183–188, 2005.

[PB05b] Jody W.C. Pang and Ian P. Bond. A hollow fibre reinforced polymer composite encompassing self-healing and enhanced damage visibility. *Composites Science and Technology*, 65(11-12):1791–1799, 2005.

[PBD91] A. Petitbon, L. Boquet, and D. Delsart. Laser surface sealing and strengthening of zirconia coatings. *Surface and Coatings Technology*, 49(1-3):57–61, 1991.

[Pet95] John J. Petrovic. Mechanical behavior of MoSi2and MoSi2composites. *Materials Science and Engineering A*, 192-193(PART 1):31–37, 1995.

[PS90] E. M. Patton and M. H. Santare. The effect of a rigid elliptical inclusion on a straight crack. *International Journal of Fracture*, 46(1):71–79, 1990.

[PT06] J. P. Parmigiani and M. D. Thouless. The roles of toughness and cohesive strength on crack deflection at interfaces. *Journal of the Mechanics and Physics of Solids*, 54(2):266–287, 2006.

[PTvdZ15] Sathiskumar A. Ponnusami, Sergio Turteltaub, and Sybrand van der Zwaag. Cohesive-zone modelling of crack nucleation and propagation in particulate composites. *Engineering Fracture Mechanics*, 149:170–190, 2015.

[PTZX15] Sathiskumar A. Ponnusami, Sergio Turteltaub, Xun Zhang, and Ping Xiao. Modelling crack propagation in particle- dispersed self-healing thermal barrier coatings. In S. van der Zwaag and Eddy Brinkman, editors, *Self Healing Materials- Pioneering Research in The Netherlands*, pages 229—-241. IOS Press, Netherlands, 2015.

[Qin14] Hai Qing. Micromechanical study of influence of interface strength on mechanical properties of metal matrix composites under uniaxial and biaxial tensile loadings. *Computational Materials Science*, 89:102–113, 2014.

[QL15] Hai Qing and Tianliang Liu. Micromechanical Analysis of SiC / Al Metal Matrix Composites: Finite Element Modeling and Damage Simulation. *International Journal of Applied Mechanics*, 07(02):1550023, 2015.

[QZR15] Md Shahriar Quayum, Xiaoying Zhuang, and Timon Rabczuk. Computational model generation and RVE design of self-healing concrete. *Journal of Contemporary Physics*, 50(4):383–396, 2015.

[Rab08] Oded Rabinovitch. Debonding analysis of fiber-reinforced-polymer strengthened beams: Cohesive zone modeling versus a linear elastic fracture mechanics approach. *Engineering Fracture Mechanics*, 75(10):2842–2859, 2008.

[RBS09] V. A. Romanova, R. R. Balokhonov, and S. Schmauder. The influence of the reinforcing particle shape and interface strength on the fracture behavior of a metal matrix composite. *Acta Materialia*, 57(1):97–107, 2009.

[RdBN08] Joris J C Remmers, René de Borst, and Alan Needleman. The simulation of dynamic crack propagation using the cohesive segments method. *Journal of the Mechanics and Physics of Solids*, 56(1):70–92, 2008.

[RRK12] Julian J Rimoli, Juan J Rojas, and Farah N Khemani. On the mesh dependency of cohesive zone models for crack propagation analysis. In *AIAA/ASME/ASCE/AHS/ASC Structures, Structural Dynamics and Materials Conference*, pages 1–9, 2012.

[RSR92] K. T. Venkateswara Rao, W. O. Soboyejo, and R. O. Ritchie. Ductile-phase toughening and Fatigue-Crack Growth in Nb-Reinforced Molybdenum Disilicide Intermetallic Composites. *Metallurgical Transactions A*, 23(8):2249–2257, 1992.

[SA04] Ahmet Selçuk and Alan Atkinson. Strength and Toughness of Tape-Cast Yttria-Stabilized Zirconia. *Journal of the American Ceramic Society*, 83(8):2029–2035, 2004.

[SBNS17] Hamid Shahsavari, Mostafa Baghani, Reza Naghdabadi, and Saeed Sohrabpour. A thermodynamically consistent viscoelastic–viscoplastic constitutive model for self-healing materials. *Journal of Intelligent Material Systems and Structures*, page 1045389X1773091, 2017.

[SCMB01] M. Stolarska, D. L. Chopp, N. Mos, and T. Belytschko. Modelling crack growth by level sets in the extended finite element method. *International Journal for Numerical Methods in Engineering*, 51(8):943–960, 2001.

[ŠFA+16] Branko Šavija, João Feiteira, Maria Araújo, Sutima Chatrabhuti, Jean-Marie Raquez, Kim Van Tittelboom, Elke Gruyaert, Nele De Belie, and Erik Schlangen. Simulation-Aided Design of Tubular Polymeric Capsules for Self-Healing Concrete. *Materials (Basel, Switzerland)*, 10(1), 2016.

[SFK+05] N. K. Simha, F. D. Fischer, O. Kolednik, J. Predan, and G. X. Shan. Crack tip shielding or anti-shielding due to smooth and discontinuous material inhomogeneities. *International Journal of Fracture*, 135(1-4):73–93, 2005.

[SFS+08] N. K. Simha, F. D. Fischer, G. X. Shan, C. R. Chen, and O. Kolednik. J-integral and crack driving force in elastic-plastic materials. *Journal of the Mechanics and Physics of Solids*, 56(9):2876–2895, 2008.

[SKÜW01] Joachim H. Schneibel, M. J. Kramer, Ö Ünal, and Richard N. Wright. Processing and mechanical properties of a molybdenum silicide with the composition Mo-12Si-8.5B (at.%). *Intermetallics*, 9(1):25–31, 2001.

[SMD+88] L.S. Sigl, P.A. Mataga, B.J. Dalgleish, R.M. McMeeking, and A.G. Evans. On the toughness of brittle materials reinforced with a ductile phase. *Acta Metallurgica*, 36(4):945–953, 1988.

[SON17] A. Srivastava, S. Osovski, and A. Needleman. Engineering the crack path by controlling the microstructure. *Journal of the Mechanics and Physics of Solids*, 100:1–20, 2017.

[SPM+16] Willem G. Sloof, Ruizhi Pei, Samuel A. McDonald, Julie L. Fife, Lu Shen, Linda Boatemaa, Ann Sophie Farle, Kun Yan, Xun Zhang, Sybrand van der Zwaag, Peter D. Lee, and Philip J. Withers. Repeated crack healing in MAX-phase ceramics revealed by 4D in situ synchrotron X-ray tomographic microscopy. *Scientific Reports*, 6(1):23040, 2016.

[SPP10] G. G. Sozhamannan, S. Balasivanandha Prabu, and R. Paskaramoorthy. Failures analysis of particle reinforced metal matrix composites by microstructure based models. *Materials and Design*, 31(8):3785–3790, 2010.

[SPS+08] G. M. Song, Y. T. Pei, W. G. Sloof, S. B. Li, J. Th M. De Hosson, and S. van der Zwaag. Oxidation-induced crack healing in Ti3AlC2ceramics. *Scripta Materialia*, 58(1):13–16, 2008.

[SR06] E C Schimmel and J Remmers. Development of a constitutive model for self-healing materials. Technical report, Delft Aerospace Computational Science, 2006.

[SR09] Andrew Seagraves and Raúl Radovitzky. Advances in Cohesive Zone Modeling of Dynamic Fracture. In *Dynamic Failure of Materials and Structures*, pages 349–405. Springer US, Boston, MA, 2009.

[Sri96] T. S. Srivatsan. Microstructure, tensile properties and fracture behaviour of Al2O3 particulate-reinforced aluminium alloy metal matrix composites. *Journal of Materials Science*, 31(5):1375–1388, 1996.

[SS03] J. H. Schneibel and J. A. Sekhar. Microstructure and properties of MoSi2-MoB and MoSi2-Mo5Si3molybdenum silicides. *Materials Science and Engineering A*, 340(1-2):204–211, 2003.

[SSL15] Amir Shojaei, Soodabeh Sharafi, and Guoqiang Li. A multiscale theory of self-crack-healing with solid healing agent assisted by shape memory effect. *Mechanics of Materials*, 81:25–40, 2015.

[Sta17] ASTM Standard. E399 standard test method for linear-elastic plane-strain fracture toughness kic of metallic materials. *ASTM book of standards*, 2017.

[STD+15] Willem G. Sloof, Sergio Turteltaub, Z. Derelioglu, Sathiskumar A. Ponnusami, and G. Song. Crack healing in yttria stabilized zirconia thermal barrier coatings. In S. van der Zwaag and Eddy Brinkman, editors, *Self Healing Materials- Pioneering Research in The Netherlands*, pages 219–227. IOS Press, Netherlands, 2015.

[SY05] Xudong Sun and Julie Yeomans. Optimization of a Ductile-Particle-Toughened Ceramic. *Journal of the American Ceramic Society*, 79(10):2705–2717, 2005.

[Tam68] Osamu Tamate. The effect of a circular inclusion on the stresses around a line crack in a sheet under tension. *International Journal of Fracture Mechanics*, 4(3):257–266, 1968.

[TH92] Viggo Tvergaard and John W. Hutchinson. The relation between crack growth resistance and fracture process parameters in elastic-plastic solids. *Journal of the Mechanics and Physics of Solids*, 40(6):1377–1397, 1992.

[T.L05] T.L.Anderson. *Fracture mechanics : fundamentals and applications*. CRC press, 2005.

[TSL+07] Kathleen S. Toohey, Nancy R. Sottos, Jennifer A. Lewis, Jeffrey S. Moore, and Scott R. White. Self-healing materials with microvascular networks. *Nature Materials*, 6(8):581–585, 2007.

[UKP09] Ani Ural, Venkat R. Krishnan, and Katerina D. Papoulia. A cohesive zone model for fatigue crack growth allowing for crack retardation. *International Journal of Solids and Structures*, 46(11-12):2453–2462, 2009.

[VD13] Kim Van Tittelboom and Nele De Belie. Self-healing in cementitious materials-a review. *Materials*, 6(6):2182–2217, 2013.

[vdZ07] Sybrand van der Zwaag, editor. *Self Healing Materials: An Alternative Approach to 20 Centuries of Materials Science*, volume 100 of *Springer Series in Materials Science*. Springer Netherlands, 2007.

[vdZB15] S. van der Zwaag and Eddy Brinkman, editors. *Self Healing Materials: Pioneering Research in the Netherlands*. IOS Press, Netherlands, 2015.

[VJS+10] Robert Vaßen, Maria Ophelia Jarligo, Tanja Steinke, Daniel Emil Mack, and Detlev Stöver. Overview on advanced thermal barrier coatings. *Surface and Coatings Technology*, 205(4):938–942, 2010.

[VSL11] George Z. Voyiadjis, Amir Shojaei, and Guoqiang Li. A thermodynamic consistent damage and healing model for self healing materials. *International Journal of Plasticity*, 27(7):1025–1044, 2011.

[VSLK12] G. Z. Voyiadjis, A. Shojaei, G. Li, and P. I. Kattan. A theory of anisotropic healing and damage mechanics of materials. *Proceedings of the Royal Society A: Mathematical, Physical and Engineering Sciences*, 468(2137):163–183, 2012.

[Wan10] John T Wang. Relating Cohesive Zone Models to Linear Elastic Fracture Mechanics. Technical Report May, NASA Technical Report, 2010.

[WJ11] Virginie Wiktor and Henk M. Jonkers. Quantification of crack-healing in novel bacteria-based self-healing concrete. *Cement and Concrete Composites*, 33(7):763–770, 2011.

[WPT+07] R.C. Williams, A.-V. Phan, H.V. Tippur, T. Kaplan, and L.J. Gray. SGBEM analysis of crack–particle(s) interactions due to elastic constants mismatch. *Engineering Fracture Mechanics*, 74(3):314–331, 2007.

[WS01] G. N. Wells and L. J. Sluys. A new method for modelling cohesive cracks using finite elements. *International Journal for Numerical Methods in Engineering*, 50(12):2667–2682, 2001.

[WSB08] Wenhai Wang, Keya Sadeghipour, and George Baran. Finite element analysis of the effect of an interphase on toughening of a particle-reinforced polymer composite. *Composites Part A: Applied Science and Manufacturing*, 39(6):956–964, 2008.

[WSG+01] S. R. White, N. R. Sottos, P. H. Geubelle, J. S. Moore, M. R. Kessler, S. R. Sriram, E. N. Brown, and S. Viswanathan. Autonomic healing of polymer composites. *Nature*, 409(6822):794–797, 2001.

[WSLC12] J. J. Williams, J. Segurado, J. LLorca, and N. Chawla. Three dimensional (3D) microstructure-based modeling of interfacial decohesion in particle reinforced metal matrix composites. *Materials Science and Engineering A*, 557:113–118, 2012.

[WST86] K. Wallin, T. Saario, and K. Törrönen. Fracture of brittle particles in a ductile matrix. *International Journal of Fracture*, 32(3):201–209, 1986.

[WTB07] G. Williams, R. Trask, and I. Bond. A self-healing carbon fibre reinforced polymer for aerospace applications. *Composites Part A: Applied Science and Manufacturing*, 38(6):1525–1532, 2007.

[XC01] Z. M. Xiao and B. J. Chen. Stress intensity factor for a Griffith crack interacting with a coated inclusion. *International Journal of Fracture*, 108(3):193–205, 2001.

[XN94] X. P. Xu and A. Needleman. Numerical simulations of fast crack growth in brittle solids. *Journal of the Mechanics and Physics of Solids*, 42(9):1397–1434, 1994.

[XSKZ14] Wei Xu, Xin Sun, Brian J. Koeppel, and Hussein M. Zbib. A continuum thermo-inelastic model for damage and healing in self-healing glass materials. *International Journal of Plasticity*, 62:1–16, 2014.

[YJ91] J. M. Yang and S. M. Jeng. Interface and mechanical behavior of MoSi2-based composites. *Journal of Materials Research*, 6(3):505–513, 1991.

[ZCK+16] Pingping Zhu, Zhiwei Cui, Michael S. Kesler, John A. Newman, Michele V. Manuel, M. Clara Wright, and L. Catherine Brinson. Characterization and modeling of three-dimensional self-healing shape memory alloy-reinforced metal-matrix composites. *Mechanics of Materials*, 103:1–10, 2016.

[ZJV11] Serguey V. Zemskov, Henk M. Jonkers, and Fred J. Vermolen. Two analytical models for the probability characteristics of a crack hitting encapsulated particles: Application to self-healing materials. *Computational Materials Science*, 50(12):3323–3333, 2011.

[ZOG+16] Jie Zhang, Qiubao Ouyang, Qiang Guo, Zhiqiang Li, Genlian Fan, Yishi Su, Lin Jiang, Enrique J. Lavernia, Julie M. Schoenung, and Di Zhang. 3D Microstructure-based finite element modeling of deformation and fracture of SiCp/Al composites. *Composites Science and Technology*, 123:1–9, 2016.

SUMMARY

Research in the field of self-healing materials gained significant attention in the last decade owing to its promise of enhanced durability of the material components in engineering applications. Though the research has led to several successful demonstrations, extensive experimental tests will be required for a successful demonstration. Further, for real-time engineering applications with self-healing materials, arriving at an optimal design of the self-healing system is crucial. In this context, modelling techniques in combination with a limited number of experimental tests are potentially more efficient than a design process based on extensive experimental campaigns. With this motivation, the present thesis aims to develop a modelling framework to analyse and understand the fracture mechanisms and the healing behaviour of self-healing material systems using finite element modelling approach. The overall objective is to provide certain guidelines and suggestions for material scientists in terms of selection and design of healing particles and a computational tool to understand and quantify the cracking and healing behaviour of self-healing material systems.

Chapter 1: A brief introduction to self-healing materials is presented while highlighting two major classes of self-healing materials, namely, the intrinsic and the extrinsic. The healing mechanisms and the routes are briefly discussed. Fracture mechanisms in a Thermal Barrier Coating (TBC) system are discussed followed by introducing the concept of self-healing TBC, aiming at extending the lifetime of the TBC systems. The challenges and key issues associated with the successful realisation of a self-healing material are discussed and the need for modelling techniques to address those issues are highlighted. Finally, the outline of the thesis is explained towards the end of the chapter.

Chapter 2: The crucial issue of crack-healing particle interaction is studied in great detail. Three major failure mechanisms, namely matrix cracking, interface debonding and particle fracture are considered. Finite element analyses using embedded cohesive elements all over the mesh are utilised to study the fracture process in a single particle-matrix system. The conditions under which a matrix crack ruptures the healing particle are established. Fracture maps are generated which differentiate the cracking mechanisms as a function of mismatch in elastic and fracture properties between the particle and the matrix. Further, the effect of pre-existing defects on the crack path is investigated. In the end, the consolidated results will serve as a set of design guidelines and suggestions for experimentalists to arrive at a successful design of a self-healing material system.

Chapter 3: In this chapter, instead of a single particle-matrix system, the topology of a real microstructure of a SPS produced TBC system with healing particles is utilised to develop the finite element model and the fracture mechanisms are investigated as a function of mismatch in fracture properties of the constituents. While the study in chapter 2 aims at predicting the local crack path in the vicinity of the healing particle, this chapter goes one step further and evaluate the effect of particle and interface properties on the global mechanical properties of the composite. This is a useful study as it reveals the effect of dispersed healing particles in an otherwise homogenous phase on the global mechanical properties. This, in turn, helps to properly engineer the particle properties such that deterioration of host material's properties is not too severe.

Chapter 4: The objective of this chapter is to develop a generic fracture mechanics-based crack healing model that could serve as a design and analysis tool for successful development of self-healing materials. A cohesive zone-based constitutive law, originally developed to model fracture, is extended to include a healing variable to simulate crack healing process and thus recovery of mechanical properties. The proposed model is a composite type material model that accounts for the properties of both the original and the healing material, which are typically different. The developed constitutive model is implemented in a finite element framework through the use of cohesive elements. The resulting numerical framework is capable of modelling both extrinsic and intrinsic self-healing materials. The model is capable of dealing with multiple healing events, which is relevant for self-healing materials in real-life applications. Salient features of the model are demonstrated through simple examples followed by application of the model to a representative extrinsic self-healing material system.

Chapter 5: In this chapter, the recovery of mechanical properties of a MAX-phase ceramic Ti_2AlC, upon high-temperature oxidation is investigated using an experimental-numerical approach. A wedge-induced fracture test is used to determine the fracture properties of not only the virgin material but also that of the healed crack. The crack healing model developed in chapter 4 is utilized to model the cracking behavior in both conditions and to determine the values for fracture strength as well as fracture energy. In order to showcase the features of the model, parametric studies are conducted with varying the ratio of healed to total crack length. Further, healing efficiency is defined in terms of strength and energy recovery and their utility is demonstrated using the results of the parametric analysis. Fracture and healing experiments are conducted on a single Ti_2AlC specimen and the results are compared with the modelling outcomes.

Chapter 6: In previous chapters, in particular, in chapters 2 and 3, the effect of the healing particles on crack driving force is not quantified explicitly, rather the crack paths and global load-displacement plots were presented. It is the objective of this chapter to quantify the driving force, which is the energy release rate, for different mismatches in the mechanical properties between the particle and the matrix. For this purpose, the concept of configurational forces is utilized and eXtended Finite

Element Method (XFEM) is employed as a tool to simulate crack propagation. Two specific issues have been addressed. Firstly, the configurational forces associated with the crack and the inhomogeneities are quantified, which in turn yield the direction of the crack propagation, simulated by XFEM. The second objective of this chapter is to analyse the influence of fracture process zone on the results of the crack driving force and the crack path, which ultimately provide insights on the differences between the cohesive zone model and classical fracture mechanics approaches.

SAMENVATTING

In de afgelopen twee decennia kreeg het vakgebied van de zelf-herstellende materialen veel aandacht vanwege de nieuwe mogelijkheden die hiermee verkregen worden om technische installaties langer en betrouwbaarder te laten functioneren. Hoewel het onderzoek geleid heeft tot enkele veelbelovende projecten zijn nog heel veel experimenten nodig om te komen tot daadwerkelijke toepassingen van deze nieuwe klasse materialen. Het zou mooi zijn als de huidige, op veel experimenten gebaseerde aanpak vervangen zou kunnen worden door één waarbij optimaal zelf herstellende materialen via computer berekening, in combinatie met slecht een paar experimenten, ontwikkeld zouden kunnen worden.

Met dit doel voor ogen beschrijft dit proefschrift de ontwikkeling van een conceptueel framework om zowel het breuk- als het herstel gedrag van materialen middels eindige elementen modellen te kunnen beschrijven en te voorspellen. Meer specifiek beoogt dit proefschrift richtlijnen te geven aan materiaalkundigen voor de selectie van de deeltje en hun concentratie teneinde een optimaal zelfherstellend gedrag met behoud van de gewenste initiële eigenschappen te verkrijgen.

Hoofdstuk 1: dit hoofdstuk begint met een inleiding in het gebied van zelfherstellende materialen en introduceert de begrippen extrinsieke en intrinsieke zelfherstellende materialen en de bijbehorende mechanismes worden uitgelegd. De breukmechanica van Thermal Barrier Coatings (TBCs), dunne coatings met een zeer lage warmtegeleiding, wordt besproken. De kenmerken aan welke een zelfherstellende TBC moet voldoen om een langere levensduur te verkrijgen zijn op een hoog abstractie nivo besproken. Dit zou het beste kunnen geschieden in de context van modelgestuurde materiaalontwikkeling. Dit hoofdstuk introduceert ook de diverse hoofdstukken in het proefschrift.

Hoofdstuk 2: In dit hoofdstuk wordt de interactie tussen een scheur en het deeltje dat een stof zal afscheiden die in staat is de scheur te vullen en te repareren (vanaf nu te benoemen als 'het deeltje'), in detail geanalyseerd. De interactie kan leiden tot een scheur die zich voortplant in de matrix, door het deeltje of langs het grensvlak tussen beide. Een eindige element model dat gebruik maakt van zogenaamde 'cohesive zone' elementen is gebruikt om te komen tot de voorspellende beschrijving van het scheurpad in een systeem bestaande uit een homogene matrix, een enkele scheur en één enkel (bolvormig) deeltje. De analyse leidt tot grafieken waaruit het te verwachten scheurgedrag afgelezen kan worden als functie van de elastische eigenschappen van het deeltje genormaliseerd op die van het matrix materiaal. Ook het effect van

aanwezige microscheuren op het scheurpatroon is geanalyseerd. Het totaal biedt een set van duidelijke richtlijnen voor experimentele materiaalkundigen om te komen tot een gewenste interactie tussen scheuren en deeltjes.

Hoofdstuk 3: het werk in dit hoofdstuk bouwt verder op dat van hoofdstuk 2 en analyseert het breukgedrag van een 2-dimansionaal systeem met veel deeltjes en een topologie die een kopie is van een experimenteel vervaardigd proefstuk. In het eindige elementen model zijn de breukmechanische eigenschappen van de twee samenstellende materialen gevarieerd om te onderzoeken welk effect dat heeft op zowel het scheurpatroon als op de uiteindelijke mechanische eigenschappen van het materiaal als geheel. Dit is uitermate nuttige information omdat het de materiaalontwikkelaars in staat moet stellen het systeem te optimaliseren voor zelfherstellend gedrag zonder daarmee te zeer afbreuk te doen aan de initiële mechanische eigenschappen van de TBC.

Hoofdstuk 4: doel van het werk in dit hoofdstuk was om het ontwikkelde 'cohesive zone' eindige elementen model verder uit te bouwen door het ook geschikt te maken om het breukgedrag te beschrijven nadat zelfherstel heeft plaatsgevonden. Het nieuwe model houdt rekening houdt met de verschillen in breukmechanische eigenschappen van het uitgangsmateriaal en het materiaal dat in de scheur gevormd is. Wederom zijn cohesive zone elementen op grote schaal toegepast. Het model is in staat het breukgedrag van zowel intrinsieke als extrinsieke zelfherstellende materialen te beschrijven. Daarnaast is het model ook in staat het breukgedrag te beschrijven voor het geval van meerdere breuk en herstel cycli, hetgeen van groot belang is voor het voorspellen van het gedrag onder realistische praktijkcondities. De mogelijkheden van het model zijn geïllustreerd in een aantal relevante 'case studies'. Hoofdstuk 4: doel van het werk in dit hoofdstuk was om het ontwikkelde 'cohesive zone' eindige elementen model verder uit te bouwen door het ook geschikt te maken om het breukgedrag te beschrijven nadat zelfherstel heeft plaatsgevonden. Het nieuwe model houdt rekening houdt met de verschillen in breukmechanische eigenschappen van het uitgangsmateriaal en het materiaal dat in de scheur gevormd is. Wederom zijn cohesive zone elementen op grote schaal toegepast. Het model is in staat het breukgedrag van zowel intrinsieke als extrinsieke zelfherstellende materialen te beschrijven. Daarnaast is het model ook in staat het breukgedrag te beschrijven voor het geval van meerdere breuk and herstel cycli, hetgeen van groot belang is voor het voorspellen van het gedrag onder realistische praktijkcondities. De mogelijkheden van het model zijn geïllustreerd in een aantal relevante 'case studies'.

Hoofdstuk 5: in dit hoofdstuk wordt een gecombineerd experimenteel-theoretisch onderzoek naar het herstelgedrag van een MAX phase keramiek Ti2AlC als gevolg van hoge temperatuur oxidatieve behandeling gepresenteerd. Een breuktest waarbij een wig in een voorgevormde groef in het proefstuk gedrukt wordt, is gebruikt om de sterkte van zowel het oorspronkelijke materiaal als dat van de herstelde scheur te bepalen. Het in hoofdstuk 4 ontwikkelde model is gebruikt om uit de

experimenteel bepaalde kracht-verplaatsings data en de acoustische emissie data zowel de breuksterkte als de breukenergie te bepalen. De mogelijkheden van het model zijn verder geïllustreerd in een parametrische studie naar het effect van de relatieve lengte van het herstelde deel van de scheur op het verdere breukgedrag. Mede op basis van die analyse kan een onderscheid gemaakt worden in de mate van herstel op basis van de herwonnen breuksterkte dan wel op basis van de herwonnen breukenergie.

Hoofdstuk 6: in de eerdere hoofstukken, met name hoofdstukken 2 en 3 is voor de een extrinsiek zelf herstellend modelsysteem onderzoek gedaan naar het breukpad in relatie tot de kracht-verplaatsings krommes op proefstuk nivo. Daarbij is geen aandacht geschonken aan de eigenlijke drijvende kracht voor de scheurpropagatie. Doel van het onderzoek in dit hoofdstuk is het bepalen van de drijvende kracht, i.e. het vrijkomen van de elastische energie, als functie van de mechanische eigenschappen van de matrix en de deeltjes. Hiertoe is in dit hoofdstuk het zogenaamde 'configurational force' concept gebruikt in combinatie met een eXtended eindige elementen, XFEM benadering. Met dit nieuwe model konden de lokale krachten tussen de scheur en de deeltjes in de matrix bepaald worden en daaruit kon de scheurrichting gedestilleerd worden. Het onderzoek richtte zich verder op het bepalen van de invloed van de beïnvloede zone rond de scheurtip op de drijvende kracht voor scheurgroei en het breukpad. Deze analyse geeft inzicht in het verschil tussen het modelleren van breuk middels 'cohesive zone' elementen en dat via klassieke lineair elastische breukmechanica.

CURRICULUM VITAE

Sathiskumar Anusuya Ponnusami was born in Virudhunagar district in the southern Indian State, Tamil Nadu in the year 1988. After his school education, he went on to pursue Bachelor of Engineering degree in Aeronautics in Anna University to become the first college graduate in his family. Having graduated with his Bachelor's degree with distinction in 2009, he got qualified in Graduate Aptitude Test in Engineering (GATE) examination in 2009 with an All India Rank of 25, which is a national level competitive entrance examination for admission into India's leading universities such as Indian Institute of Science (IISc) and Indian Institute of Technology (IIT). Subsequently, he got admission for Master's program in Aerospace Engineering in India's premier research institute, IISc in the Department of Aerospace Engineering. It is at IISc, where he gradually developed interest in the field of aerospace structures and mechanics, thanks to the course Flight Vehicle Structures offered by Prof. Dineshkumar Harursampath in the Aerospace Engineering Department. His Master's project conducted at IISc and National Aerospace Laboratories in Bangalore won the Outstanding Performance Award at Mahindra Young Engineer Awards 2010 in Structures category.

After graduating with a Master's degree with distinction, he got an opportunity to conduct his doctoral research at Delft University of Technology in the Faculty of Aerospace Engineering towards the end of 2011. During his period at TU Delft, he enjoyed working in a fascinating subject of self-healing materials and attempted to establish some useful guidelines and tools that enable material scientists to understand and successfully design a self-healing material. Apart from his main research topic, he got varied opportunities to explore his research interests. He participated in Airbus Fly Your Ideas Global Challenge conducted by Airbus in collaboration with UNESCO with a project titled, 'A hybrid piezo-battery composite for next generation aircraft', an altogether different topic from his doctoral research. He led his team of 5 members from four different international universities in four different countries spanning three continents. At the end of six-month period comprising three rounds involving 518 teams from over 100 countries, his team, MultiFun was crowned as the Global Champion of the 2015 Challenge in the Finals held at Airbus German Headquarters in Hamburg with a trophy and cash prize of 30,000 euros. He was also awarded the NLF Dutch Aerospace Award 2015 in the University category by Netherlands Aerospace Funds with a cash award of 5000 euros. Other recognitions include Young Scientist Award in International Conference on Self-healing Materials (ICSHM 2015) held in Belgium, Future Materials Awards by Future Materials Magazine and World Textile Information Network held at Milan, Italy. He is currently working as a researcher in Solid Mechanics Group at the University of Oxford in the United Kingdom.

ACKNOWLEDGEMENTS

This research work was conducted in the Department of Aerospace Structures and materials at the Faculty of Aerospace Engineering in Delft University of Technology. I'm grateful for the support I received from the Aerospace Structures and Computational Mechanics Chair.

I dedicate this little thesis book to all of my teachers at different phases of my life starting from school till my research at TU Delft.

I would like to thank my promotor Prof. dr. ir. Sybrand van der Zwaag for his excellent guidance, timely feedback and suggestions, which greatly helped in completing the thesis. Directly through his advice in my research and indirectly by observing his mentoring style, I learnt how a structured way of doing research without any compromise in creativity could yield splendid outcome. Time management and his communication techniques are some great skills that I would like to inherit from him.

I would like to extend my sincere thanks and gratitude to Dr. Sergio Turteltaub, my PhD supervisor for his mentorship and guidance throughout the research. Enjoying what you do, paying attention to details and perfectionism in research are some important habits and skills which I could take home as learnings from him over the years. Thanks in particular for several of the detailed discussions which helped in resolving issues encountered during the research. More importantly, it was such discussions which act as a trigger to understand the broader picture of the subject of fracture and computational mechanics, which ultimately is crucial for a researcher to develop a philosophical perspective on technical subjects. I'm grateful to my promotor Prof. dr. Chiara Bisagni, for her support and mentorship during my last years of PhD. In particular, thanks for her advice and support during the Airbus Fly Your Ideas Competition 2015. I would like to thank Prof.dr.ir. Akke Suiker for providing me the opportunity to conduct my PhD research at TU Delft.

Sincere thanks and gratitude to Prof. dr. ir. Wim Sloof, Faculty of 3mE, without his support and help, I wouldn't have got exposure to experimental aspects of material science and engineering. Special mentions to multiple meetings and discussions with him and his group at 3mE. Thanks go to my experimental collaborators, Zeynep, Ann-Sophie, Alexandra, Linda and Toshio at 3mE. My sincere thanks to Dr. Christos Kassapoglu for his encouragement and positive words during meetings and discussions. Thanks to Prof. Niels van Dijk for discussions and our short collaborations. I would also like to thank my promotors for extending their support for my other ventures such as participating in Airbus Fly Your Ideas Challenge during my time at Delft.

My heartfelt gratitude to Dr. Dineshkumar Harursampath for being my mentor and teacher during my time at Indian Institute of Science(IISc) and beyond. I'm sure your mentorship at different levels during my time at IISc and Delft will have a profound influence on my career and life. As I always say, your course on Flight Vehicle Structures is the best course that I had attended. My gratitude to Harursampath family for the wonderful few months time spent at Delft. Special mention and thanks to my twelve-year long friend Jayaprakash, for all the help and our collaboration which helped very much in my thesis. I hope and look forward to offering the same for your thesis work.

Apart from conducting PhD research, a great experience while being in Delft is my participation in Airbus Fly Your Ideas Global Innovation Challenge 2015 over a period of six months. First thanks to Dr. Harursampath, our team mentor at IISc for facilitating me to lead an international team with students from universities such as Georgia Tech, City University of London, Indian Institute of Science apart from myself being at TU Delft. The whole experience of winning in the competition has been truly inspiring on several fronts as it helped to understand and appreciate industrial perspectives on innovation. It also reinforced the need for even more closer academia-industrial collaborations to accelerate next-generation innovation. Big thanks to my team members Dhamotharan, Mohit, Shashank, Ajith and Airbus mentors Deniz and Christian from Toulouse and Hamburg respectively. Acknowledgments to Airbus, UNESCO and Fly Your Ideas team for all their support during the competition and for hosting our team at Airbus Hamburg during the Grand Finale. I would like to acknowledge Nederlandse Luchtvaart Fonds for the Dutch Aerospace Award 2015 in university category.

Many thanks go to my colleagues and group members in ASCM, Sourena, Pooria, Weiling, Ke, Daniel, Rijk, Zhenpei, Sonell, Zhi and Jaco. One important person without whom it would have been difficult to get the administrative tasks done is our secretary Laura Chant. Thanks Laura for your help. Many thanks to Jan Hol for all his support in using the software facilities and more at ASCM. Thanks to Professor Arbocz, Alan, Roeland, Arvind, Martin, Gillian, Javad, Julien, Eddy, Attila, Ali, Miranda, Fardin, Dan, Darwin, Yujie, Darun, Niels, Adriaan, Etana, Darwin, Jurij, Louis, Noud and Sam for the good time that I had spent with you all. Thanks to my colleagues and friends at NovAM Group: Shanta, Santiago, Nijesh, Antonio, Ranjita, Srikant and Arianna.

Thanks to my friends Krishnamoorthy, Dhamu, Sudhakar anna, Prapanj anna, Ankita, Muthu anna, Anand Uthandi, Mahipal, Satish, Rajasekar, Vignesh, Vishal, Vivek, Shaafi, Wasim, Sreenath, Yasser, Ganapathy anna, Navneet, Murali, Vinoth, Balaji G, Sanjay, Varun, Sanath, Stephen, Deepan, Mohan, Balaji R, Sandeep, Adi, Prasanna, Nishant, Anand, Sachin for making my life enjoyable in Delft and in Europe. Thanks to all of my friends back in India who have been an important part of my life at different times. I hold all the good memories with you close to my heart.

I would like to acknowledge the (financial) support provided by the Netherlands Enterprise Agency (IOP SHM). Thanks to IOP SHM for providing the support for Self-healing

summer school and also providing the opportunity to convey my research ideas in symposiums and conferences. I would like to extend my sincere thanks to Engineering Mechanics Graduate school for several useful courses at three technical universities in the Netherlands and offering me a platform to interact with fellow researchers through oral and poster presentations in Engineering Mechanics symposiums.

There are many people in Delft outside the TU who have been a tremendous support during my time in the Netherlands. Thanks in particular to Kamal anna, whose help and support cannot be matched with a 'thank you'. My love to Christa and Jan Botermans with whom I have spent some quality time in Delft and Pijnacker. Their care and moral support during various times is something that is difficult to pay back. My gratitude to Mohan anna and Rangarajan sir for their warm friendship and some great insightful discussions.

I take this opportunity to express my love and utmost gratitude to my dear Amma, Anusuya and my dear Appa, Ponnusami. Thank you for your unconditional love and support. My dear Sangheetha paapa, you have been a wonderful sister supporting all the way in my life. My heartfelt love to you! Thank you, Karthick Ponraj for being my good friend and a wonderful life partner to my sister. The new member of our family, Aadhira kutty will make our lives even more beautiful. Thank you, Chitra ma and Pradeep pa. My sincere respects to you for being an excellent example to our society for taking an evidently progressive approach towards woman's education. Love and gratitude to my family members: Periamma, Periyappa, Chithi, Chithappa, Thaatha, Paati, Dhana, Anand, Rajkumar maama, Yuvaraj and Dhayan maama, Athai, Maama, Balaji, Jayakumar, Rajnarayanan maama, Dinesh, Yaamini, Roshini, Navaneethan pa and Vasantha ma. Last, but not the least, my dearest girlfriend and fiancé, Yazhini, a truly amazing person to be with. Thank you for being with me at all times despite several challenges and difficult times. I look forward to spending our lives together. Love you! By the way, while writing this, I can finally say that I'm finishing my PhD.

Sathiskumar A Ponnusami
Delft, January 2018

PAPERS AND CONFERENCE PRESENTATIONS

Book Chapters:

1. Sathiskumar A. Ponnusami, S.R. Turteltaub, X. Zhang and P. Xiao (2015), Modelling crack propagation in particle-dispersed self-healing thermal barrier coatings, in: Self Healing Materials- Pioneering Research in The Netherlands, edited by S. van der Zwaag, IOS Press, Amsterdam, The Netherlands (pp. 219-227)..

2. W.G. Sloof, S.R. Turteltaub, Z. Derelioglu, G.M. Song, Sathiskumar A. Ponnusami (2015), Crack healing in yttria stabilized zirconia thermal barrier coatings, in: Self Healing Materials- Pioneering Research in The Netherlands, edited by S. van der Zwaag, IOS Press, Amsterdam, The Netherlands (pp. 229-241).

Journal articles:

1. Sathiskumar A. Ponnusami, Sergio Turteltaub, Sybrand van der Zwaag (2015), Cohesive-zone modelling of crack nucleation and propagation in particulate composites, Engineering Fracture Mechanics, Volume 149, November 2015, Pages 170-190.

2. Blonde, R., Jimenez-Melero, E., Sathiskumar A. Ponnusami, Zhao, L., Schell, N., Bruck, E., and Dijk, N. V. (2014), Position-dependent shear-induced austenite-martensite transformation in double-notched TRIP and dual-phase steel samples, Journal of Applied Crystallography, 47(3).

3. Sathiskumar A. Ponnusami, Jayaprakash Krishnamsay, Sergio Turteltaub, Sybrand van der Zwaag, A cohesive-zone crack healing model for self-healing materials, International Journal of Solids and Structures, Available online, November 2017, Volume 134, March 2018, Pages 249-263.

4. Sathiskumar A. Ponnusami, Jayaprakash Krishnamsay, Sergio Turteltaub, Sybrand van der Zwaag, A micromechanical fracture analysis to investigate the effect of healing particles on the overall mechanical response of a self-healing particulate composite, article in the process of submission.

5. Sathiskumar A. Ponnusami, Jayaprakash Krishnamsay, Sergio Turteltaub, Sybrand van der Zwaag, Assesment of crack driving force and crack path for inclusion problems using XFEM and configurational forces, article in preparation.

International Conference Presentations and Proceedings:

1. Sathiskumar A. Ponnusami, A.S. Farle, W.G. Sloof, S. van der Zwaag , S. Turteltaub, "A cohesive zone fracture mechanics-based crack healing model and its application to self-healing MAX-phase ceramics", 6th International Conference on Self-Healing Materials ICSHM2017, Friedrichshafen, Germany, June 2017.

2. Sathiskumar A Ponnusami, Jayaprakash Krishnamsay, Sergio Turteltaub, Ann-Sophie Farle, Willem G. Sloof, Sybrand van der Zwaag, "Crack healing model for extrinsic and intrinsic self-healing materials, European Mechanics of Materials Conference (EMMC15), 2016, Brussels, Belgium.

3. Sathiskumar A. Ponnusami, W.G. Sloof, S. van der Zwaag , S. Turteltaub, "A parametric study of crack-healing particle interaction as a function of mechanical properties of the constituent phases", Fifth International Conference on Self-Healing Materials ICSHM2015, Durham, North Carolina, USA, 2015.

4. Sathiskumar A. Ponnusami, Sergio Turteltaub, "Crack-particle interactions in heterogeneous materials", 11th World Congress on Computational Mechanics, World Congress on Computational Mechanics, WCCM XI, Barcelona Spain, 2014.

5. Z. Derelioglu, Sathiskumar A. Ponnusami, S. Turteltaub, S. van der Zwaag and W.G. Sloof, "Healing Particles in Self-Healing Thermal Barrier Coatings", Fourth International Conference on Self-Healing Materials ICSHM2013, Ghent, Belgium, 2013.

6. D. Harursampath, M. Gupta, S. Agrawal, Sathiskumar A Ponnusami, D. Veerasamy, Sangheetha A P, "Blending modern multifunctional materials with traditional structures: An approach towards greener and cleaner aviation", 72nd Annual Forum of American Helicopter Society, Florida, USA, May 2016.

7. D. Harursampath, Sathiskumar A. Ponnusami, S. Agrawal, M. Gupta, and D. Veerasamy, "A Multifunctional Composite System for Rotorcraft structures-An Investigation of Energy harvesting and storage characteristics" American Helicopter Society (AHS) International's Sustainability 2015 - An International Conference on Environmental Sustainability in Air Vehicle Design and Operations of Helicopters and Airplanes, Montreal, Canada, 2015.

European/National Conference Presentations:

1. Sathiskumar A. Ponnusami, Sergio Turteltaub, Sybrand van der Zwaag “Self-healing Thermal barrier coatings- Modelling aspects”, 9th IOP Symposium on Self-healing materials, Gouda, The Netherlands, 2014
2. Sathiskumar A. Ponnusami, Sergio Turteltaub,“ Modelling Self-healing Thermal barrier coatings”, Sixteenth Engineering Mechanics Symposium, Lunteren, The Netherlands, 2013.
3. Sathiskumar A. Ponnusami, Sergio Turteltaub, “Crack-particle interactions in Self-healing Thermal barrier coatings”, Dutch-German Symposium on Self-healing materials, Gouda, The Netherlands, 2013.

Invited Talks and Presentations:

1. Sathiskumar A. Ponnusami, (Seminar), "Multifunctional Aerospace Structures - A Key Towards Sustainable Aviation?”, Department of Mechanical Engineering, National University of Singapore, March 2016.
2. Sathiskumar A. Ponnusami, (Invited Keynote Talk), "A Hybrid Multifunctional Fiber Composite for Next Generation Aircraft Structures”, 9th Aviation Knowledge and Career Day: Theme- ‘Out of the Box’, A Conference for Engineers, Pilots and Airlines, Hogeschool van Amsterdam, Netherlands, December 2015.
3. Sathiskumar A. Ponnusami, (Invited Lecture), "Sustainable Transportation through Nature-inspired Multifunctional composite materials”, Bèta talk, Delft University of Technology, Netherlands, December 2015.

Magazine articles:

1. Sathiskumar A. Ponnusami, “Self-healing Thermal Barrier Coatings”, Leonardo Times, Journal of the Society of Aerospace Engineering Students, ‘Leonardo da Vinci’, 17(1), 44-46, 2013.
2. “Aerocomposites: The move to multifunctionality”, Contributed article to CompositesWorld Magazine, Gardner Publications, USA, 2015.
3. Sathiskumar A. Ponnusami, Raphael Klien, "Airbus Fly Your Ideas 2015: Team MultiFun wins”, Leonardo Times, Journal of the Society of Aerospace Engineering Students, ‘Leonardo da Vinci’, 12-16, October 2015.

Patent:

1. Dineshkumar Harursampath, Sathiskumar A Ponnusami, S. Harlanayaka, Shashank Agrawal, Mohit Gupta, D. Veerasamy, "A multifunctional system and a method for integrated energy recycling and storing", Patent no: 287775, Application no: 201641032216, Date granted: 26/09/2017 (Indian patent).

ACCOMPLISHMENTS

1. Winning Team (among 518 teams from 104 countries with 3700 students) in Airbus- UNESCO Fly Your Ideas Global Innovation competition 2015, Team MultiFun. (Role: Team Leader). Along with coveted trophy, a cash prize of 30,000 euros was awarded at Airbus German Headquarters, Hamburg, Germany, May 2015.

2. Winner - Dutch Aerospace Award 2015 awarded by NLF (Netherlands Aerospace Funds). The award aimed at 'Encouraging to Excel' in the field of Aerospace with a focus on innovation. Along with medal, a cash prize of 5000 euros was awarded.

3. Young Scientist Award at 4th International Conference on Self-healing Materials, Ghent, Belgium with a research grant of 5000 euros.

4. Winner- ITMA Future Materials Awards 2015 for best innovative idea and finalist in the categories of best innovation in mobile textiles (aerospace and automotive composites) and sustainable textiles. Awarded by the Future materials magazine and World Textile Information network (WTIN), UK recognizing success in textile composites innovation at ITMA Conference, Milan, Italy, November 2015.

5. Finalist- University World Cup 2015 for best concepts and start-up idea, Multi-Fun. Selected as one of the 38 finalist teams from over 750 university teams for University World Cup organized by Venture Cup, Copenhagen, Denmark.

6. Outstanding Performance Award in the category of Aero Structures at Mahindra's Young Engineer Awards 2010, Bangalore, India. Selected as the best entry in the category of aerospace structures for the project on 'Micromechanical studies/analyses on fiber reinforced composite interfaces for high temperature aerospace applications'.

7. Nominated for Indian National Academy of Engineering's (INAE) 'Innovative Potential Award' for the Master's Project by the Aerospace Engineering Department, Indian Institute of Science, 2011.

LIST OF FIGURES

List of Tables

ISBN 9789462999442